

A complete waveform comparison of post-Newtonian and numerical relativity in eccentric orbits

Hao Wang,^{1,*} Yuan-Chuan Zou,^{1,†} Qing-Wen Wu,^{1,‡} Xiaolin Liu,^{2,§} and Zhao Li^{3,4,5,¶}

¹*Department of Astronomy, School of Physics, Huazhong University of Science and Technology, Wuhan 430074, China*

²*Instituto de Física Teórica UAM-CSIC, Universidad Autónoma de Madrid, Cantoblanco 28049 Madrid, Spain*

³*Department of Astronomy, University of Science and Technology of China, Hefei, Anhui 230026, China*

⁴*School of Astronomy and Space Science, University of Science and Technology of China, Hefei 230026, China*

⁵*Department of Physics, Kyoto University, Kyoto 606-8502, Japan*

(Dated: September 27, 2024)

This study presents a thorough comparative analysis between post-Newtonian (PN) and numerically relativistic (NR) waveforms in eccentric orbits, covering nonspinning and spin-aligned configurations. The comparison examines frequency, amplitude, and phase characteristics of various harmonic modes, such as 22, 21, 33, 32, 44, 43, and 55 modes. The study utilizes eccentric PN waveforms based on 3PN quasi-Keplerian parameterization with 3PN radiative reaction, surpassing Newtonian quadrupole moment with higher-order moments. NR waveforms from RIT and SXS catalogs span mass ratios from 1/4 to 1, eccentricities up to 0.45, and durations exceeding 17000M across nonspinning and spin-aligned configurations. Focusing on the 22 mode, frequency comparisons between quadrupole and higher-order moments of Ψ_4^{22} and h^{22} were conducted. Amplitude comparisons revealed superior accuracy in quadrupole moments of Ψ_4^{22} . Analysis of total 180 sets of eccentric waveforms showed increasing fitting residuals with rising eccentricity, correlating with smaller mass ratios. Comparisons of initial eccentricity from PN fitting, 3PN quasi-Keplerian parameterization, and RIT/SXS catalogs revealed alignment discrepancies. Frequency, phase, and amplitude comparisons of 22 modes showed consistent inspiral behavior between PN and NR, with divergences near merger for nonspinning PN and pre-200M for spin-aligned PN. Average errors of frequency, phase, and amplitude up to 200M pre-merger amplified with increasing eccentricity. Average errors for eccentricities 0-0.2 were below 3% for frequency, 0.2 for phase, and 6% for amplitude. For eccentricities 0.2-0.4, errors increased. The higher-order modes demonstrated consistent trends for frequency and phase, and with increased amplitude errors, underscoring the self-consistency of the PN fitting process. Fittings on three RIT eccentric waveforms with low mass ratios highlighted challenges in NR simulations for such scenarios. Refinements in PN accuracy, especially at higher orders, and improvements in NR simulations for small mass ratios are essential for precise gravitational wave templates in eccentric orbits, reducing systematic errors in parameter estimation and advancing gravitational wave detection.

I. INTRODUCTION

Gravitational wave astronomy has heralded a new epoch following the inaugural binary black hole (BBH) merger event GW150914 in 2015 [1]. To date, the terrestrial gravitational wave observatories LIGO [2], Virgo [3], and KAGRA [4] (LVK) have collectively detected 90 merger events involving binary compact objects during the O1, O2, and O3 observation runs [5]. These events encompass binary black hole mergers, binary neutron star mergers, and black hole-neutron star mergers.

Currently, diverse methodologies are employed to study BBH dynamics, including post-Newtonian (PN) approaches [6], effective one body (EOB) models [7, 8], black hole perturbation theory (BHPT) [9], and numerical relativity (NR) simulations [10–12], among others. While the former methods are approximations, NR is

recognized for its comprehensive and precise numerical treatment. This study focuses on comparing PN and NR methodologies. In the PN domain, a tailored approach for low-speed and weak-field scenarios ($v^2/c^2 \sim GM/c^2r \ll 1$) characterizes BBH dynamics. It refines Newtonian motion by incorporating high-order corrections through multipole expansions into dynamic quantities. In contrast, NR addresses BBH dynamics as an initial value problem, necessitating the specification of initial conditions and evolution equations [13]. NR provides a comprehensive solution that includes strong field effects. However, its computational requirements are substantial, often demanding several months on a supercomputer for a single set of simulation. To establish the consistency between PN and NR results, numerous studies have scrutinized PN and NR waveforms, primarily focusing on circular orbits in nonspinning [14–18], spin-aligned [19, 20], and spin-precession [21] configurations. Notably, research on eccentric orbits is limited, with only a few references comparing the 22 mode and higher-order modes of nonspinning waveforms [22–24].

The predominant emphasis in current research on NR and PN methods on circular orbits can be ascribed to the impact of gravitational wave radiation, which dissipates

* husthaowang@hust.edu.cn

† zouyc@hust.edu.cn

‡ qwwu@hust.edu.cn

§ shallyn.liu@foxmail.com

¶ lz111301@mail.ustc.edu.cn

energy and momentum [25, 26]. This mechanism results in the circularization of isolated BBHs in the galactic vicinity prior to their merger, even if they possess significant initial eccentricities [27]. Consequently, as the binary system transitions into the gravitational wave detection frequency band around 10 Hz, the eccentricity is expected to be negligible. However, there are some mechanisms through which BBHs can acquire eccentricity before merging [28]. In dense stellar environments like globular clusters [29–36] and galactic nuclei [37–43], interactions such as double-single [44, 45], double-double interactions [46, 47], and gravitational capture [37, 48] can induce eccentricity in BBHs. Furthermore, in a three-body system [49], such as binary objects near a supermassive black hole, the eccentricity of the inner binary objects may oscillate due to the Kozai-Lidov mechanism [49–56], becoming observable upon entering the detection frequency band. Remarkably, some BBH mergers originating from globular clusters that enter the LIGO sensitive band maintain eccentricities surpassing 0.1 [34]. The event GW190521 [57] is considered a potential BBH merger with a high eccentricity of $e = 0.69$ [58, 59]. With the advancement of detector sensitivity, an increasing number of eccentric BBH mergers are anticipated to be identified in O4 by the LIGO-Virgo-KAGRA (LVK) collaboration or by upcoming ground-based gravitational-wave observatories like the Einstein Telescope (ET) [60] or Cosmic Explorer (CE) [61].

In recent decades, several prominent NR collaborations, including Simulating eXtreme Spacetimes (SXS) [62, 63], Rochester Institute of Technology (RIT) [64–67], bi-functional adaptive mesh (BAM) [68–70], and MAYA [71, 72], have conducted extensive simulations of binary compact objects, with their simulation datasets publicly accessible. In the domain of NR simulations concerning eccentric orbit BBH systems, recent collaborations have ventured into a wider parameter space. For example, SXS has released 20 sets of nonspinning eccentric orbit waveforms encompassing mass ratios from 1/3 to 1 and eccentricities from 0 to 0.2, covering the 22 mode and higher-order modes 21, 33, 32, 44, 43, and 55 [73]. Conversely, RIT has published 824 sets of nonspinning, spin-aligned, and spin-processed eccentric orbit waveforms with mass ratios ranging from 1/32 to 1 and eccentricities from 0 to 1, also including the 22 mode and higher-order modes 21, 33, 32, 44, and 43 [67, 74]. The extensive collection of NR simulations now accessible provides a rich dataset for thorough exploration and analysis of eccentric orbit BBH mergers.

Substantial progress has been achieved in the investigation of PN waveforms for BBH in eccentric orbits over recent decades. The computation of PN waveforms in eccentric orbit typically involves three crucial components: conservative dynamics, radiative dynamics, and the determination of the quadrupole moment or higher-order moment, also referred to as the amplitude of gravitational waves. In the realm of conservative dynamics, Memmesheimer et al. [75] examined the quasi-Kepler

parameterization of the nonspinning configuration up to 3PN under ADM and harmonic coordinates, while recent work by Cho et al. [76] extended this analysis to the 4PN order. Tessmer et al. [77] concentrated on the quasi-Kepler parameterization of spin-aligned BBHs at 2PN, with a further extension to the 3PN order in the study by Tessmer et al. [78]. Regarding radiative dynamics, Konigsdorffer and Gopakumar [79, 80] computed the 2PN instantaneous term and 1.5PN hereditary term for nonspinning systems, while Arun et al. [81–84] expanded this investigation to the 3PN order, encompassing instantaneous and hereditary contributions such as the tail and memory effects. In the context of the quadrupole moment, higher-order moments, or gravitational wave amplitude, Mishra et al., Boetzel et al., and Ebersold et al. [85–87] calculated the amplitude of the higher-order moment for nonspinning systems at 3PN, including higher-order modes up to the 10-10 mode, analyzing both the instantaneous and hereditary components. Klein et al. [88] investigated the spin effects of 2PN in the phasing of gravitational waves from binaries on eccentric orbits. Henry et al. [89] explored radiation dynamics and higher-order moments for spin-aligned waveforms at the 3PN level. These comprehensive computational investigations have improved the accuracy of PN gravitational waveforms for eccentric orbits and significantly broadened the parameter space available for detailed analysis.

The most recent PN and NR discoveries have paved the way for a more in-depth comparison between the two, laying the foundation for the development of more precise hybrid waveforms that blend PN and NR data. The creation of accurate hybrid waveforms combining PN and NR information for eccentric orbits has been a central focus in gravitational wave detection over the past decade. While studies by Chattaraj et al., Huerta et al., Hinder et al., and Huerta et al. [23, 90–92] have contributed significantly in this area, the parameter space remains notably restricted, particularly in scenarios involving low mass ratios, high eccentricities, and spin-aligned configurations. Therefore, the development of corresponding PN waveforms is crucial to address these limitations. In this research, we present a comprehensive and detailed comparison of PN and NR waveforms for eccentric orbits, encompassing both nonspinning and spin-aligned setups. Our analysis spans mass ratios from 1/4 to 1 and eccentricities from 0 to 0.45, including waveform harmonic modes 22, 33, 32, 44, 43, and 55, and incorporating the high-order moments of the waveform. Through this meticulous approach, our objective is to advance the generation of precise gravitational wave templates for eccentric orbit binary black holes, signifying progress towards more sophisticated waveform constructions.

This paper is structured as follows: In Section II A, we introduce the foundational principles and waveform construction for BBH systems using PN theory with nonspinning and spin-aligned configurations in eccentric orbits. Section II B delves into the eccentric waveforms obtained from the RIT and SXS catalogs employed in

this investigation. Section II C outlines the fitting process of PN and NR waveforms. Section II D provides a comparative analysis of different methods for measuring eccentricity. Moving to Section III A, we present the residuals resulting from our waveform fitting. Section III B explores the distinctions between various eccentricity measurement methodologies. In Section III C, we present the fitting outcomes and error assessments for the dominant mode (22), while Section III D extends these outcomes to higher-order modes (21, 33, 32, 44, 43, and 55). Section III E addresses challenges encountered in fitting waveforms from systems with small mass ratios within the RIT catalog. Finally, Section IV summarizes our discoveries and outlines prospects for future research. Throughout, natural units are utilized, i.e., $G = c = 1$, with explicit mention of G and c where necessary for clarity.

II. METHODS

A. Eccentric post-Newtonian waveforms

In this section, we begin by outlining fundamental concepts concerning a PN system operating in eccentric orbits. This description is notably succinct. For those seeking more comprehensive insights, we recommend consulting the seminal work on PN by Blanchet et al. [6]. For a nonspinning BBH setup, the constituent black holes possess masses denoted as m_1 and m_2 . The combined mass is represented by $M = m_1 + m_2 = 1$, serving as a pivotal mass scale in both the PN and NR domains. The mass ratio is articulated as $q = m_1/m_2$, with m_1 being smaller than m_2 . The reduced mass is calculated as $\mu = m_1 m_2 / M$, while the symmetric mass ratio is defined as $\eta = \mu / M$.

In Newtonian orbits, both energy and angular momentum are conserved, with the constancy of the latter implying that the orbit remains confined to a single plane without precession. As outlined in Ref. [24], we can describe the relative orbit radius r and angular frequency $\dot{\phi}$ (where ϕ denotes the relative angular coordinate) as follows:

$$r = a(1 - e \cos u), \quad (1)$$

$$\dot{\phi} = \frac{n\sqrt{1-e^2}}{(1-e\cos u)^2}, \quad (2)$$

where a and e represent the semimajor axis and eccentricity, respectively, constants within Newtonian orbits. The eccentric anomaly u and mean motion n are also introduced, specifically, $n = 2\pi/P = a^{-3/2}M^{1/2}$, where P signifies the orbital period from one pericenter to another. The eccentric anomaly u obeys Kepler's equation:

$$l = u - e \sin u, \quad (3)$$

where the mean anomaly l satisfies $\dot{l} = n$. Given that n remains constant within Newtonian orbits, integration leads to $l = n(t - t_0)$, with t_0 denoting the integration constant (representing the initial moment). Equation (3) serves as a transcendental algebraic equation for u , which necessitates numerical solutions at each time step. Subsequently, utilizing Eqs. (1) and (2), we can derive related coordinates r and $\dot{\phi}$ at any given time. By further differentiation and integration, \dot{r} and ϕ can be obtained. Through this process, Newtonian orbital dynamics are fully resolved, with each orbit characterized by constants n , e , $\phi_0 \equiv \phi(t_0)$, and $l_0 \equiv l(t_0)$.

In PN orbits, we can establish conservative dynamical equations akin to those in the Newtonian scenario, albeit with slight modifications. The Newtonian expressions for r , $\dot{\phi}$, and l are adjusted by the inclusion of higher-order PN terms. Furthermore, in contrast to the Keplerian parameterization observed in Newtonian dynamics, the quasi-Keplerian parameterization in PN introduces eccentricities e_t , e_r , and e_ϕ at distinct coordinates t , r , and ϕ . These eccentricities are interconnected and converge to the Newtonian eccentricity e at lower orders. Typically, in PN literature, e_t is selected as the primary measure of eccentricity. Notably, in PN scenarios, the orbital plane undergoes precession. Owing to this precession effect, the orbital plane rotates by an angle $\delta\phi$ within one orbital period P , allowing the definition of the orbital angular frequency as:

$$\omega \equiv \frac{2\pi + \delta\phi}{P}. \quad (4)$$

According to Refs. [24, 79], two models have been proposed for PN systems in eccentric orbits. The first model, referred to as the n model, employs n and e_t as parameters. The second model, known as the x model, utilizes the common expansion variable of PN, $(M\omega)^{2/3}$, along with e_t as parameters. As elucidated in Ref. [24], the latter model more accurately depicts the waveform of eccentric orbits in the PN framework. In our analysis, we will explore two scenarios of PN eccentric orbital BBH waveforms: one involving nonspinning black holes and the other featuring spin-aligned (non-precessing) black holes, where the directions of orbital angular momentum and spin angular momentum are either parallel or antiparallel. Despite their differences in spin configurations, the dynamics of these two cases exhibit remarkable similarities and can be approached through analogous procedures.

1. Nonspinning waveforms

Citing Refs. [24, 75], we investigate the conservative orbital dynamics of the 3PN order within modified harmonic coordinates, specifically employing the quasi-Keplerian parametrization. These expressions are dependent on the energy E and the angular momentum

J as outlined in Ref. [75]. Following the methodology presented in Ref. [24], we reframe these expressions in terms of the variables x and e_t . For brevity, we provide condensed versions here, while detailed expressions can be found in Appendix A. The PN form of Eq. (1) and Eq. (2) for nonspinning BBH can be expressed as

$$r^{\text{NS}} = r_{\text{Newt}}^{\text{NS}} x^{-1} + r_{1\text{PN}}^{\text{NS}} + r_{2\text{PN}}^{\text{NS}} x + r_{3\text{PN}}^{\text{NS}} x^2 + \mathcal{O}(x^3) \quad (5)$$

and

$$\dot{\phi}^{\text{NS}} = \dot{\phi}_{\text{Newt}}^{\text{NS}} x^{3/2} + \dot{\phi}_{1\text{PN}}^{\text{NS}} x^{5/2} + \dot{\phi}_{2\text{PN}}^{\text{NS}} x^{7/2} + \dot{\phi}_{3\text{PN}}^{\text{NS}} x^{9/2} + \mathcal{O}(x^{11/2}), \quad (6)$$

where the superscript NS indicates nonspinning, and $r_{1\text{PN}}^{\text{NS}}$, $\dot{\phi}_{1\text{PN}}^{\text{NS}}$, etc., denote the PN expansion coefficients, functions of e_t and u . Additionally, Eq. (3) and $\dot{l} = n$ transform into

$$\dot{l}^{\text{NS}} = u - e_t \sin u + l_{2\text{PN}}^{\text{NS}} x^2 + l_{3\text{PN}}^{\text{NS}} x^3 + \mathcal{O}(x^4) \quad (7)$$

and

$$j^{\text{NS}} = n^{\text{NS}} = x^{3/2} + n_{1\text{PN}}^{\text{NS}} x^{5/2} + n_{2\text{PN}}^{\text{NS}} x^{7/2} + n_{3\text{PN}}^{\text{NS}} x^{9/2} + \mathcal{O}(x^{11/2}), \quad (8)$$

where, unlike $r_{1\text{PN}}^{\text{NS}}$, $\dot{\phi}_{1\text{PN}}^{\text{NS}}$, etc., $l_{1\text{PN}}^{\text{NS}}$, $n_{1\text{PN}}^{\text{NS}}$, etc., are solely functions of e_t . For PN conservative dynamics, the integration of the right-hand side of Eq. (8), with respect to the constants x and e_t , allows for the direct determination of $l(t)$ in terms of the integration constant l_0 at the initial time t_0 . Subsequently, by substituting the obtained $l(t)$ into Eq. (7), we solve for u through numerical methods, then substitute u into Eqs. (5) and (6) to evaluate r^{NS} and $\dot{\phi}^{\text{NS}}$.

Previously, we focused solely on the conservative dynamics of BBH systems. However, in realistic BBH scenarios, gravitational radiation leads to the loss of energy and angular momentum, causing the parameters x and e_t to evolve over time. In the context of PN calculations, this evolution is typically treated using an adiabatic approximation, averaging over one orbital period to compute \dot{x} and \dot{e}_t . These quantities can be decomposed into instantaneous and nonlinear hereditary terms. The instantaneous terms depend on the retarded time, while the hereditary terms are time integrals, accounting for the system's entire dynamical history. As discussed in Refs. [81–83], the hereditary contributions include not only tail, tail-of-tail, and tail-square terms (similar to the energy flux) but also a memory contribution at 2.5PN order. Our 3PN radiative dynamics calculations are based on Ref. [81] and are expressed as follows:

$$\dot{x}^{\text{NS}} = \dot{x}_{\text{inst}}^{\text{NS}} + \dot{x}_{\text{hered}}^{\text{NS}} \quad (9)$$

and

$$\dot{e}_t^{\text{NS}} = \dot{e}_{t\text{inst}}^{\text{NS}} + \dot{e}_{t\text{hered}}^{\text{NS}}, \quad (10)$$

where the subscripts *inst* and *hered* mean *instantaneous* and *hereditary*. Their specific expressions are

$$\dot{x}_{\text{inst}}^{\text{NS}} = \frac{2c^3\eta}{3GM} x^5 (\dot{x}_{\text{Newt}}^{\text{NS}} + \dot{x}_{1\text{PN}}^{\text{NS}} x + \dot{x}_{2\text{PN}}^{\text{NS}} x^2 + \dot{x}_{3\text{PN}}^{\text{NS}} x^3), \quad (11)$$

$$\dot{e}_{t\text{inst}}^{\text{NS}} = -\frac{c^3\eta}{GM} e_t x^4 (\dot{e}_{t\text{Newt}}^{\text{NS}} + \dot{e}_{t1\text{PN}}^{\text{NS}} x + \dot{e}_{t2\text{PN}}^{\text{NS}} x^2 + \dot{e}_{t3\text{PN}}^{\text{NS}} x^3), \quad (12)$$

$$\dot{x}_{\text{hered}}^{\text{NS}} = \frac{64c^3\eta}{5GM} x^4 (\dot{x}_{1.5\text{PN}}^{\text{NS}} x^{3/2} + \dot{x}_{2.5\text{PN}}^{\text{NS}} x^{5/2} + \dot{x}_{3\text{PN}}^{\text{NS}} x^3), \quad (13)$$

$$\dot{e}_{t\text{hered}}^{\text{NS}} = \frac{32c^3\eta}{5GM} e_t x^4 (\dot{e}_{t1.5\text{PN}}^{\text{NS}} x^{3/2} + \dot{e}_{t2.5\text{PN}}^{\text{NS}} x^{5/2} + \dot{e}_{t3\text{PN}}^{\text{NS}} x^3). \quad (14)$$

Ref. [24] addresses the correction for radiative reaction at 2PN order, with the hereditary term included only at 1.5PN order, which introduces certain limitations. To obtain a more accurate PN waveform, we adopt the 3PN results from Ref. [81] for the specific expressions in Eqs. (11), (12), (13), and (14), while confirming consistency with their 2PN counterparts. However, the results in Ref. [81] are provided in ADM (Arnowitt-Deser-Misner) coordinates, requiring the transformation of the time eccentricity e_t to harmonic coordinates. The parameter x , being coordinate-invariant, does not require transformation and can be used directly. For brevity, the detailed derivations of \dot{x}^{NS} and \dot{e}_t^{NS} are relegated to Appendix A. The adiabatic evolution equations governing \dot{x}^{NS} and \dot{e}_t^{NS} form an autonomous system, solvable independently of Kepler's equation. By providing initial conditions x_0 and e_{t0} , we can numerically solve the system of ordinary differential equations to obtain $\dot{x}^{\text{NS}}(t)$ and $\dot{e}_t^{\text{NS}}(t)$. From this point, the steps of the conservative dynamics, as outlined previously, are followed: integrating Eq. (8), solving the root of Eq. (7), and substituting the resulting u into Eqs. (5) and (6). Finally, by differentiating and integrating r^{NS} and $\dot{\phi}^{\text{NS}}$, we obtain \dot{r}^{NS} and $\dot{\phi}^{\text{NS}}$. At this stage, we have fully resolved the dynamics of BBHs in eccentric orbits with gravitational radiation reaction.

In most studies, the quadrupole moment, which represents the leading-order Newtonian contribution, forms the basis for constructing PN waveforms. This method, known as the restricted waveform approximation, is a crucial component in the development of waveforms. The gravitational wave strain h due to the quadrupole moment can be expressed as follows [24]:

$$h = h_+ - ih_\times, \quad (15)$$

$$h_+ = -\frac{M\eta}{R} \left\{ (\cos^2 \theta + 1) \left[\cos 2\phi' \left(-\dot{r}^2 + r^2 \dot{\phi}^2 + \frac{M}{r} \right) + 2r\dot{r}\dot{\phi} \sin 2\phi' \right] + \left(-\dot{r}^2 - r^2 \dot{\phi}^2 + \frac{M}{r} \right) \sin^2 \theta \right\}, \quad (16)$$

$$h_\times = -\frac{2M\eta}{R} \cos \theta \left\{ \left(-\dot{r}^2 + r^2 \dot{\phi}^2 + \frac{M}{r} \right) \sin 2\phi' - 2r \cos 2\phi' \dot{r}\dot{\phi} \right\}, \quad (17)$$

where $\phi' \equiv \phi - \varphi$, and θ and φ are the spherical polar angles. The gravitational wave strain h can be expressed as the leading 2-2 mode h^{22} , using the spin-weighted spherical harmonics ${}_2Y_2^2(\theta, \varphi) = \frac{1}{2}e^{2i\varphi} \sqrt{5/\pi} \cos^4(\theta/2)$ for $l = 2, m = 2$,

$$h^{22} = \int_{-2}^2 Y_2^{2*}(\theta, \varphi) h(\theta, \varphi) d\Omega, \quad (18)$$

$$= -\frac{4M\eta e^{-2i\phi}}{R} \sqrt{\frac{\pi}{5}} \left(\frac{M}{r} + (\dot{\phi}r + i\dot{r})^2 \right),$$

where $Y_2^{2*}(\theta, \varphi)$ represents the complex conjugate of ${}_2Y_2^2(\theta, \varphi)$. This gives us the dominant gravitational wave mode h_{22} . However, due to symmetry, the quadrupole moment alone is insufficient to derive higher modes such as h_{32} , h_{43} , and others. To capture the full complexity of the waveform, we must go beyond the quadrupole moment in Eq. (18) and incorporate higher-order moments.

Refs. [85–87] have thoroughly investigated the amplitudes of eccentric orbits, deriving both the instantaneous and hereditary terms of the waveform as functions of e_t and x . However, the waveforms in these references are expressed as low-eccentricity expansions of e_t , valid only for eccentricities less than 0.1, and are not applicable to the high-eccentricity regime considered in this work. Consequently, we rely solely on the instantaneous waveforms for general orbits provided in Ref. [85]. The derivation of the 3PN waveforms for general orbits utilizes the MPM-PN (multipolar post-Minkowskian and post-Newtonian) formalism. The gravitational waveform is then expressed using spin-weighted spherical harmonics as shown in Eq. (18). For brevity, the detailed expressions for the various waveform modes are relegated to Appendix A. Ref. [85] represents the nonspinning instantaneous waveform as:

$$h^{\ell m, \text{NS}} = \frac{4GM\eta}{c^4 R} \sqrt{\frac{\pi}{5}} e^{-im\phi} H^{\ell m, \text{NS}}. \quad (19)$$

Each mode originates from a different PN order, and thus, they cannot be expressed simultaneously. As an illustration, we consider the h^{22} mode, which can be written as

$$h^{22, \text{NS}} = \frac{4GM\eta}{c^2 R} \sqrt{\frac{\pi}{5}} e^{-2i\phi} H^{22, \text{NS}}, \quad (20)$$

where the amplitude $H^{22, \text{NS}}$ is expressed as a sum of terms from different PN orders:

$$H^{22, \text{NS}} = H_{\text{Newt}}^{22, \text{NS}} + H_{\text{1PN}}^{22, \text{NS}} + H_{\text{2PN}}^{22, \text{NS}} + H_{\text{2.5PN}}^{22, \text{NS}} + H_{\text{3PN}}^{22, \text{NS}}. \quad (21)$$

Focusing on the leading Newtonian order, we have:

$$H_{\text{Newt}}^{22, \text{NS}} = \frac{GM}{r} + r^2 \dot{\phi}^2 + 2ir\dot{r}\dot{\phi} - \dot{r}^2, \quad (22)$$

which reduces to the quadrupole moment expression in Eq. (18). Thus, we obtain the harmonic waveform modes for non-spinning BBH in eccentric orbits. Despite the exclusion of hereditary term contributions, the resulting accuracy remains adequate within a certain range.

2. Spin-aligned waveforms

For a spin-aligned or non-precessing BBH system in eccentric orbits, Ref. [89] provides a comprehensive analysis and formulation of gravitational wave modes and fluxes up to 3PN order. In this work, spin effects are incorporated into the quasi-Keplerian parameterization up to 3PN in harmonic coordinates, using the covariant Tulczyjew-Dixon SSC (Newton-Wigner spin-supplementary condition) [93]. Key results from Ref. [89] include next-to-leading order instantaneous spin-orbit and spin-spin contributions to the waveform modes, as well as the inclusion of hereditary (tail and memory) contributions to both modes and fluxes in eccentric orbits. Here, we introduce several new concepts: the antisymmetric mass ratio $\delta = (m_1 - m_2)/M$, and the dimensionless spin magnitudes $\chi_1 \equiv |\mathcal{S}_1| / (m_1^2)$ and $\chi_2 \equiv |\mathcal{S}_2| / (m_2^2)$. Both χ_1 and χ_2 are aligned with the z -axis of the coordinate system, and their values range from $[-1, 1]$; negative values indicate that the spin angular momentum is antiparallel to the orbital angular momentum, while positive values indicate alignment. Here, $|\mathcal{S}_1|$ and $|\mathcal{S}_2|$ represent the spin magnitudes. Following the approach of the non-spinning case, we first introduce the 3PN quasi-Keplerian parameterization for the spin-aligned case [77, 89]. Since we remain within the same harmonic coordinate system, the radial coordinate r^{SP} can be expressed as:

$$r^{\text{SP}} = r^{\text{NS}} + r^{\text{SO}} + r^{\text{SS}}, \quad (23)$$

where r^{NS} denotes the non-spinning component of r , as given by Eq. (5). The superscript SP indicates the *spin* contribution, SO denotes spin-orbit coupling, which represents the first-order term in spin, and SS refers to spin-spin coupling, which is the quadratic term in spin. The detailed expressions for r^{SO} and r^{SS} are (provided in Appendix A):

$$r^{\text{SO}} = r_{\text{1.5PN}}^{\text{SO}} + r_{\text{2.5PN}}^{\text{SO}}, \quad (24)$$

and

$$r^{\text{SS}} = r_{\text{2PN}}^{\text{SS}} + r_{\text{3PN}}^{\text{SS}}. \quad (25)$$

Similarly, for the orbital angular velocity $\dot{\phi}^{\text{SP}}$, we have

$$\dot{\phi}^{\text{SP}} = \dot{\phi}^{\text{NS}} + \dot{\phi}^{\text{SO}} + \dot{\phi}^{\text{SS}}, \quad (26)$$

where the abbreviations for $\dot{\phi}^{\text{SO}}$ and $\dot{\phi}^{\text{SS}}$ are

$$\dot{\phi}^{\text{SO}} = \dot{\phi}_{1.5\text{PN}}^{\text{SO}} + \dot{\phi}_{2.5\text{PN}}^{\text{SO}}, \quad (27)$$

and

$$\dot{\phi}^{\text{SS}} = \dot{\phi}_{2\text{PN}}^{\text{SS}} + \dot{\phi}_{3\text{PN}}^{\text{SS}}. \quad (28)$$

The Kepler's equation for the spin-aligned BBH is

$$l^{\text{SP}} = l^{\text{NS}} + l^{\text{SO}} + l^{\text{SS}}, \quad (29)$$

where the abbreviations for l^{SO} and l^{SS} are

$$l^{\text{SO}} = l_{2.5\text{PN}}^{\text{SO}}, \quad (30)$$

and

$$l^{\text{SS}} = l_{3\text{PN}}^{\text{SS}}. \quad (31)$$

Similarly, for the mean motion n , it can be expressed as

$$n^{\text{SP}} = n^{\text{NS}} + n^{\text{SO}} + n^{\text{SS}}, \quad (32)$$

where the abbreviations for n^{SO} and n^{SS} are

$$n^{\text{SO}} = n_{1.5\text{PN}}^{\text{SO}} + n_{2.5\text{PN}}^{\text{SO}}, \quad (33)$$

and

$$n^{\text{SS}} = n_{2\text{PN}}^{\text{SS}} + n_{3\text{PN}}^{\text{SS}}. \quad (34)$$

The above content provides the quasi-Keplerian parameterization at 3PN order for the dynamics of spin-aligned eccentric orbits in a BBH system. For further details, refer to Refs. [77, 89]. Next, we consider the evolution of x and e_t due to the energy and angular momentum carried away by gravitational radiation. Analogous to the non-spinning case, \dot{x}^{SP} and \dot{e}_t^{SP} can be expressed as

$$\dot{x}^{\text{SP}} = \dot{x}^{\text{NS}} + \dot{x}^{\text{SO}} + \dot{x}^{\text{SS}}, \quad (35)$$

and

$$\dot{e}_t^{\text{SP}} = \dot{e}_t^{\text{NS}} + \dot{e}_t^{\text{SO}} + \dot{e}_t^{\text{SS}}. \quad (36)$$

As in the nonspinning case, the spin-aligned scenario also includes contributions from both the instantaneous and hereditary terms. The abbreviations for \dot{x}^{SO} , \dot{x}^{SS} , \dot{e}_t^{SO} , and \dot{e}_t^{SS} are

$$\dot{x}^{\text{SO}} = \dot{x}_{\text{inst}}^{\text{SO}} + \dot{x}_{\text{hered}}^{\text{SO}}, \quad (37)$$

$$\dot{x}^{\text{SS}} = \dot{x}_{\text{inst}}^{\text{SS}}, \quad (38)$$

$$\dot{e}_t^{\text{SO}} = \dot{e}_{t\text{inst}}^{\text{SO}} + \dot{e}_{t\text{hered}}^{\text{SO}}, \quad (39)$$

$$\dot{e}_t^{\text{SS}} = \dot{e}_{t\text{inst}}^{\text{SS}}. \quad (40)$$

It is worth mentioning that the hereditary term of spin-spin coupling comes from beyond the 3PN order, so it is absent here. The specific expressions of the PN order of the above equations are

$$\dot{x}_{\text{inst}}^{\text{SO}} = \dot{x}_{1.5\text{PN}}^{\text{SO}} + \dot{x}_{2.5\text{PN}}^{\text{SO}}, \quad (41)$$

$$\dot{x}_{\text{hered}}^{\text{SO}} = \dot{x}_{3\text{PN}}^{\text{SO}}, \quad (42)$$

$$\dot{x}_{\text{inst}}^{\text{SS}} = \dot{x}_{2\text{PN}}^{\text{SS}} + \dot{x}_{3\text{PN}}^{\text{SS}}, \quad (43)$$

$$\dot{e}_{t\text{inst}}^{\text{SO}} = \dot{e}_{t1.5\text{PN}}^{\text{SO}} + \dot{e}_{t2.5\text{PN}}^{\text{SO}}, \quad (44)$$

$$\dot{e}_{t\text{hered}}^{\text{SO}} = \dot{e}_{t3\text{PN}}^{\text{SO}}, \quad (45)$$

$$\dot{e}_{t\text{inst}}^{\text{SS}} = \dot{e}_{t2\text{PN}}^{\text{SS}} + \dot{e}_{t3\text{PN}}^{\text{SS}}. \quad (46)$$

Similar to the nonspinning case, we substitute the radiation equation into the conservation equation to obtain r^{SO} and $\dot{\phi}^{\text{SP}}$, and we obtain the BBH evolution dynamics of the spin-aligned eccentric orbit. For the spin-aligned case, as in the previous nonspinning case, we only use the instantaneous terms expression of the general orbit, because the expression with hereditary terms in Ref. [89] is only expansions for low eccentricity and is not applicable to the cases of medium and high eccentricity, and is therefore not applicable to the content of our study. Each higher mode of spin-aligned waveform can be expressed as

$$h^{\ell m, \text{SP}} = \frac{4GM\eta}{c^4 R} \sqrt{\frac{\pi}{5}} e^{-im\phi} H^{\ell m, \text{SP}}. \quad (47)$$

We take the 22 mode as an example to give its specific PN order expression:

$$h^{22, \text{SP}} = \frac{4GM\eta}{c^4 R} \sqrt{\frac{\pi}{5}} e^{-2i\phi} H^{22, \text{SP}}, \quad (48)$$

where the amplitude $H^{22, \text{SP}}$ can be expressed as

$$H^{22, \text{SP}} = H^{22, \text{NS}} + H^{22, \text{SO}} + H^{22, \text{SS}}, \quad (49)$$

where $H^{22, \text{NS}}$ is the nonspinning portion of the aforementioned waveform. And the abbreviations of $H^{22, \text{SO}}$ and $H^{22, \text{SS}}$ are

$$H^{22, \text{SO}} = H_{1.5\text{PN}}^{22, \text{SO}} + H_{2.5\text{PN}}^{22, \text{SO}} + H_{3\text{PN}}^{22, \text{SO}}, \quad (50)$$

and

$$H^{22, \text{SS}} = H_{2\text{PN}}^{22, \text{SS}} + H_{3\text{PN}}^{22, \text{SS}}. \quad (51)$$

So far, we can obtain any desired spin-aligned PN waveform in an eccentric orbit. All the abbreviations mentioned above can be found in Appendix A for detailed.

B. Eccentric Numerical Simulations

Several NR collaborations have conducted extensive simulations of BBH mergers in quasicircular orbits. However, publicly accessible simulations involving eccentric orbits remain relatively scarce. The NR simulations of eccentric orbits used in this study were sourced from the RIT (Rochester Institute of Technology) [74] and SXS (Simulating eXtreme Spacetimes) [73] catalogs. The simulations in the RIT catalog were performed using the LazEv code [94], which employs the moving puncture approach [11] and the BSSNOK (Baumgarte-Shapiro-Shibata-Nakamura-Oohara-Kojima) formalism for the evolution system [13, 95, 96]. The LazEv code operates within the Cactus [97]/Carpet [98]/Einstein Toolkit [99] framework. The fourth release of the RIT catalog included 824 eccentric BBH NR simulations, covering a range of configurations including nonspinning, spin-aligned, and spin-precessing systems—with eccentricities ranging from 0 to 1 [67]. The eccentric waveforms utilized in this work are primarily sourced from the non-spinning and spin-aligned waveforms in the RIT catalog. The second source is the SXS Collaboration, which employs a multi-domain spectral method [100–103] in conjunction with a first-order version of the generalized harmonic formulation [104–107] of Einstein’s equations with constraint damping to evolve the initial data. The Spectral Einstein Code (SpEC) [73] is used for these NR simulations.

In NR, gravitational wave waveforms are extracted by computing the Newman-Penrose scalar or Weyl scalar Ψ_4 at a finite radius and then extrapolating it to null infinity. The scalar Ψ_4 can be expanded using spin-weighted spherical harmonic functions, similar to Eq. (18), as follows:

$$r\Psi_4 = \sum_{\ell,m} r\Psi_4^{\ell m} {}_{-2}Y_{\ell,m}(\theta, \phi), \quad (52)$$

where r is the extraction radius, and $\Psi_4^{\ell m}$ represents the expansion coefficient or harmonic mode. As r approaches infinity, the relationship between h and Ψ_4 is given by:

$$\Psi_4 = \frac{\partial^2}{\partial t^2} h. \quad (53)$$

The expansion coefficients $h^{\ell m}$ and $\Psi_4^{\ell m}$ follow the same relationship. Both $\Psi_4^{\ell m}$ and $h^{\ell m}$ data can be accessed from the RIT and SXS catalog databases. These data are available as harmonic modes, with up to 44 modes for RIT and 55 modes for SXS. The RIT and SXS catalogs also include detailed metadata for each simulated waveform, such as mass ratio, spin, initial orbital angular momentum, initial ADM energy, and the properties of the final remnants. This metadata provides comprehensive information for analysis.

To streamline the representation of the parameter space and aid in research, we introduce the concept of the effective spin in the z -direction, which aligns with

the orbital angular momentum L . This effective spin is defined as

$$\chi_{\text{eff}} = \frac{m_1\chi_1 + m_2\chi_2}{m_1 + m_2}. \quad (54)$$

During waveform processing, we initially excluded the first $300M$ and $100M$ of the SXS and RIT waveforms, respectively, to eliminate the effects of transient junk radiation. Following this, we identified the peak value of the gravitational wave amplitude, which was used as the reference for time alignment, setting this moment as the new time zero for the waveform. Table II in Appendix A provides a detailed set of parameters for the waveforms used in the comparison between PN and NR simulations. Additionally, the parameter ranges for the SXS and RIT waveforms are illustrated in FIG. 1. In FIG. 1, the initial eccentricity e_{t_0} is determined through PN fitting to 22 mode frequency of higher-order moments after removing transient junk radiation, a concept that will be further elaborated. RIT catalog provides a broad range of waveform parameters, the lowest mass ratio available for eccentric orbit waveforms is $1/32$. However, we have restricted our analysis to waveforms with mass ratios ranging from $1/4$ to 1 . The SXS catalog includes 20 nonspinning eccentric waveforms with mass ratios in the range $q \in [1, 3]$ and initial eccentricities $e_{t_0} \in [0, 0.2]$. In total, 180 waveforms were analyzed, including 160 nonspinning waveforms and 20 spin-aligned waveforms from the SXS and RIT catalogs. The rationale for this selection will be discussed in the following sections.

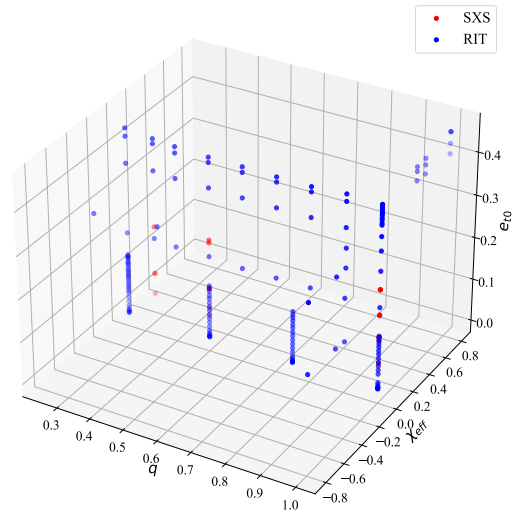


FIG. 1. The parameters used in our study include three configurations no spin, spin alignment, which cover the parameter space mass ratio q from $1/4$ to 1 , and the initial eccentricity e_{t_0} from 0 to 0.45 .

C. Fitting the post-Newtonian waveforms to numerical relativity waveforms

NR simulations are the most accurate method for modeling the dynamics of BBH systems. They precisely capture not only the inspiral phase but also the merger and ringdown phases, including complex strong-field dynamic effects. In contrast, the PN model provides high-order corrections to the speed of light to incrementally approximate the gravitational wave waveform. However, it is limited to cases where the black holes are widely separated, and their velocities remain well below the speed of light. Following the approach outlined in Ref. [24], we adopt a similar methodology: we use the NR waveform as the reference, fit the PN waveform to the NR data, and thereby extract a set of PN fitting parameters.

Before performing the fitting, we must first determine which quantities to compare, as we have two key elements: the gravitational wave strain h and the Newman-Penrose scalar Ψ_4 . Ref. [24] provides the correct framework for fitting Ψ_4 . However, many studies directly use h when constructing hybrid waveforms that combine PN and NR data. In this study of eccentric waveforms, we explore fitting both h and Ψ_4 to evaluate which one better aligns with the fitting expectations. For ease of comparison, we decompose both h and Ψ_4 into their amplitude and phase components as follows:

$$h^{\ell m} = \mathcal{A}^{\ell m}(t) \exp[-i\Phi^{\ell m}(t)], \quad (55)$$

$$\Psi_4^{\ell m} = A^{\ell m}(t) \exp[-i\varphi^{\ell m}(t)], \quad (56)$$

and the amplitude, phase and frequency of $h^{\ell m}$ can be obtained using the following equations:

$$\mathcal{A}^{\ell m} = |h^{\ell m}|, \quad (57)$$

$$\Phi^{\ell m} = \arg(h^{\ell m}), \quad (58)$$

$$\omega^{\ell m} = \frac{d\Phi^{\ell m}}{dt}. \quad (59)$$

The same is true for $\Psi_4^{\ell m}$, we can get the amplitude, phase and frequency of it by

$$A^{\ell m} = |\Psi_4^{\ell m}|, \quad (60)$$

$$\varphi^{\ell m} = \arg(\Psi_4^{\ell m}), \quad (61)$$

$$\varpi^{\ell m} = \frac{d\varphi^{\ell m}}{dt}. \quad (62)$$

Following the methodology outlined in Ref. [24], we use the gravitational wave frequency of the 22 mode as the parameter for PN fitting to NR waveforms, as it is

a coordinate-invariant quantity and represents the dominant mode. A time interval $I = [t_1, t_2]$ is selected, and least squares fitting is applied to obtain the optimal initial parameters for the PN fit to the NR waveform. As described in Sec. II A 1, determining the strain h^{22} requires first establishing the initial parameters e_{t0} and x_0 for e_t and x , followed by the integration constant l_0 and the initial phase parameter Φ_0^{22} . For Ψ_4^{22} , the same operation is performed after taking two time derivatives of h . In the context of NR data, the Ψ_4^{22} component can either be directly sourced from the catalog or computed by taking the second time derivative of h^{22} . Given the significant data noise in the Ψ_4^{22} dataset from the RIT catalog, this study adopts the latter approach, computing the second time derivative of h^{22} to ensure data accuracy and reliability. We take Ψ_4^{22} as an example to illustrate the fitting process. When performing frequency fitting only, the initial phase φ_0^{22} need not be considered. To conduct the least squares fit, we minimize the residual

$$Q(y_0) \equiv \frac{1}{N} \sum_{t \in I} [\varpi_{\text{PN}}^{22}(t; y_0) - \varpi_{\text{NR}}^{22}(t)]^2, \quad (63)$$

where subscripts PN and NR indicate that the waveforms come from PN and NR, respectively, N is the number of steps, and y_0 denotes the initial parameters:

$$y_0 \equiv [x_0, e_{t0}, l_0]. \quad (64)$$

For clarity, we omit the superscript 22 for frequency, amplitude, and phase, assuming their dominance in the 22 mode. Once the optimal initial parameters for the frequency are obtained, least squares fitting is applied to match φ_{PN} and φ_{NR} , determining the initial phase φ_0 . According to Ref. [24], if the fitting interval exceeds at least $200M$, the result will stabilize, becoming independent of the interval length. Otherwise, errors can occur. Hence, the fitting interval during the inspiral phase should be as long as possible to obtain the most accurate initial parameters y_0 .

When performing the fitting of PN to NR waveforms, we encounter four distinct scenarios: the choice between fitting the frequency of h^{22} or Ψ_4^{22} . Additionally, for both h^{22} and Ψ_4^{22} , we can either fit the frequency of their quadrupole moment (Eq. (18)) or consider the higher-order moments (Eq. (20)). In many studies [23, 90–92], the quadrupole moment of h^{22} is emphasized as the primary component for constructing waveforms. We use the waveform RIT:eBBH:1282 as a case study to demonstrate the outcomes across various fitting scenarios. Notably, there is a scarcity of previous studies comparing extended PN and NR waveforms for eccentric orbits, making this work relatively novel and indicative of broader trends. The characteristics of other waveforms closely align with this exemplar. In FIG. 2, we examine the frequency fitting of the 22 mode across four different cases: the quadrupole moment of h^{22} (panel (a) of FIG. 2), the higher-order moment of h^{22} (panel (b) of FIG. 2), the quadrupole moment of Ψ_4^{22} (panel (c) of FIG. 2), and

the higher-order moment of Ψ_4^{22} (panel (d) of FIG. 2). The waveform fitting interval extends from $100M$ after the waveform's onset to $1000M$ before the merger. As FIG. 2 illustrates, in all four cases, we observe a strong agreement between PN and NR waveforms during the inspiral phase, with discrepancies only becoming apparent near the merger. This highlights the exceptional accuracy of PN methods in capturing the inspiral phase of extended waveforms, an observation not fully addressed in prior literature. The fitting results for the four cases, including residuals Q (we use 1000 steps; the residuals show little dependence on the number of steps), l_0 , x_0 , and e_{t_0} , are presented in Table I. Based on these results, the magnitude of the residuals is on the order of 10^{-7} , indicating that all four cases provide a good fit to the NR waveform frequency. In fact, for shorter waveforms and lower eccentricities, the residual Q can be one to two orders of magnitude smaller. The similarity in residuals in Table I suggests that any of the four cases will yield accurate results. However, among the four cases, (d) consistently has the smallest residual, a trend that applies across all other waveforms after extensive fitting. It is important to note that there are non-physical fluctuations in the early part of the frequency of h^{22} (as seen in panels (a) and (b) of FIG. 2). These fluctuations necessitate global fitting for h^{22} , which means using as much of the waveform as possible, including the region close to the merger, rather than only part of the waveform. These non-physical fluctuations are not present in Ψ_4^{22} . For parameters such as l_0 , x_0 , and e_{t_0} , while we have stringent accuracy requirements for waveform fitting parameters (as will be explained later), the fitting results across the four cases do not maintain a consistent level of accuracy. As shown in Table I, l_0 can only be accurate to 0.1, x_0 to 0.001, and e_{t_0} to 0.01 across the four cases. We attribute this to numerical errors in the NR waveform and the differences between the higher-order and quadrupole moments in the PN expansion. There is no absolute right or wrong in these four scenarios, and any of them can be reasonably chosen as the fitting basis. For these reasons, we select the frequency of the 22 mode from the higher-order moment of Ψ_4^{22} as the fitting target.

TABLE I. Fitting results of the four cases in FIG. 2, including the residuals Q (we set the number of steps to 1000, the residual results have little dependence on the number of steps), l_0 , x_0 , e_{t_0} .

	Q	l_0	x_0	e_{t_0}
(a)	3.74×10^{-7}	4.27440580	0.04831607	0.19214287
(b)	2.40×10^{-7}	4.31218357	0.04826974	0.19500954
(c)	1.51×10^{-7}	4.26107246	0.04828178	0.19464287
(d)	1.17×10^{-7}	4.29085024	0.04824280	0.19711954

Following the discussion on frequency, it is crucial to address another key aspect of the waveform: the amplitude. Unlike frequency, amplitude is not necessarily gauge-invariant, which can cause it to behave differently.

In FIG. 3, we present the amplitude of the waveform RIT:eBBH:1282, corresponding to the four cases in FIG. 2: the quadrupole moment of h^{22} (panel (a)), the higher-order moment of h^{22} (panel (b)), the quadrupole moment of Ψ_4^{22} (panel (c)), and the higher-order moment of Ψ_4^{22} (panel (d)). In panel (a) of FIG. 3, we observe that the amplitude agrees well with the NR waveform's amplitude during a brief period prior to the merger, with increasing deviation as we move further from the merger. Panel (b) shows that the amplitude of the PN waveform deviates significantly from the NR amplitude throughout the entire time period. Panel (c) reveals the best agreement between the amplitude of PN and NR waveforms, with nearly no deviation in the inspiral phase and only deviations near the merger, consistent with the well-known limitations of PN approximations near the merger phase. In panel (d), the amplitude exhibits some consistency with the NR waveform during the inspiral, but visible deviations occur and grow larger as the merger approaches. From FIG. 3, we conclude that the amplitude of the quadrupole moment of Ψ_4^{22} shows the best agreement with the NR waveform, while the other cases exhibit varying degrees of deviation. These amplitude deviations are not unique to waveform RIT:eBBH:1282 but are present across all waveforms, particularly those that are relatively long (over $3000M$). This phenomenon occurs in both RIT and SXS waveforms. This observation supports the approach taken in many previous studies that rely solely on the quadrupole moment as a waveform approximation. While this method may work for short waveforms, it becomes less effective for longer waveforms.

Our goal here is not to investigate the underlying causes of these discrepancies but to focus on their phenomenological implications. As such, this paper will not delve into the amplitude of h^{22} due to its significant deviations. Instead, we concentrate on analyzing the amplitude of Ψ_4^{22} across different PN orders. In FIG. 4, we present waveform RIT:eBBH:1282, computed at various PN orders of Eq. (21), to illustrate the contributions of different PN approximations. For instance, selecting the 2PN order includes the preceding Newtonian, 1PN, and other relevant terms. The results in FIG. 4 reveal distinct contributions from various PN orders to the amplitude, particularly in the discrepancies that emerge near the merger. During the inspiral phase, the Newtonian order contributes most significantly to the amplitude, surpassing the contributions of higher-order PN terms. As noted earlier, the close agreement between the Newtonian order's amplitude and that of the NR waveform reinforces their consistency. In contrast, the amplitudes associated with higher PN orders exhibit varying degrees of deviation from the NR amplitude. These findings indicate that within the range of 3PN order, the Newtonian term provides the most accurate amplitude results. This observation also applies to higher harmonic modes, a point we will expand upon in later sections of this paper.

There is a vast array of RIT and SXS waveforms available for analysis. A total of 180 sets of waveforms

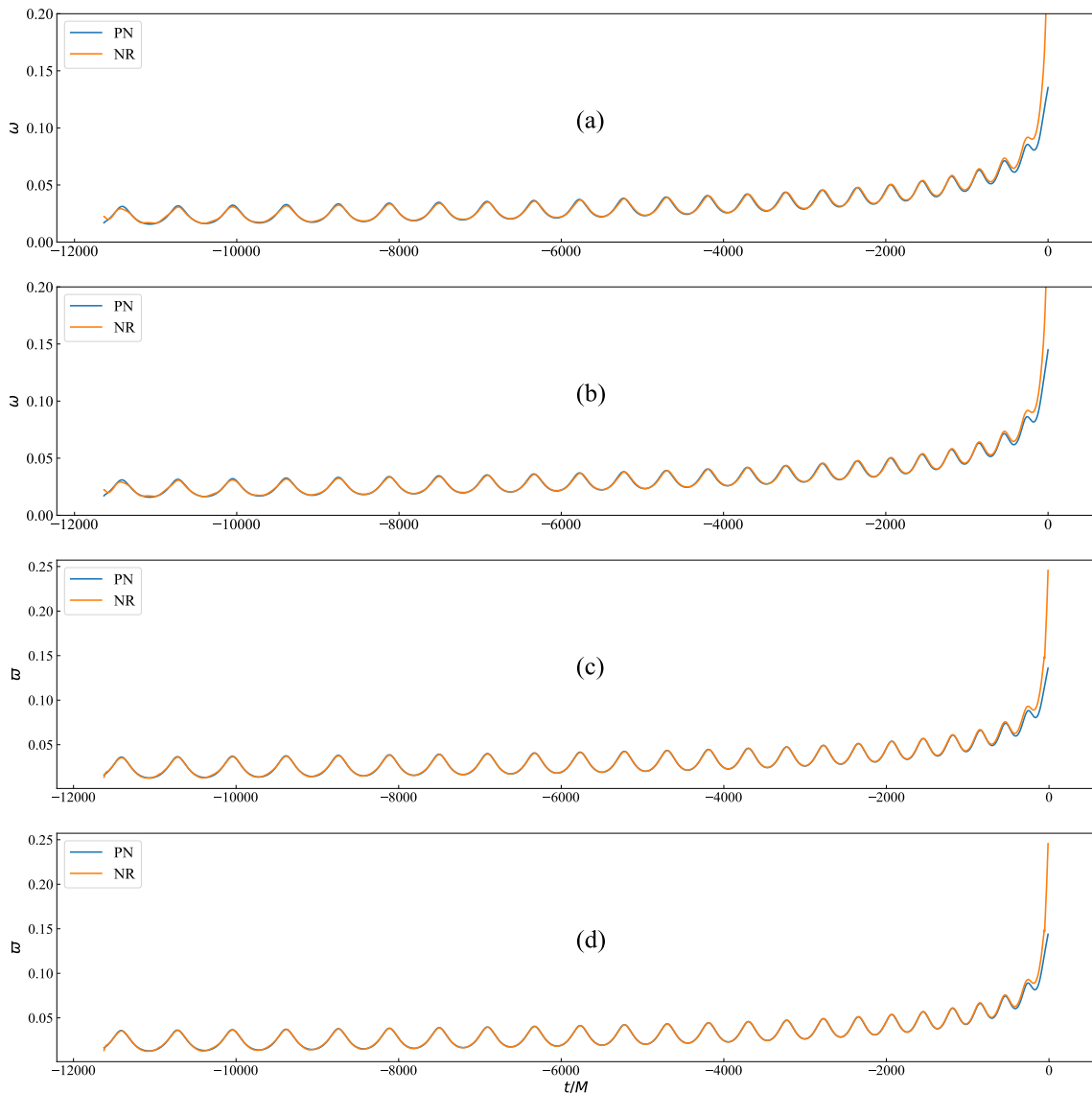


FIG. 2. Frequency fitting of the 22 mode across four distinct cases for waveform RIT:eBBH:1282: the quadrupole moment of h^{22} (panel (a)), the higher-order moment of h^{22} (panel (b)), the quadrupole moment of Ψ_4^{22} (panel (c)), and the higher-order moment of Ψ_4^{22} (panel (d)).

have been carefully selected for direct fitting, covering both nonspinning and spin-aligned configurations. Consequently, this study necessitates a substantial amount of waveform fitting. For each waveform, three free parameters $y_0 \equiv [x_0, e_{t0}, l_0]$ are essential for fitting, with each parameter requiring precise determination within specified accuracy bounds. e_{t0} must be determined with a precision of at least 0.001, x_0 must be resolved to a minimum of 0.0001, and l_0 must be ascertained with an accuracy threshold of at least 0.01 to ensure the required precision. This precision is directly linked to the sensitivity of parameters in the PN fitting process, with x_0 exhibiting the highest sensitivity, followed by e_{t0} , and l_0 at a lower sensitivity level. These observations have been derived from extensive fitting exercises conducted

in our research. The utilization of the standard parameter range of y_0 for NR waveform fitting often results in extensive computations and issues, frequently leading to infinite or invalid values under the square root. To optimize computational efficiency, we have developed some techniques to constrain parameter ranges effectively.

In light of the fitting process for waveform RIT:eBBH:1282, it is crucial to revisit FIG. 1 in Sec. II B to understand why only 180 sets of waveforms are retained for fitting, instead of encompassing all the eccentric waveforms from RIT. The waveforms chosen for fitting must possess sufficient length. While we previously indicated that a correctly fitted waveform should have a minimum duration of $200M$, practical fitting requires a waveform duration exceeding $350M$ in NR sim-

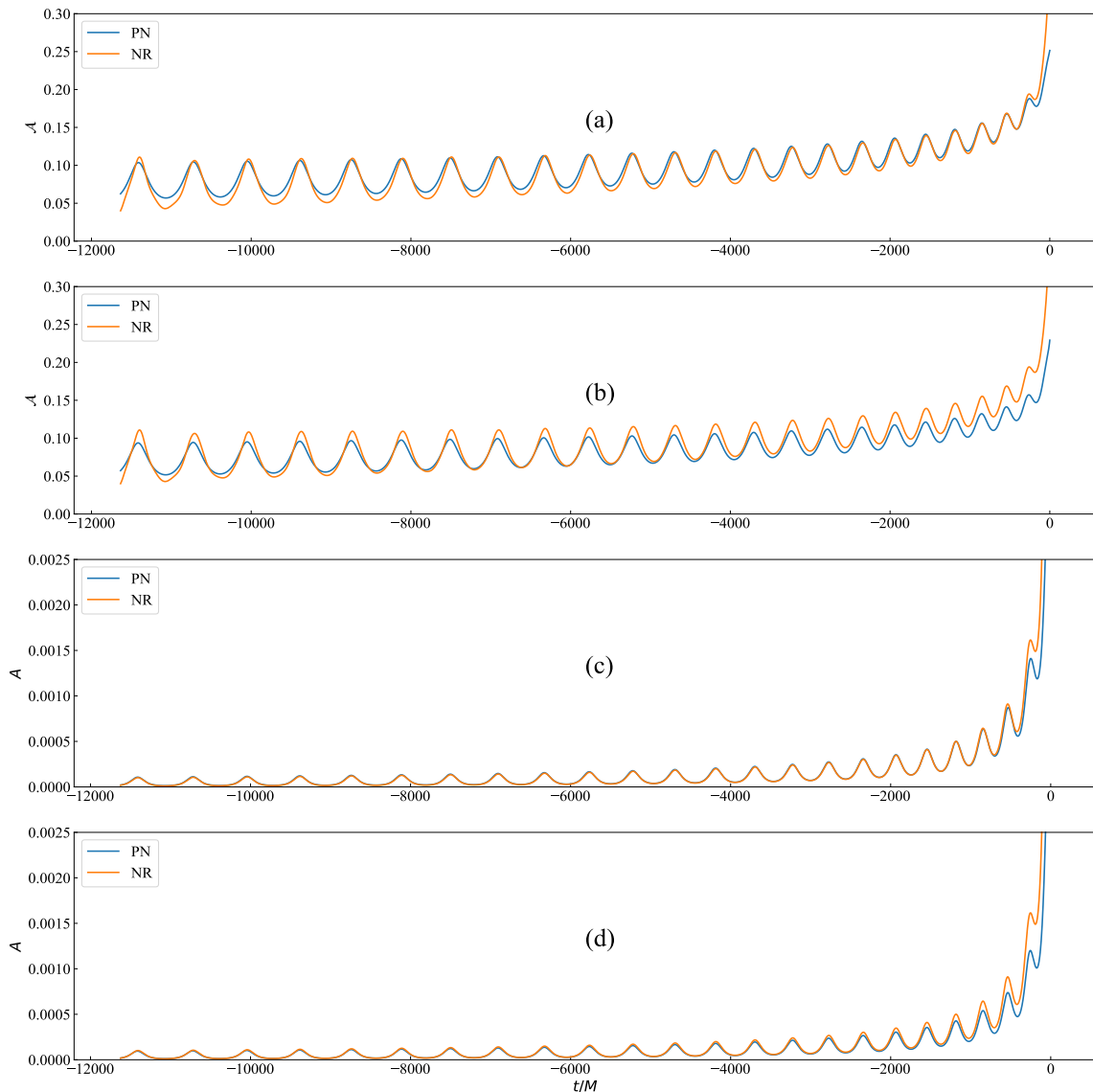


FIG. 3. The amplitude of the waveform RIT:eBBH:1282 in the four cases of FIG. 2: the quadrupole moment of h^{22} (panel (a)), the higher-order moment of h^{22} (panel (b)), the quadrupole moment of Ψ_4^{22} (panel (c)), and the higher-order moment of Ψ_4^{22} (panel (d)).

ulations to achieve an accurate match. Furthermore, the waveform frequency should exhibit at least two peaks, signifying two periastron passages. This criterion leads to the exclusion of numerous highly eccentric waveforms from RIT. Accommodating a highly eccentric waveform necessitates substantial initial separation and heightened initial eccentricity in NR simulations.

In the process of determining x_0 , directly setting a fitting interval can introduce challenges in precisely defining the range, potentially leading to issues such as encountering infinite values during fitting and obtaining imprecise estimates. To overcome these challenges and enhance precision in derivation, we propose approximating the evolution of $x(t)$ based on the frequency evolution of circular orbit waveforms with identical mass ra-

tios during the fitting of NR waveforms. The relationship $x = (M\omega_o)^{2/3} = (M\omega_w/2)^{2/3} \approx (M\omega_c/2)^{2/3}$ provides a means to derive x and, conversely, ω_o (the orbital average frequency), ω_w (waveform average frequency), and ω_c (Circular orbit waveform frequency). While slight differences exist between ω_w and the circular orbit frequency ω_c , the approximation remains accurate within a margin of ± 0.001 (for RIT:eBBH:1282) throughout the waveform's frequency evolution. As a result, the evolution of x can be approximated using the frequency of circular orbit waveforms. It is important to note that as the waveform length increases and eccentricity gradually rises, the effectiveness of this approximation diminishes, necessitating an expansion of the parameter x guess range. In FIG. 5, we illustrate this phenomenon using the wave-

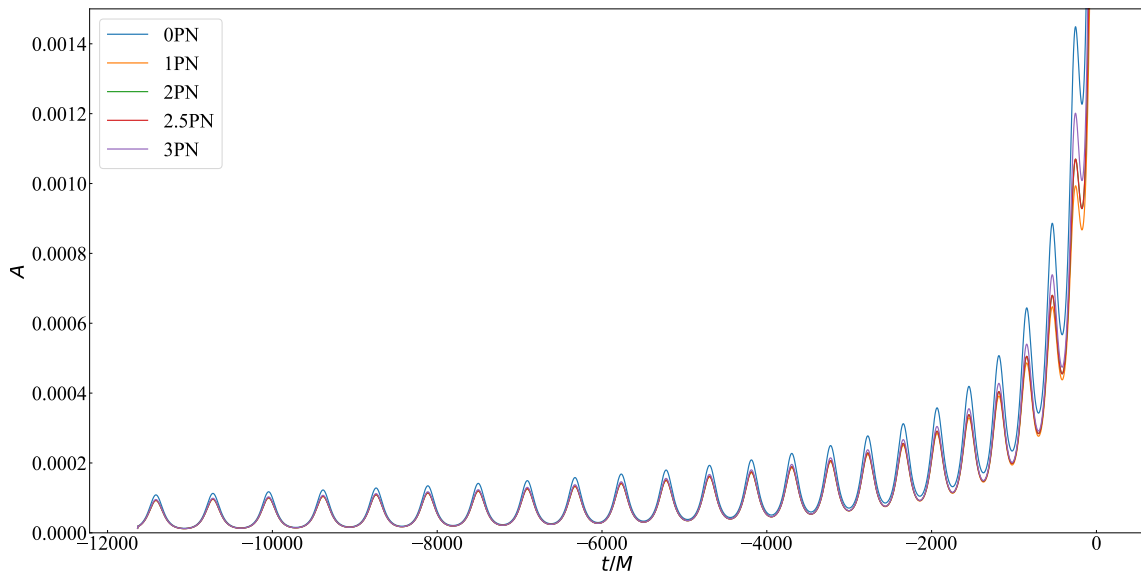


FIG. 4. Various PN orders amplitudes of Eq. (21) for waveform RIT:eBBH:1282. For instance, selecting the 2PN order entails the inclusion of the preceding Newtonian order, the 1PN order, and so forth.

form RIT:eBBH:1282, spanning approximately $12000M$, alongside a corresponding circular orbit waveform with $q = 1$ generated by the SEOBNRv4 code in Pycbc [108]. This comparison underscores the constraints of the parameter x guess range. FIG. 5 showcases the RIT waveform and its PN fit, along with the average frequency ω_w derived from x , and the SEOBNRv4 waveform for a mass ratio of $q = 1$ from Pycbc. To further validate the accuracy of the SEOBNRv4 waveform, we also include the circular orbit waveform SXS:BBH:0180, albeit shorter in duration than SEOBNRv4, provided here solely for comparison. When utilizing the SEOBNRv4 waveforms from Pycbc, we convert their units from the International System of Units (SI) to the Natural System of Units. As depicted in FIG. 5, although the frequency of the circular orbit waveform and the orbit-averaged frequency for the same mass ratio are not perfectly aligned, the discrepancy is minimal. This slight distinction is why some studies [109, 110] directly utilize the circular orbit waveform as an approximation for the average frequency of eccentric waveforms. The methodology of estimating the orbital average frequency using a circular orbit waveform is pertinent not only for nonspinning waveforms but also for spin-aligned waveforms, provided waveforms with the same mass ratio and spin characteristics are employed, as detailed in our prior study [111].

Moreover, in the case of e_{t_0} , it is not feasible to simply assign a range of $[0, 1]$ due to the potential occurrence of infinite or negative values under the square root at high eccentricities in the process of PN fitting. Both RIT and SXS have developed proprietary methods for assessing eccentricity within their datasets, providing a valuable reference point. By leveraging these eccentricities, typically falling within a range of approximately ± 0.1 , we can establish an initial guess range for eccentricity. This

strategy helps alleviate issues linked to unbounded ranges and enhances the robustness of the fitting process.

Additionally, for l_0 , we can consider the range $[0, 6.5]$, recognizing that due to periastron precession, the value of l_0 may exceed 2π . Furthermore, we can refine the range of l_0 based on the variation in frequency ϖ at periastron and apastron.

When determining the initial guess parameter range, a strategy akin to Newton’s bisection method can be utilized. Initially, we can select 10 initial guess parameters, for example, $e_{t_0} \in [0.1, 0.2, 10]$, where 10 denotes the number of eccentricity divisions, and progressively fine-tune the guess range for the initial parameters. Following an iteration, this process might yield $e_{t_0} \in [0.19, 0.20, 10]$. By iteratively adjusting the guess parameter range three or four times, we can derive initial parameters with sufficient accuracy while significantly reducing computational expenses. This iterative approach can be similarly applied to all three parameters: e_{t_0} , l_0 , x_0 . Once these parameters are determined, we utilize the least squares fitting method to determine the initial phase φ_0 , thereby fully defining all PN parameters. The results of fitting 180 sets of eccentric waveforms from RIT and SXS are elaborated in Table II in Appendix B.

D. Different methods of measuring initial eccentricity

Upon determining the PN fitting parameter e_{t_0} from the NR waveform, we establish a method to quantify the eccentricity of the NR waveform. The accuracy of this approach relies on the radiation and conservation dynamics at the 3PN order. It is noteworthy that within general relativity, a gauge-invariant definition of eccentric-

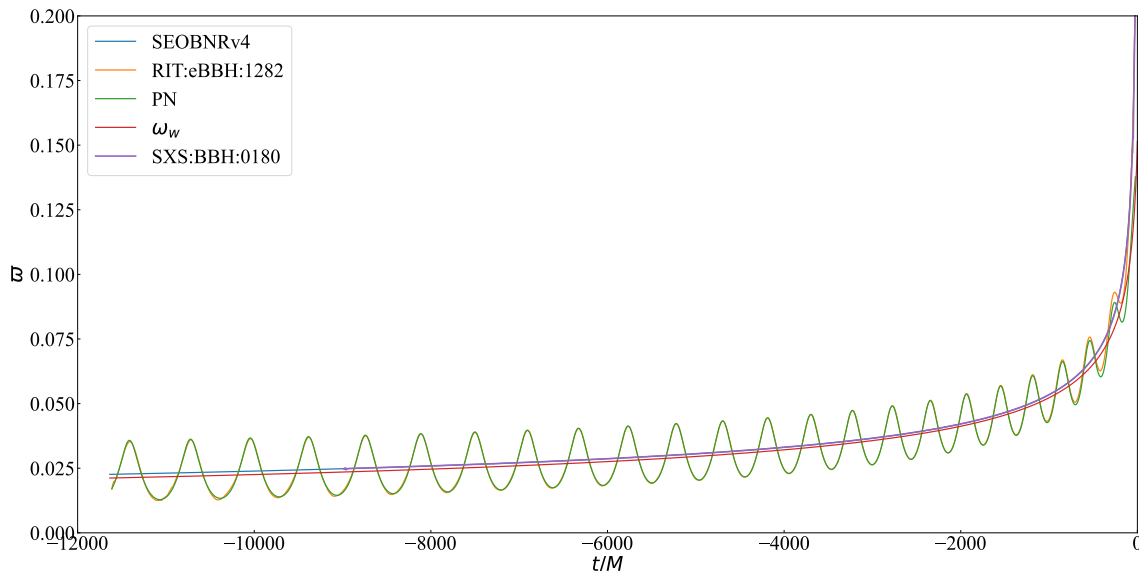


FIG. 5. Frequency of the waveform RIT:eBBH:1282 and its PN fitting, average orbital frequency ω_w , alongside a corresponding circular orbit waveform with $q = 1$ generated by the SEOBNRv4 code in Pycbc. To further validate the accuracy of the SEOBNRv4 waveform, we also include the circular orbit waveform SXS:BBH:0180.

ity is lacking; nevertheless, various references [109, 112–114] have introduced diverse methodologies to gauge the orbital eccentricity of BBH in eccentric orbits. In NR simulations, two primary techniques are utilized to determine the orbital eccentricity of BBH systems. One method involves analyzing the waveform’s features, such as frequency oscillations, phase variations, and amplitude changes, to infer the eccentricity. However, this method is constrained in capturing only local waveform oscillations, primarily at lower PN and Newtonian orders, thus leading to notable errors in eccentricity estimation. Conversely, the second method relies on assessing the orbital energy and angular momentum to ascertain the initial orbital eccentricity of the BBH system. In this study, we concentrate solely on the latter method of eccentricity calculation, which entails deriving the initial eccentricity of a BBH system through its orbital energy and angular momentum. By contrasting the PN fit parameter e_{t_0} with the initial eccentricities obtained from this method and the existing initial eccentricity data from the RIT and SXS catalogs, we aim to discern any discrepancies between them.

For nonspinning systems, following the methodology outlined in Refs. [115] and [116], we utilize the generalized 3PN quasi-Keplerian parameterization to estimate the initial eccentricity. The initial eccentricity e_{t_0} can be determined utilizing the expression given in Eq. (25e) of Ref. [75] under harmonic coordinates. For conciseness, Eq. (25e) is provided in Appendix A. The key parameters necessary for computing eccentricity in Eq. (25e) are the initial binding energy E_b and the initial angular momentum L , both of which are available in the metadata of the RIT and SXS catalogs. The binding energy

can be calculated as

$$E_b = M_{\text{ADM}} - M, \quad (65)$$

where M_{ADM} denotes the ADM mass.

For spin-aligned systems, we utilize Eq. (75) from Ref. [77], detailed in Appendix A, which provides an expression precise up to the 2PN order in ADM coordinates. While this equation is accurate up to the 2PN order in ADM coordinates, the similarity of eccentricity values computed in ADM coordinates using Eq. (75) with those determined in harmonic coordinates based on the fitting outcomes of the nonspinning waveform from Ref. [115] and the PN fitting in this study indicates minimal discrepancies. The difference between the 2PN and 3PN orders is also slight, with errors in both cases being only 0.001, mirroring the precision of our eccentricity estimation through PN fitting. Notably, Ref. [78] offers a calculation of the eccentricity e_{t_0} at the 3PN order; however, due to potential inaccuracies in its calculation formula, achieving the correct result is unattainable, thereby rendering its findings unsuitable for this study.

Both the SXS and RIT catalogs present their independently measured eccentricities; however, the precision of these values remains uncertain due to the differing methodologies employed by each catalog. The eccentricity measurement technique introduced by RIT, elaborated in Ref. [67], is notably straightforward, with its accuracy extensively scrutinized therein. The process of generating eccentric waveforms and measuring eccentricity unfolds as follows: A novel parameter ϵ within the range of 0 to 1 is introduced, adjusting the tangential linear momentum as $p_t = p_{t,qc}(1 - \epsilon)$, where $p_{t,qc}$ denotes the tangential linear momentum in a quasicircular orbit. In this approach, the initial positions of the binary black

hole remain fixed at apastron, while the initial orbital eccentricity gradually increases during the simulations, transitioning from a quasi-circular orbit ($e = 0$) towards the head-on collision limit ($e = 1$). The corresponding initial orbital frequency (including the 22-mode of gravitational waves) decreases by the factor $\omega_{o,e} = \omega_{o,qc}(1-\epsilon)$. Consequently, the initial eccentricity of the orbit can be approximated as $e = 2\epsilon - \epsilon^2$, providing a second-order approximation with respect to ϵ . The SXS catalog does not explicitly outline its eccentricity measurement method in Refs. [62, 63].

III. RESULTS

A. Fitting residuals

The residual fitting between PN and NR data can potentially be influenced by various factors such as mass ratio, spin, eccentricity, waveform length, and more. Our fitting insights suggest the following outcome: The fitting residual is primarily linked to the eccentricity of the system, with mass ratio or spin playing a secondary role, and showing no significant correlation with other factors. A decrease in eccentricity results in a reduced fitting residual, while an increase in eccentricity leads to an increased fitting residual. This implies that a very long waveform with low eccentricity, like RIT:eBBH:1282, exhibits a small fitting residual due to the consistency between PN and NR data. On the other hand, an increase in the fitting residual indicates a decrease in the accuracy of PN approximations compared to NR. This loss in accuracy can be attributed to the heightened impact of strong-field effects in NR simulations as eccentricity increases, exacerbating the limitations of PN approximations.

In FIG. 6, we present the residuals from PN fitting of all the eccentric waveforms from RIT and SXS shown in FIG. 1, encompassing waveforms with varying mass ratios, different eccentricities, and both nonspinning and spin-aligned configurations. In FIG. 6, although the graphs appear in four distinct panels, they illustrate the same data, with variations reflecting the different research contexts.

In panel (a) of FIG. 6, we illustrate the variation of the fitting residual with the mass ratio q . It may seem puzzling why the fitting residual correlates with the mass ratio, as the accuracy of the waveform ideally should remain unaffected by the mass ratio, whether in PN or NR simulations. Historically, NR simulated waveforms have been regarded as the most accurate compared to PN and EOB approximations. However, NR simulations may not be entirely error-free and could contain distinct inaccuracies, such as numerical errors. In panel (a), it becomes evident that as the mass ratio decreases, so does the fitting residual. This trend holds true for both the RIT and SXS catalogs. For specific values, please consult Appendix A. Essentially, the software codes EinsteinToolkit

and SpEC, commonly used for numerical simulations, exhibit the highest accuracy when the mass ratio is unity during the simulation of BBH mergers in eccentric orbits. Conversely, as the mass ratio decreases, the margin of error widens. In NR simulations, a lower mass ratio results in a longer waveform under identical initial conditions, necessitating a finer numerical simulation grid for increased accuracy. The increased fitting residual in panel (a) suggests that NR waveforms incur a more significant error in scenarios involving small mass ratios, as supported by findings in Ref. [22], which also conducts a comparison of PN and NR involving small mass ratios. In Sec. III E, we will analyze waveforms with small mass ratios from RIT as case studies to elucidate the potential challenges and implications of PN fitting in scenarios with small mass ratios.

In panel (b) of FIG. 6, we have depicted the impact of waveform length on the PN fitting residuals. The color bar in panel (b) represents the duration of the waveform, spanning from the initial time to the merger point. One might expect that the PN fitting residual correlates with the length of the waveform. Surprisingly, this is not the case. It is clear that the length of the waveform has minimal influence on the fitting residuals. The majority of waveforms we analyze are short, typically ranging from approximately 1000M to 2000M in length. Some exhibit significant eccentricities, resulting in larger fitting residuals, while others with lower eccentricities yield smaller residuals. Among a few elongated waveforms, the longest extends beyond 16000M. Despite this extended duration, its fitting residual remains moderate due to its intermediate eccentricity level. This observation highlights that PN fitting residuals are not tied to waveform length, or any correlation is very weak.

In panel (c) of FIG. 6, we showcase the impact of different catalogs on PN fitting residuals. The trends in the fitting residuals of RIT and SXS are notably similar, suggesting that distinct catalogs or computational codes have minimal effects on PN fitting. RIT and SXS have previously cross-validated their simulated waveforms in earlier studies, leading to a high level of agreement between them.

In panel (d) of FIG. 6, we explore the effect of spin alignment and no spin on the PN fitting residual. The scatter points in both scenarios display a similar overall trend, with a slight elevation observed in the scatter points for spin alignment compared to those without spin. This discrepancy can be attributed to the influence of spin on waveform characteristics. However, the difference between the two scenarios is marginal and can be nearly disregarded. Further investigations involving a broader range of spin-aligned eccentric waveforms will provide a more thorough analysis in future research. Thus, it can be concluded that the presence or absence of nonprecessing spin has a negligible effect on the PN fitting residual. For precise values, please consult the detailed PN fitting data in Appendix B.

In summary, the analysis of FIG. 6 leads us to the con-

clusion that the PN fitting residual is primarily linked to the eccentricity of the waveforms. A clear trend emerges indicating that as eccentricity increases, so does the fitting residual. This increase in the fitting residual indicates a decrease in the accuracy of PN approximations compared to NR. This decline can be attributed to the heightened impact of strong-field effects in NR simulations as eccentricity rises, exacerbating the limitations of the PN approximation. While the mass ratio does have a minor influence on the fitting residual, this effect is primarily due to inherent limitations within the NR simulations. Additionally, our findings suggest that variations in numerical simulation codes and spin configurations do not significantly impact the fitting residual.

B. Initial eccentricity

In the preceding Section IID, we introduced the non-spinning quasi-Keplerian parameterization at 3PN orders and the spin-aligned quasi-Keplerian parameterization at 2PN orders for quantifying the initial eccentricity based on the initial energy and orbital angular momentum. Furthermore, we emphasized that both RIT and SXS have autonomously derived their individual initial eccentricity values.

As previously discussed, there is no definitive standard for measuring eccentricity, leading to the absence of a universally accepted method. Consequently, it is difficult to claim the superiority of any specific approach for determining eccentricity. Generally, as eccentricity increases, so does the margin of error in its measurement. In this study, we focus on evaluating the relative discrepancies between two eccentricity measurement methods and the PN fitting eccentricity, e_{t0} . The initial eccentricity, determined using the quasi-Keplerian parameterization based on initial energy and orbital angular momentum, is denoted as e_{t0KP} . The absolute error of it with respect to e_{t0} is expressed as:

$$\varepsilon_{KP} = |e_{t0KP} - e_{t0}|. \quad (66)$$

We chose not to calculate the relative error by dividing by e_{t0} because of the potential for significant discrepancies between e_{t0KP} and e_{t0} , which could yield large numerical differences that might obscure meaningful interpretation in a plot. For detailed numerical values of e_{t0KP} and e_{t0} , please refer to Appendix B. The initial eccentricity measured by the RIT catalog is denoted as e_{t0RIT} , and the absolute error compared to e_{t0} is given by:

$$\varepsilon_{RIT} = |e_{t0RIT} - e_{t0}|. \quad (67)$$

Similarly, the initial eccentricity measured by the SXS catalog is denoted as e_{t0SXS} , with the absolute error relative to e_{t0} defined as:

$$\varepsilon_{SXS} = |e_{t0SXS} - e_{t0}|. \quad (68)$$

In FIG. 7, we present the absolute errors between the eccentricities determined by the two aforementioned methods and those obtained through PN fitting. Panel (a) corresponds to the nonspinning configuration, while panel (b) pertains to the spin-aligned configuration.

From panel (a), which focuses on the nonspinning configuration, we observe that the absolute errors of all three measurement methods increase with eccentricity e_{t0} . Among these methods, the eccentricity measured by RIT, e_{t0RIT} , exhibits the closest agreement with PN fitting, followed by the quasi-Keplerian parameterization, e_{t0KP} , while the SXS measurements, e_{t0SXS} , show the largest deviations. Detailed data from the RIT catalog and Appendix B reveal that the RIT eccentricity measurements exhibit smooth, continuous behavior without abrupt fluctuations, maintaining close alignment with PN fitting results across a wide range of eccentricities [74]. For e_{t0RIT} , the absolute error with respect to PN fitting remains within 0.025 for low and moderate eccentricities (0-0.4) and within 0.05 for intermediate eccentricities (0.4-0.45). In contrast, measurements using the e_{t0KP} method display significant errors at very low eccentricities, a known limitation of the approach. This method may produce eccentricity that deviate by more than 1 at both very low and very high eccentricities (around 0.9), making it unreliable in these extreme cases. For e_{t0KP} , the absolute error relative to PN fitting in the low eccentricity range (0-0.2) is approximately 0.025-0.075, though in other eccentricity ranges, the e_{t0KP} results align more closely with RIT and PN measurements. Regarding the SXS measurements, e_{t0SXS} , the absolute error for low eccentricities (0-0.1) ranges between 0 and 0.04, but for higher eccentricities, the errors become too significant to be considered reliable. Moreover, the SXS catalog lacks complete measurement data for some waveforms, further contributing to the uncertainties in these assessments.

In panel (b), which examines the spin-aligned configuration, the trends in absolute errors mirror those observed for the nonspinning case. However, the absolute errors are more pronounced for medium eccentricities in the spin-aligned configuration. Specifically, for e_{t0KP} , the maximum error exceeds 0.08, while for e_{t0RIT} , the maximum error surpasses 0.12. These findings highlight an increasing lack of reliability in all three measurement methods as spin effects become more pronounced, further underscoring the influence of spin on eccentricity assessments.

C. Dominant mode

In this section, we present the PN fitting results for the dominant 22 mode, with higher modes discussed in the following section. We use three sets of nonspinning and three sets of spin-aligned waveforms with increasing initial eccentricity to illustrate the PN fitting results for frequency, phase, and amplitude. A note-

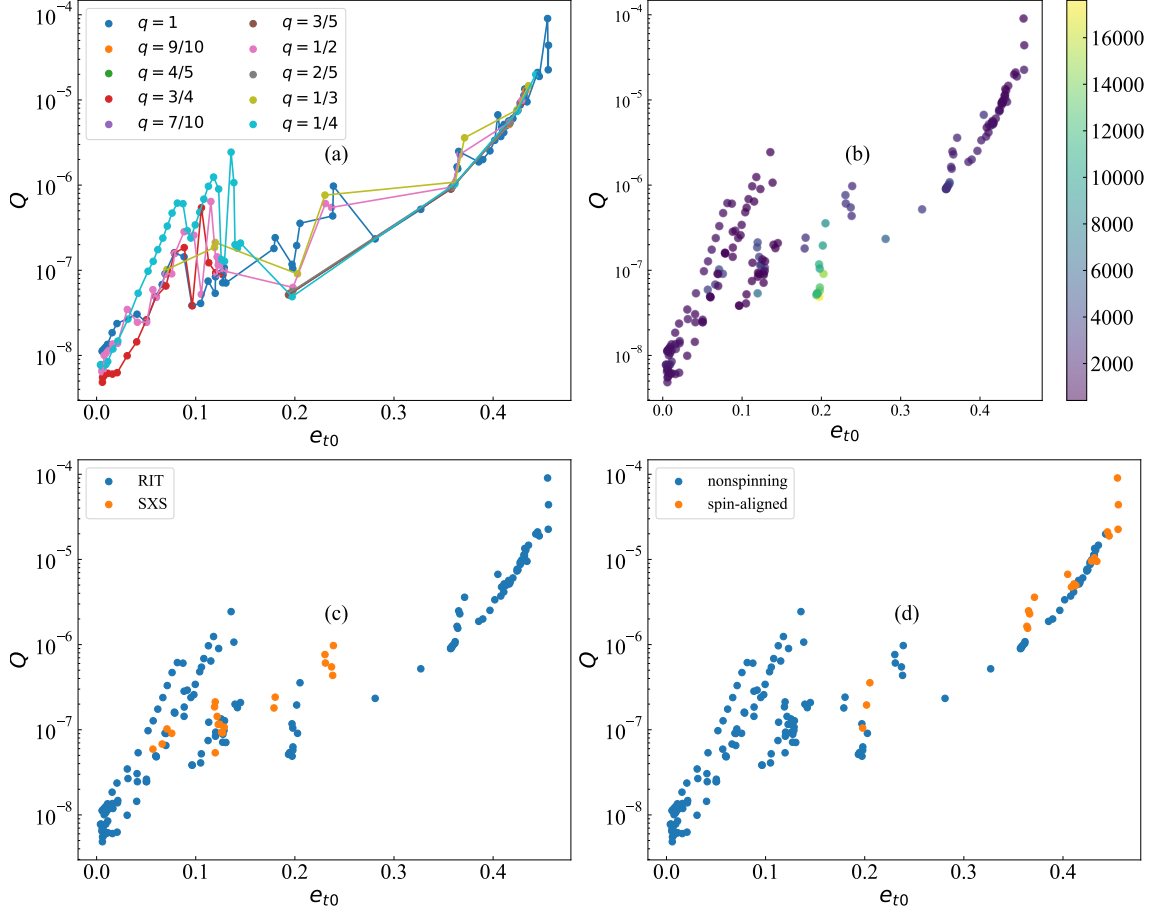


FIG. 6. Residuals obtained from PN fitting of all the eccentric waveforms of RIT and SXS in FIG. 1, encompassing waveforms with varying mass ratios, different eccentricities, different waveform lengths and both nonspinning and spin-aligned configurations.

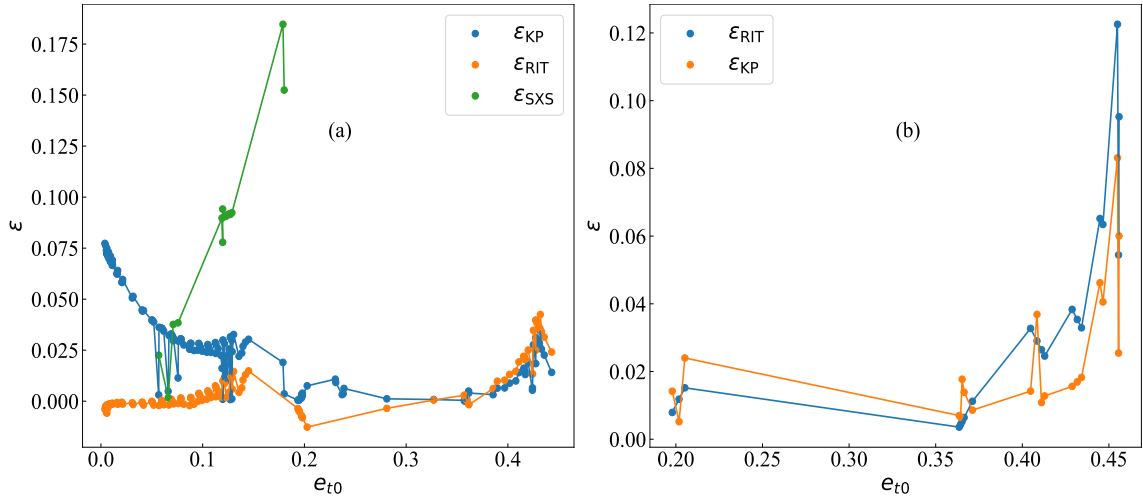


FIG. 7. Absolute errors between the eccentricities determined by quasi-Keplerian parameterization, RIT and SXS catalogs and those obtained through PN fitting. Panel (a) in corresponds to the nonspinning configuration, while panel (b) pertains to the spin-aligned configuration.

worthy feature of these waveform sets is that they differ only in their initial eccentricities, while all other parameters, such as mass ratio, initial separation, and spin remain identical and constant. The six waveforms are nonspinning cases RIT:eBBH:1330, RIT:eBBH:1331, RIT:eBBH:1332, and spin-aligned cases RIT:eBBH:1899, RIT:eBBH:1900, RIT:eBBH:1901. Detailed fitting parameters for these waveforms can be found in Appendix A.

In FIG. 8, we display the frequency, phase, and amplitude of three nonspinning waveforms: RIT:eBBH:1330 (panels (a), (d), (g)), RIT:eBBH:1331 (panels (b), (e), (h)), and RIT:eBBH:1332 (panels (c), (f), (i)), along with their corresponding PN fits. Similarly, FIG. 9 presents the frequency, phase, and amplitude of three spin-aligned waveforms: RIT:eBBH:1899 (panels (a), (d), (g)), RIT:eBBH:1900 (panels (b), (e), (h)), and RIT:eBBH:1901 (panels (c), (f), (i)), also with their PN fits. In both figures, we consider only the leading Newtonian order for the amplitude, as discussed in Sec. II C, which yields the most accurate fits compared to higher-order moments. Both FIGs. 8 and 9 reveal a clear trend: as eccentricity increases, the quality of the fitting decreases, as indicated by the larger fitting residuals in FIG. 6. Higher eccentricities result in more pronounced deviations near periastron, where local maxima are observed in the figures, highlighting the significant influence of the strong-field effects in NR within this region. Another consistent observation across all panels of FIGs. 8 and 9, regardless of eccentricity, is the notable deviation between PN and NR starting approximately $200M$ before the merger. This divergence is inherent to the nature of PN and NR, with the strong-field effects of NR dominating as PN gradually loses its accuracy approaching the merger.

The direct PN fitting results shown in FIGs. 8 and 9 do not provide a clear quantitative measure of the error between PN fits and NR waveforms. To address this, we introduce new metrics to describe these differences more precisely. We define the frequency relative error as:

$$\frac{|\delta\varpi|}{\varpi_{\text{NR}}} = \left| \frac{\varpi_{\text{PN}} - \varpi_{\text{NR}}}{\varpi_{\text{NR}}} \right| \times 100\%, \quad (69)$$

the phase absolute error as:

$$|\delta\varphi| = |\varphi_{\text{PN}} - \varphi_{\text{NR}}|, \quad (70)$$

and the amplitude relative error as:

$$\frac{|\delta A|}{A_{\text{NR}}} = \left| \frac{A_{\text{PN}} - A_{\text{NR}}}{A_{\text{NR}}} \right| \times 100\%, \quad (71)$$

These metrics provide a quantitative description of the differences between PN fitting and NR waveforms.

In FIG. 10, we present the frequency relative error $\frac{|\delta\varpi|}{\varpi_{\text{NR}}}$, phase absolute error $|\delta\varphi|$, and amplitude relative error $\frac{|\delta A|}{A_{\text{NR}}}$ for three sets of nonspinning waveforms: RIT:eBBH:1330 (panel (a), (d), (g)), RIT:eBBH:1331

(panel (b), (e), (h)), and RIT:eBBH:1332 (panel (c), (f), (i)). FIG. 11 displays the corresponding frequency relative error $\frac{|\delta\varpi|}{\varpi_{\text{NR}}}$, phase absolute error $|\delta\varphi|$, and amplitude relative error $\frac{|\delta A|}{A_{\text{NR}}}$ for three sets of spin-aligned waveforms: RIT:eBBH:1899 (panel (a), (d), (g)), RIT:eBBH:1900 (panel (b), (e), (h)), and RIT:eBBH:1901 (panel (c), (f), (i)).

From FIGs. 10 and 11, we observe that these errors oscillate over time, which contrasts with the behavior seen in circular orbits. In circular orbits, the frequency, phase, and amplitude increase monotonically over time, leading to a monotonic difference between PN and NR. However, in eccentric orbits, the frequency, phase, and amplitude oscillate, which causes the differences between PN and NR to oscillate as well. This oscillation spans the entire time range, as evidenced by the patterns in FIGs. 10 and 11. Moreover, when viewed over shorter time intervals, these oscillations exhibit no clear regularity, sometimes the error is large, and other times it is nearly zero, making it difficult to accurately describe the error between PN and NR at any specific frequency or time. As eccentricity increases, the errors in all panels for frequency, phase, and amplitude exhibit an upward trend, with oscillations becoming more pronounced. In panel (a) of FIG. 10, the relative frequency error fluctuates between 0% and 6%, increasing near the merger but remaining stable until approximately $200M$ before the merger. In panel (b), the error ranges from 0% to 15%, with local increases potentially due to waveform artifacts that introduce fluctuations (these artifacts arise from taking the second derivative of h to obtain Ψ_4). Panel (c) shows errors between 0% and 20%. In panel (d), the absolute phase error remains around 0 to 0.3 before the merger, while panel (e) shows an error around 0.4. Panel (f) exhibits a phase error under 0.5. The relative amplitude error in panel (g) stays below 25%, while in panels (h) and (i), it fluctuates within 20% and 35%, respectively. FIG. 11 shows similar trends to FIG. 10, but with noticeably larger frequency, phase, and amplitude errors in each panel. This discrepancy between FIG. 10 and FIG. 11 may result from lingering inconsistencies between local PN and NR frameworks, or it could indicate that the spin-aligned PN waveform lacks the necessary precision.

From the preceding analysis, it is clear that the oscillatory errors in frequency, phase, and amplitude, as depicted in FIGs. 10 and 11, cannot be accurately represented by singular values at specific moments in time. A measurement at any given moment could coincide with the trough of an oscillation, yielding a lower error, or it could align with the peak, resulting in a higher error. In such cases, drawing definitive conclusions is difficult. To address this, we calculate average errors over the entire time span, excluding the region where PN fails, specifically, from $200M$ before the merger. The average errors in frequency, phase, and amplitude are denoted as $\frac{|\delta\varpi|}{\varpi_{\text{NR}}}$, $|\delta\varphi|$, and $\frac{|\delta A|}{A_{\text{NR}}}$. In FIGs. 10 and 11, we mark the $-200M$ point, corresponding to a frequency near 0.1. FIGs. 10

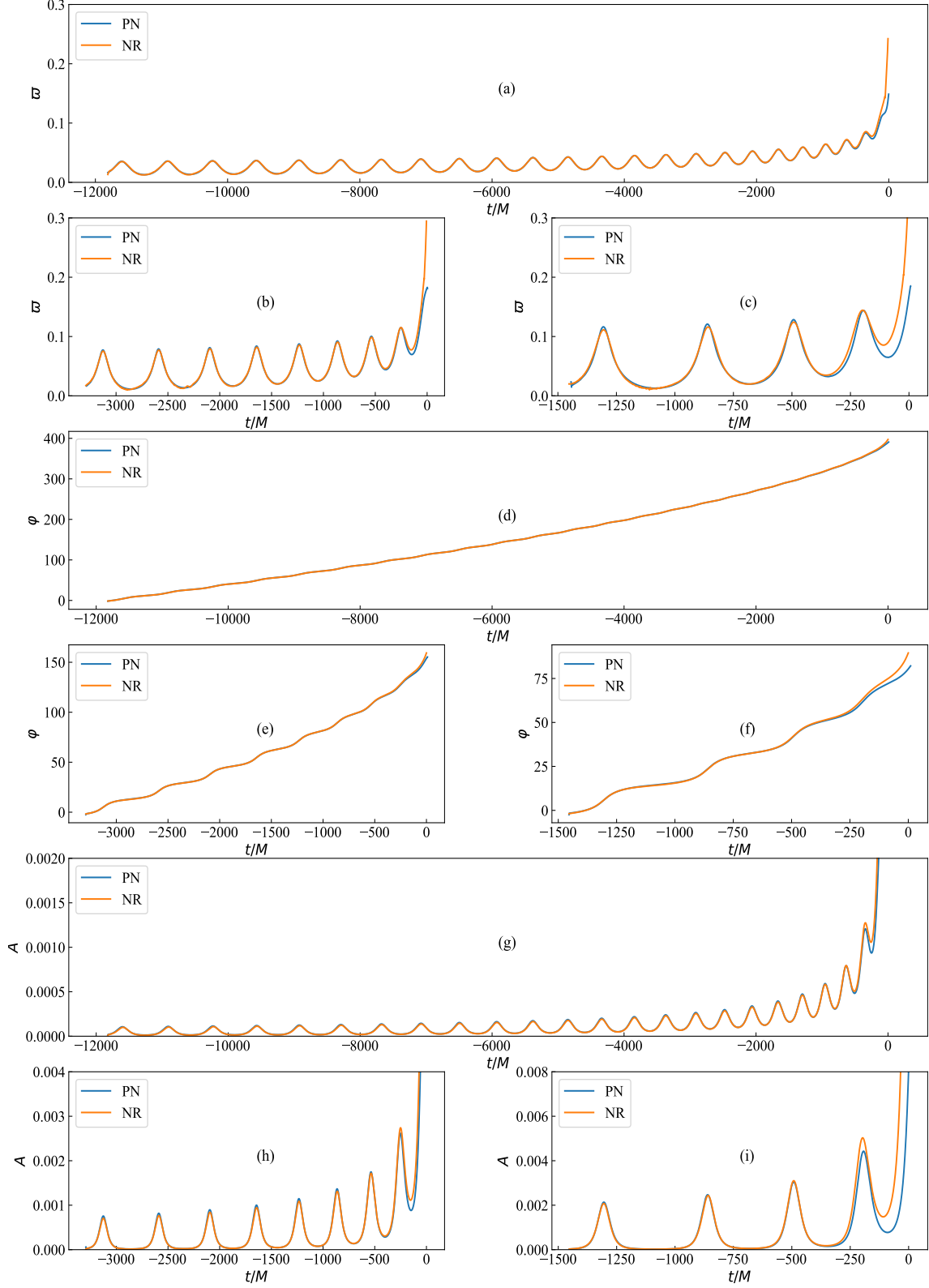


FIG. 8. Frequency, phase, and leading Newtonian order amplitude of three sets of nonspinning waveforms RIT:eBBH:1330 (panel (a), (d), (g)), RIT:eBBH:1331 (panel (b), (e), (h)), RIT:eBBH:1332 (panel (c), (f), (i)), along with their PN fitting.

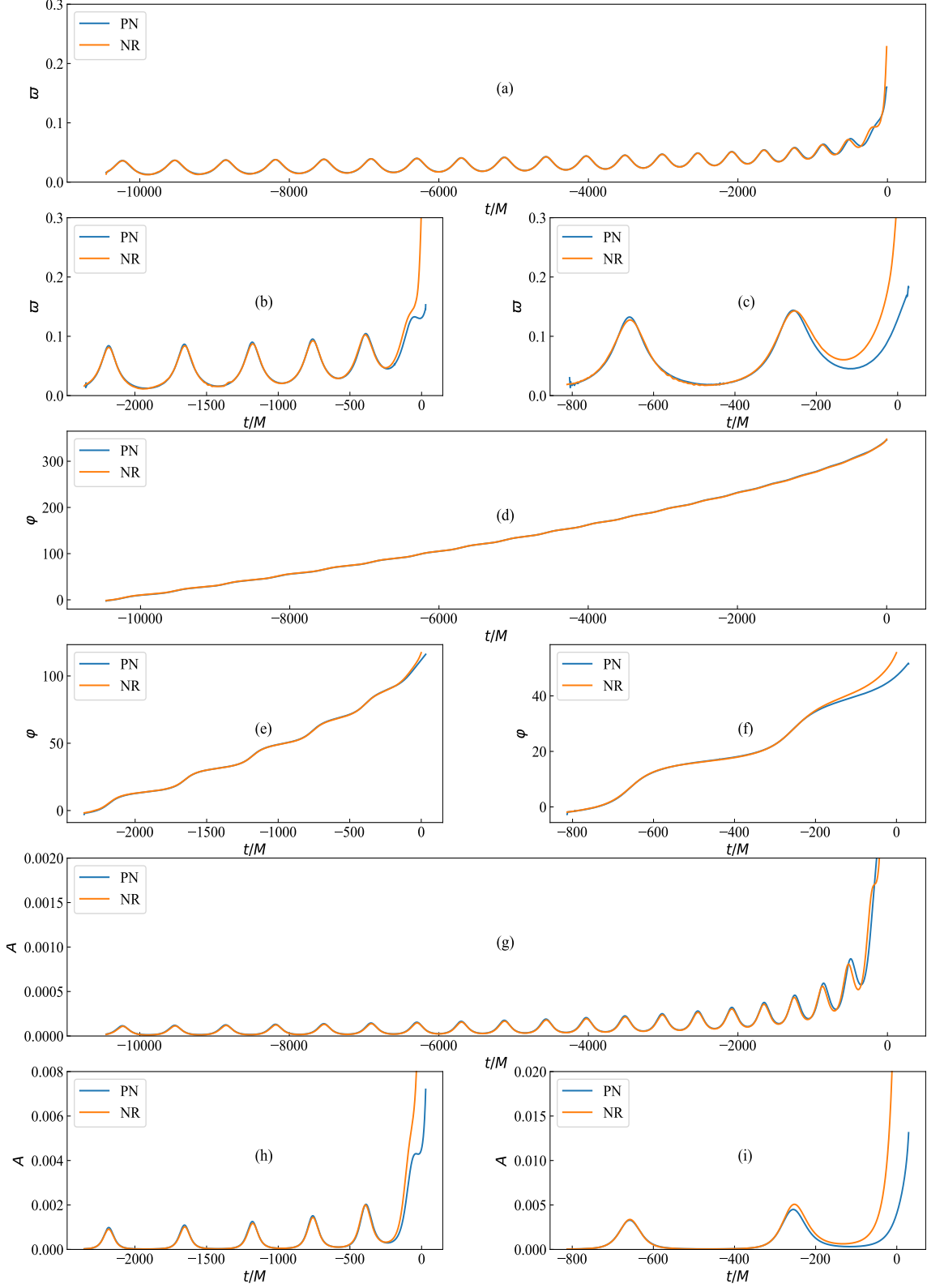


FIG. 9. Frequency, phase, and leading Newtonian order amplitude of three sets of spin-aligned waveforms RIT:eBBH:1899 (panel (a), (d), (g)), RIT:eBBH:1900 (panel (b), (e), (h)), RIT:eBBH:1901 (panel (c), (f), (i)), also accompanied by their PN fitting.

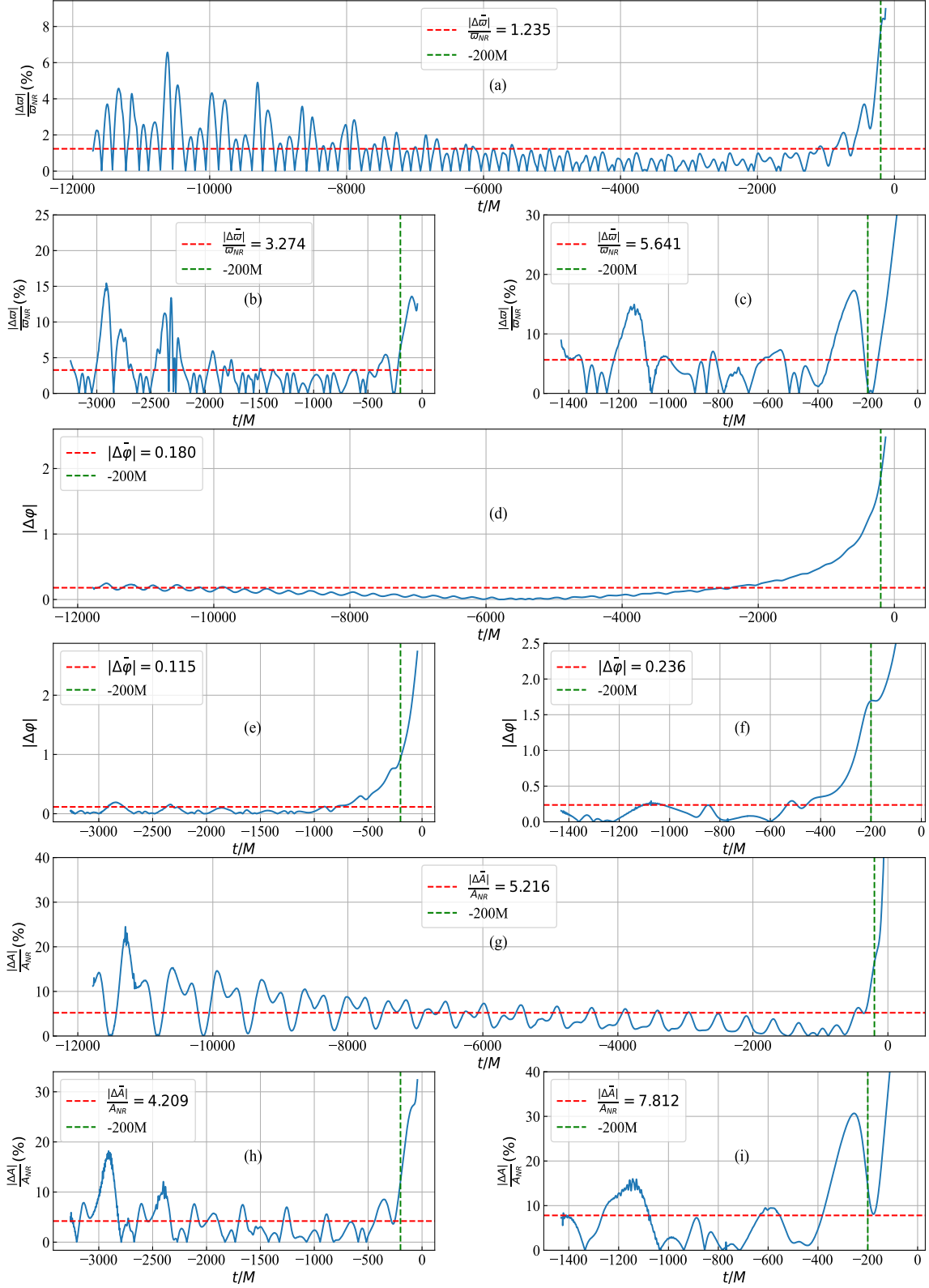


FIG. 10. Frequency relative error $\frac{|\delta\omega|}{\omega_{NR}}$, phase absolute error $|\delta\phi|$, and amplitude relative error $\frac{|\delta A|}{A_{NR}}$ of three sets of nonspinning waveforms RIT:eBBH:1330 (panel (a), (d), (g)), RIT:eBBH:1331 (panel (b), (e), (h)), RIT:eBBH:1332 (panel (c), (f), (i)). The horizontal red line represents their average value, and the vertical green line represents time $-200M$.

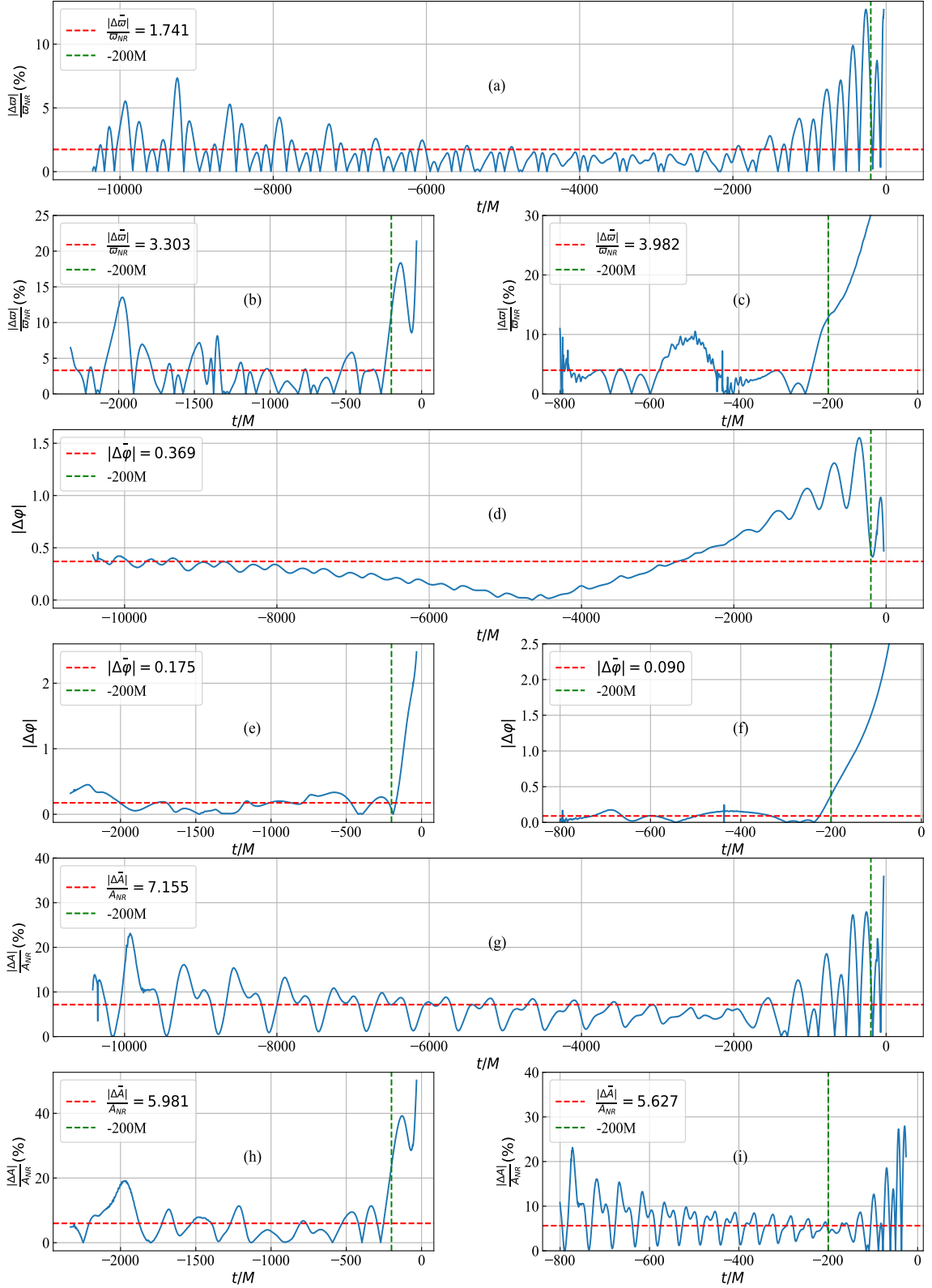


FIG. 11. Frequency relative error $\frac{|\delta\vec{\omega}|}{\omega_{NR}}$, phase absolute error $|\delta\phi|$, and amplitude relative error $\frac{|\delta A|}{A_{NR}}$ of three sets of spin-aligned waveforms RIT:eBBH:1899 (panel (a), (d), (g)), RIT:eBBH:1900 (panel (b), (e), (h)), RIT:eBBH:1901 (panel (c), (f), (i)). The horizontal red line represents their average value, and the vertical green line represents time $-200M$.

and 11 show the average errors for frequency, phase, and amplitude for the six waveforms, providing a qualitative measure of their magnitudes. The exact average error values are annotated in these figures, offering a comprehensive and quantitative depiction of error across the datasets by averaging over the oscillations. These averages, positioned at the midpoint of the oscillations, serve as a balanced metric for assessing error. From FIGs. 10 and 11, we observe that the average error values generally increase with eccentricity, though occasional decreases may occur, potentially due to factors such as waveform length influencing the fitting process and some other numerical errors. It is important to note that phase represents the integral of frequency, meaning that phase errors accumulate over time. Consequently, the phase difference is affected by the length of the waveform. However, in the context of eccentricity-induced oscillations, relying solely on phase error as a precise metric is challenging due to the complexity of these oscillations. The three average errors we employ here should be viewed as reference values rather than definitive measures, as the errors at specific times can significantly exceed the average error magnitude.

As highlighted in Sec. IIB, we have performed PN fitting on a comprehensive set of 180 eccentric NR waveforms. Given the extensive nature of these results, presenting detailed figures for each case would be impractical. Therefore, in FIG. 12, we provide the average errors in frequency, phase, and amplitude across these 180 waveforms as quantitative metrics to assess their accuracy. We also distinguish between the errors for RIT and SXS waveforms, as well as between nonspinning and spin-aligned RIT waveforms, and waveform length.

In panel (a) of FIG. 12, we show the relationship between the average relative amplitude error, $\frac{|\delta A|}{A_{NR}}$, and eccentricity e_{t0} . The error increases gradually with rising eccentricity. For eccentricities between 0 and 0.2, the maximum error reaches 6%. In the eccentricity range of 0.2 to 0.4, differences emerge between nonspinning and spin-aligned waveforms: for nonspinning, $\frac{|\delta A|}{A_{NR}}$ ranges from 5% to 7.5%, while for spin-aligned waveforms, it ranges from 6% to 10%. At higher eccentricities, the amplitude error surpasses 10%.

Panel (b) of FIG. 12 presents the evolution of the average relative frequency error, $\frac{|\delta \omega|}{\omega_{NR}}$, as a function of eccentricity. Similar to the amplitude error, the frequency error increases with eccentricity. In the 0 to 0.2 range, $\frac{|\delta \omega|}{\omega_{NR}}$ ranges between 0% and 2%. For eccentricity between 0.2 and 0.4, the nonspinning case shows frequency errors between 2% and 6%, while the spin-aligned case exhibits errors between 2% and 8%. For eccentricities beyond 0.4, the frequency error exceeds 8%. Overall, the frequency error is generally smaller than the amplitude error.

In panel (c) of FIG. 12, we examine the average phase error, $|\delta \varphi|$, as a function of initial eccentricity e_{t0} . For nonspinning cases with eccentricities between 0 and 0.2,

the phase error ranges from 0 to 0.2. As eccentricity increases to between 0.2 and 0.4, $|\delta \varphi|$ ranges from 0.1 to 0.3, and for eccentricities above 0.4, it spans from 0.3 to 0.5. In the spin-aligned case, the phase error is larger than in the nonspinning case. For eccentricities between 0.2 and 0.45, $|\delta \varphi|$ fluctuates between 0.2 and 0.9, reflecting lower accuracy for spin-aligned waveforms compared to nonspinning ones.

Panel (d) of FIG. 12 explores the relationship between phase error, eccentricity, and waveform duration, with the color bar indicating waveform length. Shorter waveforms tend to exhibit lower phase errors, clustering towards the lower end of panel (d). Additionally, higher eccentricities correspond to larger phase errors for shorter waveforms, highlighting the combined influence of waveform length and eccentricity on phase accuracy.

D. Higher modes

In the previous section, we concentrated on the dominant 22 mode. In this section, we shift our focus to the PN fitting results for higher-order modes, including the 21, 33, 32, 44, 43, and 55 modes. It should be noted that the RIT catalog does not include the 55 mode, with the 44 mode being the highest one available. Unlike the 22 mode, higher-order modes do not undergo iterative fitting. Instead, we directly utilize the fitting outcome of the 22 mode as the initial parameter to generate waveforms for these higher-order modes. This approach is not intended to suggest that higher-order modes are unsuitable for fitting but rather serves to cross-check the consistency of the parameters derived from fitting the 22 mode.

Due to symmetry, not all higher-order harmonic modes exist in BBH systems. For instance, modes with odd values of m in Eq. (19) are absent in equal-mass systems. In the RIT catalog, many of the expected higher-order modes are missing, and some of the available higher-order modes display unphysical behavior, which may result from errors in the extraction or expansion of Ψ_4 .

For brevity, we do not display all the fitting results for higher-order modes here. Instead, we present a selection of the most representative waveforms. If needed, any waveform can be reproduced using the fitting parameters provided in Appendix B.

FIG. 13 presents the PN fitting results for the frequency (panels (a)–(f)), phase (panels (g)–(l)), and amplitude (panels (m)–(r)) of the higher-order modes, including the 21, 33, 32, 44, 43, and 55 modes, for waveform SXS:BBH:1364. This particular waveform was chosen for its mass ratio of $q = 1/2$ and the presence of well-behaved higher-order modes. For amplitude, we consider only the leading PN moment, following the approach used for the dominant 22 mode. This choice is motivated by its demonstrated accuracy, which will be discussed later. From FIG. 13, it is clear that the PN fitting for the frequency and phase of the higher-order modes is of compa-

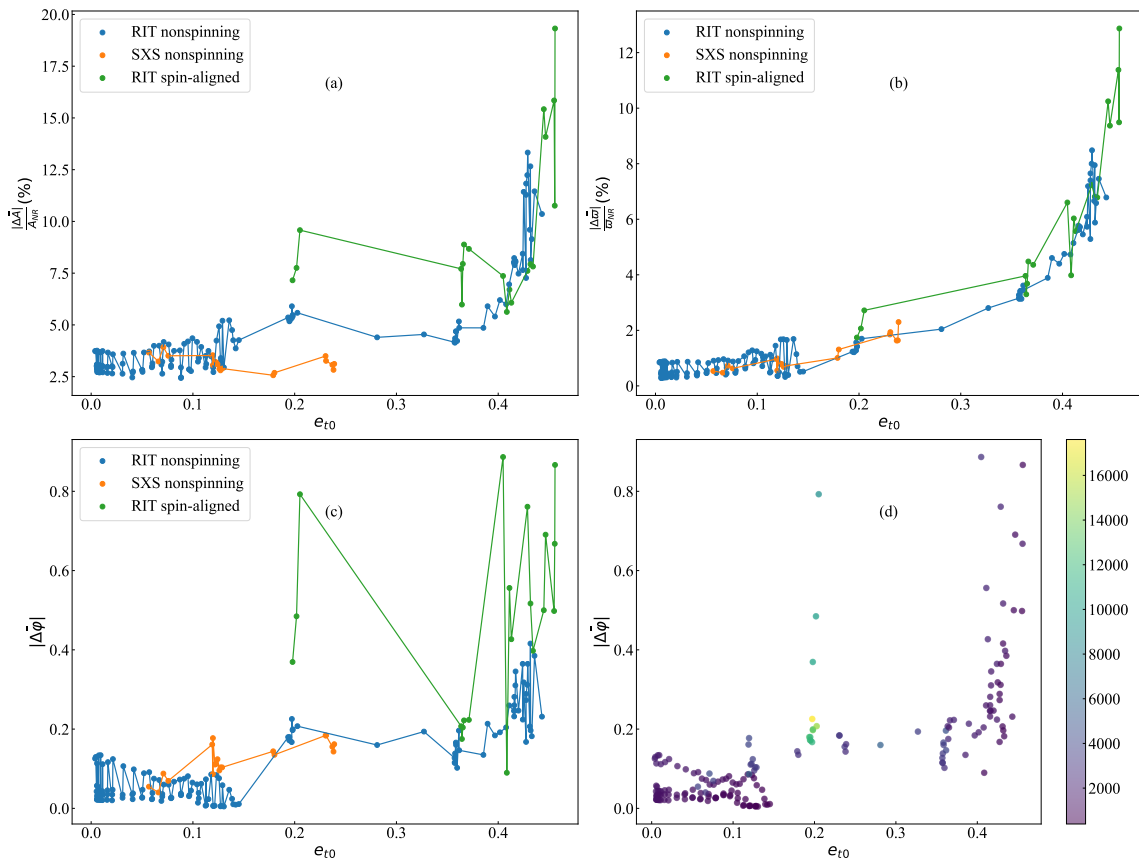


FIG. 12. Correlation between the average amplitude relative error $\frac{|\delta A|}{A_{\text{NR}}}$ (a), the average frequency relative error $\frac{|\delta \omega|}{\omega_{\text{NR}}}$ (b), and the average phase absolute error $|\delta \phi|$ (c) resulting from the PN fitting of the 22 mode and the initial eccentricity parameters e_{t0} . Panel (d) illustrates the relationship between phase error, eccentricity, and waveform duration, with the color bar denoting the length of waveforms.

rable quality to that of the dominant 22 mode. However, the amplitude fitting is less accurate and shows distinct behavior compared to the dominant mode.

In FIG. 14, we illustrate the amplitudes of various PN order moments for the higher-order modes 21 (panel (a)), 33 (panel (b)), 32 (panel (c)), 44 (panel (d)), 43 (panel (e)), and 55 (panel (f)) of the waveform SXS:BBH:1364. The amplitudes of these modes arise from different PN orders and exhibit significant variation in magnitude. Notably, A_{21} , A_{32} , and A_{43} share similar behavior, while A_{33} , A_{44} , and A_{55} display analogous patterns. Despite these variations, a common feature is that the leading-order moment produces the largest amplitude, closely approximating the values seen in NR simulations.

In contrast to the comprehensive coverage of higher-order modes in the SXS catalog, the RIT catalog provides incomplete data for these modes. Apart from the 33 and 44 modes, most higher-order modes contain disordered data that render them unsuitable for comparison. Even some instances of the 33 and 44 modes show irregularities. As a result, our comparisons are restricted to a limited number of well-behaved higher-order modes. For these modes, we present the frequency

((a), (d)), phase ((b), (e)), and amplitude ((c), (f)) PN fitting results of the 33 and 44 modes of the long waveform RIT:eBBH:1330 in FIG. 15. The fitting results for frequency and phase are comparable to those of the 22 mode shown in FIG. 8, while the amplitude fitting shows slightly worse performance.

In the spin-aligned case, the RIT catalog includes even fewer higher-order modes, with only the 44 mode available. To maintain consistency with the discussion of the 22 mode, we present in FIG. 16 the PN fitting results for the frequency (a), phase (b), and amplitude (c) of the 44 mode from waveform RIT:eBBH:1899. The results indicate that the frequency and phase fitting for the 44 mode in the spin-aligned case are similar to those of the 22 mode in FIG. 9, albeit with slightly poorer amplitude fitting. Additionally, the overall quality of the 44 mode's fitting in the spin-aligned case is slightly degraded compared to the nonspinning case.

FIGs. 13, 15, and 16 offer illustrative examples of the PN fitting results for higher-order modes, providing an intuitive understanding of the outcomes. Given the large number of waveforms analyzed, it is impractical to display all the fitting results individually. However, higher-

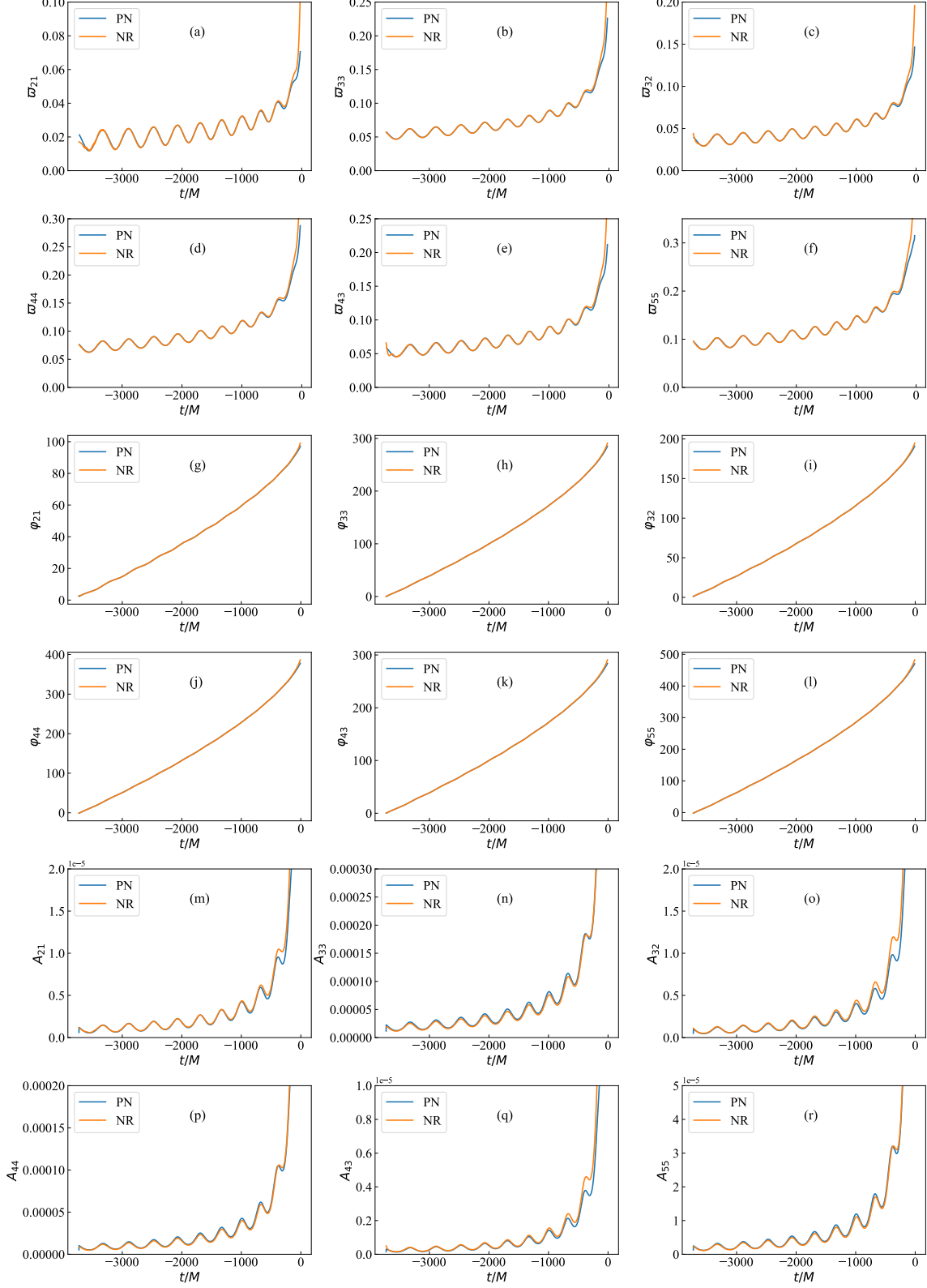


FIG. 13. PN fitting outcomes for the frequency ((a), (b), (c), (d), (e), (f)), phase ((g), (h), (i), (j), (k), (l)), and amplitude ((m), (n), (o), (p), (q), (r)) of the higher-order modes including 21, 33, 32, 44, 43, and 55 modes of the waveform SXS:BBH:1364.

order modes for any waveform can be generated using the parameters in Appendix B in conjunction with the PN equations. As with the 22 mode, we quantify the discrepancies between the PN fitting waveforms and the NR waveforms using the average amplitude relative error $\frac{|\delta \bar{A}_{\ell m}|}{A_{\ell m, \text{NR}}}$, the average frequency relative error $\frac{|\delta \bar{\omega}_{\ell m}|}{\omega_{\ell m, \text{NR}}}$, and the average phase absolute error $|\delta \bar{\varphi}_{\ell m}|$ for each higher-order mode, where ℓm represents the harmonic mode. FIG. 17 shows the relationship between the average amplitude relative error ((a), (d), (g), (j), (m), (p)), the average frequency relative error ((b), (e), (h), (k), (n), (q)), and the average phase absolute error ((c), (f), (i), (l), (o), (r)) as a function of the initial eccentricity parameter e_{t_0} .

For the average amplitude relative error $\frac{|\delta \bar{A}_{\ell m}|}{A_{\ell m, \text{NR}}}$, identifying a clear trend with eccentricity is difficult due to the narrow eccentricity range in most cases. Nevertheless, A_{21} , A_{33} , and A_{44} show an increasing trend with eccentricity, whereas the behavior of A_{32} , A_{43} , and A_{55} is less discernible. The amplitude A_{21} has the smallest error and A_{44} the largest. In general, the errors in RIT waveforms exceed those in SXS waveforms, and errors in the spin-aligned scenario are larger than in the non-spinning case. Specific error values are presented in FIG. 17.

For the average frequency error $\frac{|\delta \bar{\omega}_{\ell m}|}{\omega_{\ell m, \text{NR}}}$, all higher-order modes show an increasing trend with eccentricity, with errors significantly smaller than those for amplitude. These results suggest that the PN fitting method captures frequency more accurately than amplitude. For eccentricities between 0 and 0.2, the errors remain below 4%, while for eccentricities from 0.2 to 0.4, they stay below 8%. The errors in SXS waveforms are lower than those in RIT waveforms.

The average phase absolute error, $|\delta \bar{\varphi}_{\ell m}|$, follows a pattern similar to that of the 22 mode, depending on both the waveform duration and the initial eccentricity. For clarity, we focus on the relationship between phase error and eccentricity. Across all waveform lengths, the phase error remains below 0.3 for eccentricities in the range of 0 to 0.2, demonstrating high precision for higher-order modes. For eccentricities between 0.2 and 0.4, the phase error stays below 1 for nonspinning waveforms and under 2 for spin-aligned waveforms, indicating a decline in phase accuracy at higher eccentricities.

In summary, the frequency and phase behaviors of the higher-order modes are similar to those of the 22 mode, showing comparable average errors. This consistency demonstrates that the parameters obtained from fitting the 22 mode are valid for higher-order modes. While the amplitudes of higher-order modes are best estimated by their leading-order moment, the errors tend to be larger than for the 22 mode. Additionally, the errors in higher-order modes for RIT waveforms generally exceed those in SXS waveforms, and spin-aligned scenarios exhibit larger errors compared to nonspinning cases.

E. Small mass ratio fitting problems and implications

In Sec. III A, we highlighted the issue of increasing fitting residuals with the mass ratio. This trend may arise from the growing error in NR simulations of eccentric orbit BBH systems as the mass ratio decreases. The RIT simulations include a lower mass ratio of 1/7, which we provides lengthy waveforms suitable for fitting but discards excessively short waveforms here. For this study, we focus exclusively on waveforms with a mass ratio of 1/4, as previously mentioned, and omit those with mass ratios of 1/5, 1/6, and 1/7. This section clarifies the rationale behind excluding these specific mass ratios.

FIG. 18 displays the frequencies of the 22 modes for the long waveforms RIT:eBBH:1514 (panel (a)) and RIT:eBBH:1560 (panel (c)), with mass ratios of 1/5 and 1/7 from the RIT catalog, along with their corresponding PN fitting outcomes. Panel (b) shows the frequency of waveform RIT:eBBH:1537 and the circular orbit waveform with an equivalent mass ratio $q = 1/6$, sourced from SEOBNRv4 of PyCBC. Panel (b) serves a similar purpose as FIG. 5.

Waveforms RIT:eBBH:1514, RIT:eBBH:1537, and RIT:eBBH:1560 share identical initial parameters with other long waveforms in the RIT catalog, specifically, no spin, an initial coordinate separation of 24M, and a similar initial eccentricity of approximately 0.19. The only difference is the mass ratio. According to PN and NR theories, under similar initial conditions, a smaller mass ratio should result in a longer merger time and thus a longer waveform. However, waveforms RIT:eBBH:1514 and RIT:eBBH:1537 exhibit shorter waveform durations compared to RIT:eBBH:1491, which has a larger mass ratio of $q = 1/4$. This discrepancy suggests potential issues with the NR simulations of RIT:eBBH:1514 and RIT:eBBH:1537.

In contrast to waveform RIT:eBBH:1282, panel (a) of FIG. 18 shows the PN fitting results for waveform RIT:eBBH:1514 over the interval $[-15552M, -10000M]$. Due to the infeasibility of fitting the entire waveform, only the initial segment was considered. While the fitting of this segment appears satisfactory, significant deviations are evident between the PN waveform and the NR waveform in subsequent segments, indicating possible issues with the NR simulation.

The discrepancy in the 22 mode frequency of waveform RIT:eBBH:1537, shown in panel (b) of FIG. 18, is notably more pronounced. Its significantly shorter waveform duration compared to that in panel (a) highlights this issue. Additionally, plotting a circular orbit waveform with the same mass ratio of $q = 1/6$ reveals a marked deviation from the average orbital frequency of the eccentric waveform. This deviation contradicts our expectations based on FIG. 5, where the circular orbit waveform frequency should approximately align with the midpoint of the eccentric waveform frequency deviation. This pronounced discrepancy strongly suggests problems

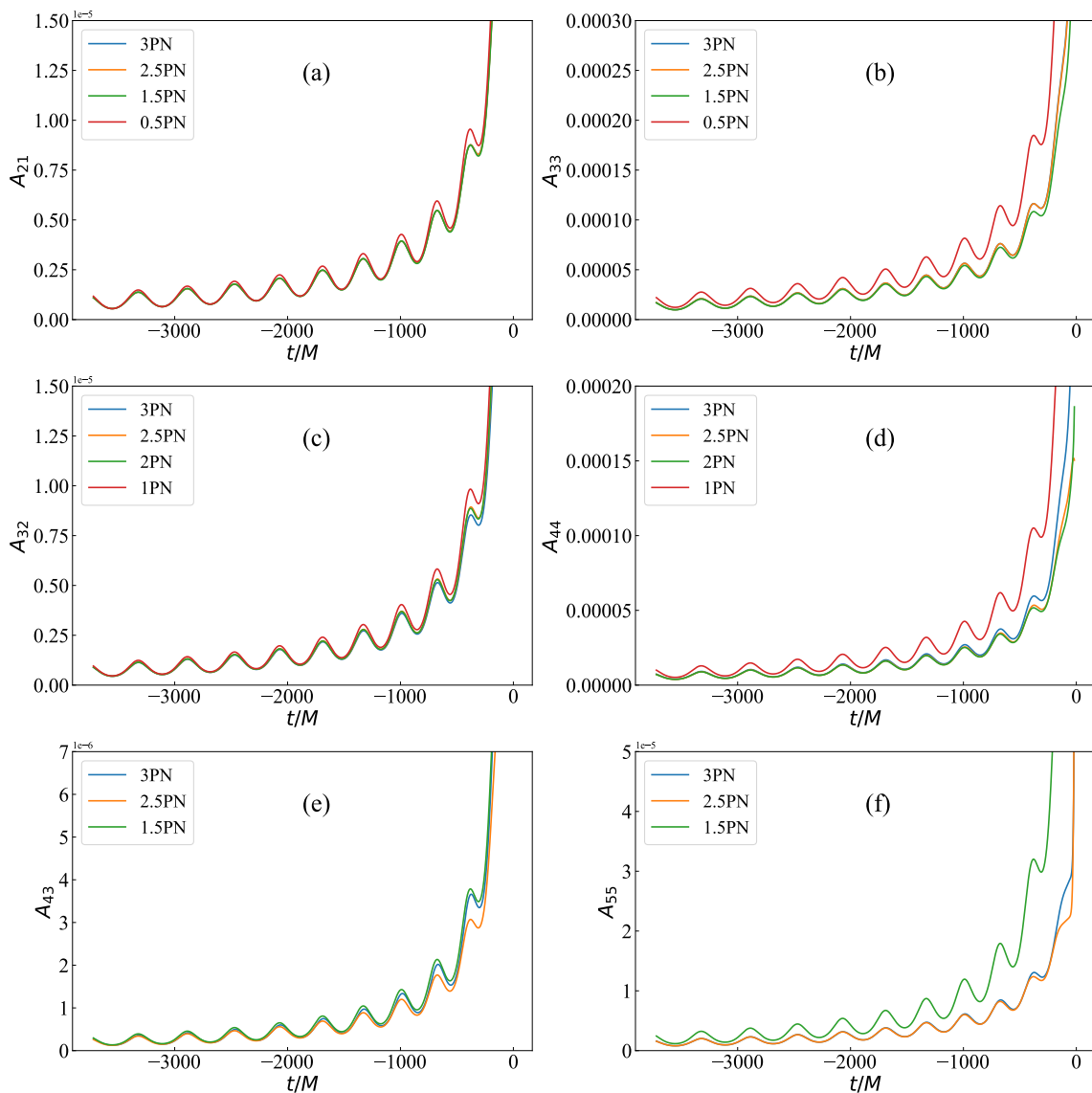


FIG. 14. Amplitudes of various PN order moments for the higher-order modes 21 (a), 33 (b), 32 (c), 44 (d), 43 (e), and 55 (f) of the waveform SXS:BBH:1364.

within the NR simulation of RIT:eBBH:1537.

Regarding waveform RIT:eBBH:1560, shown in panel (c) of FIG. 18, a complete waveform fit is possible. However, the fitting results reveal a discrepancy: the initial eccentricity inferred from radiation reaction differs from that derived via quasi-Keplerian parameterization. Partial fits lead to larger deviations, which are not shown here. This inconsistency causes a divergence between the PN fitting and the NR waveform, suggesting potential issues in the NR simulation of waveform RIT:eBBH:1560.

In conclusion, NR simulations of BBH in eccentric orbits, particularly for small mass ratios, may encounter challenges, resulting in inaccuracies in the waveforms. This underscores the need for careful selection of waveforms with smaller mass ratios when constructing templates and highlights the importance of exploring wave-

forms from diverse dynamical perspectives for cross-validation. The findings from NR simulations in small mass ratio cases emphasize the critical need for developing more accurate and refined NR algorithms to improve gravitational wave parameter extraction and reduce systematic errors.

IV. CONCLUSION AND OUTLOOK

In this study, we present a comprehensive comparison between post-Newtonian and numerically relativistic waveforms in eccentric orbits, encompassing both non-spinning and spin-aligned configurations. The comparison delves into the frequency, amplitude, and phase characteristics of various harmonic modes, including the 22,

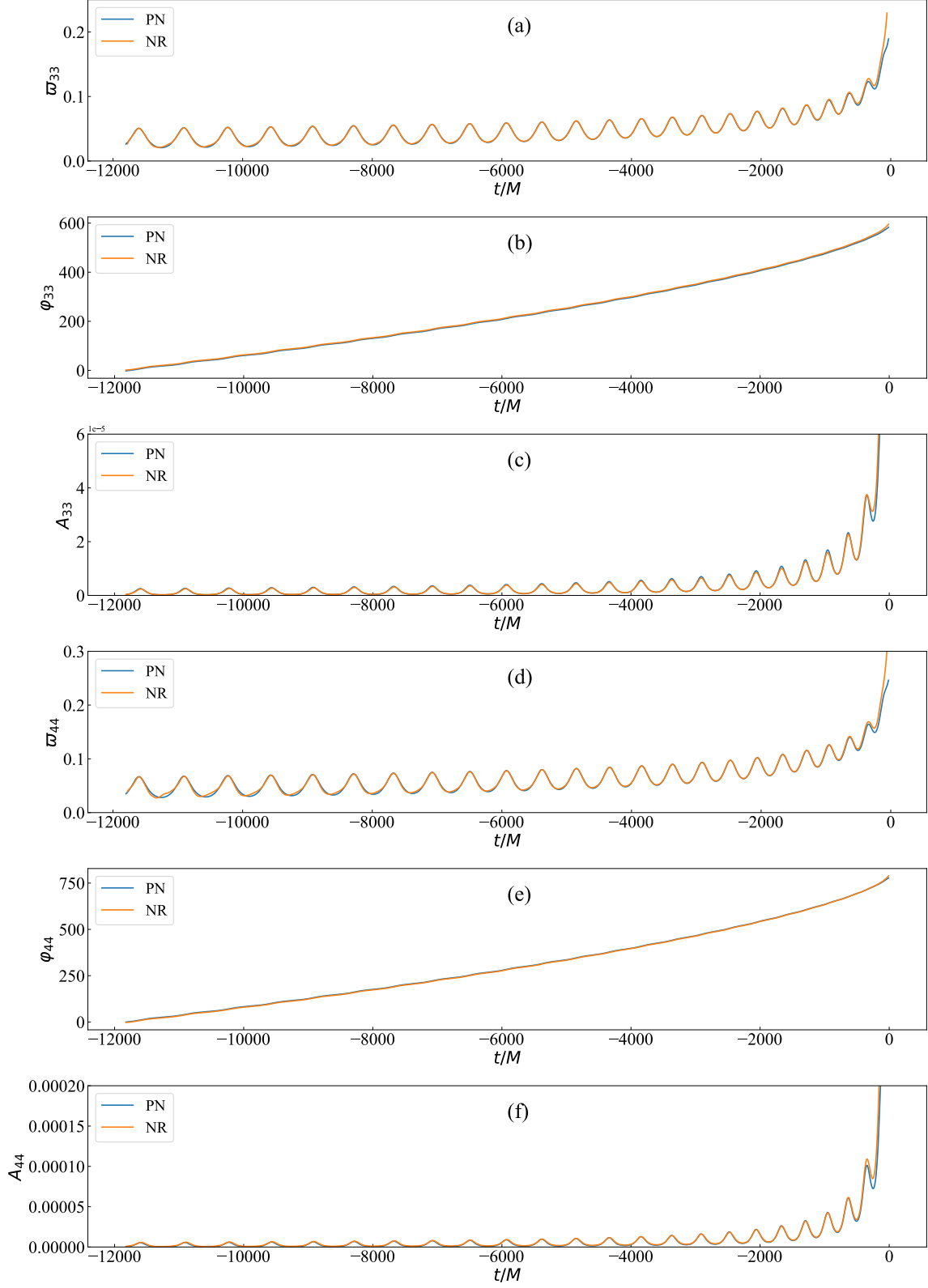


FIG. 15. PN fitting results of frequency ((a), (d)), phase ((b), (e)) and amplitude ((c), (f)) of the 33 and 44 modes of the long nonspinning waveform RIT:eBBH:1330.

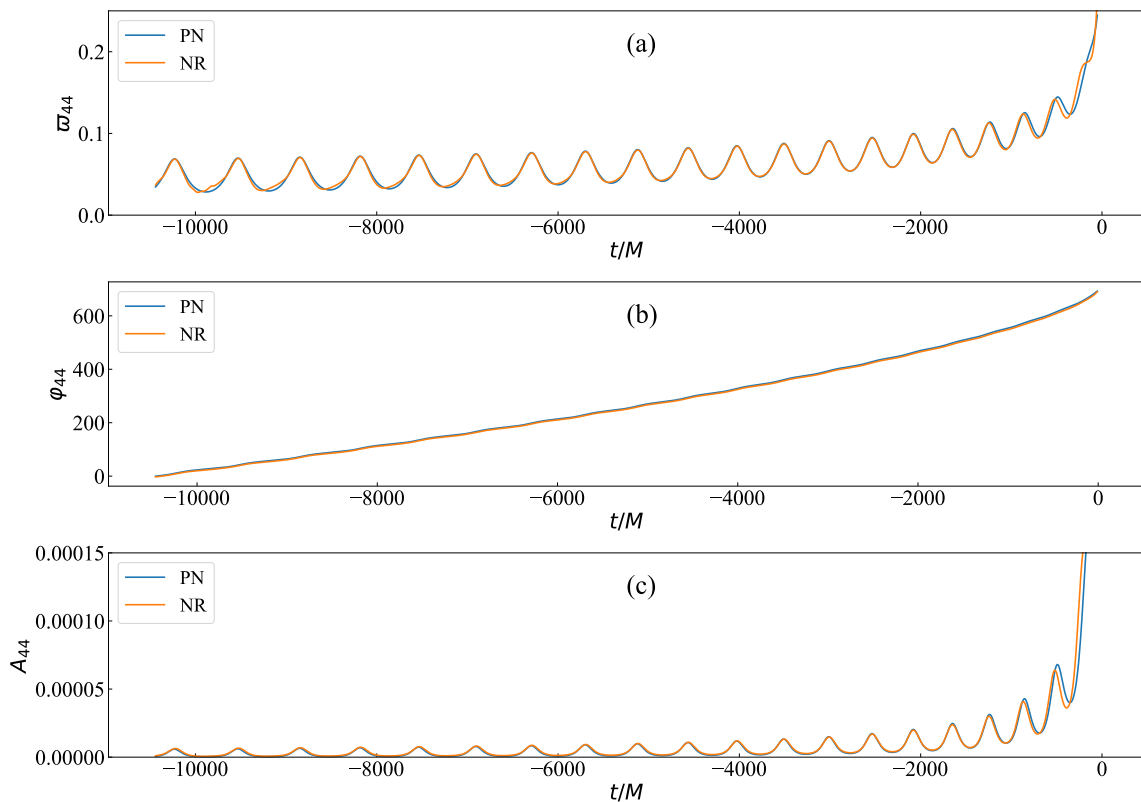


FIG. 16. PN fitting results of the frequency (a), phase (b), and amplitude (c) of the 44 modes of long spin-aligned waveform RIT:eBBH:1899.

21, 33, 32, 44, 43, and 55 modes. The nonspinning and spin-aligned eccentric PN waveforms utilized in our analysis are founded on the 3PN quasi-Keplerian parameterization, incorporating 3PN radiative reaction incorporating instantaneous and hereditary contributions. Furthermore, we utilize the gravitational wave amplitude from higher-order moments at 3PN, which exceed the Newtonian quadrupole moment. The NR waveforms considered in our study comprise a diverse array of eccentric orbit waveforms sourced from the RIT and SXS catalogs. These waveforms span mass ratios ranging from 1/4 to 1, eccentricities from 0 to 0.45, and waveform durations extending beyond $17000M$, across both nonspinning and spin-aligned configurations.

In our investigation, we opted to focus on the 22 mode as the target for fitting and proceeded to compare the frequencies of the quadrupole moments and higher-order moments of Ψ_4^{22} and h^{22} . To ensure a comprehensive analysis, we utilized the fitting parameters of the Ψ_4^{22} of higher-order moment as the reference standard. Throughout our analysis, we compared the amplitudes of the quadrupole and higher-order moments of Ψ_4^{22} and h^{22} . Notably, we found that the amplitude derived from the quadrupole moment of Ψ_4^{22} demonstrated superior accuracy, while the amplitudes associated with other PN order moments showed relatively diminished values in comparison.

Throughout our study, we conducted fitting exercises on a total of 180 sets of eccentricity waveforms, revealing a trend where fitting residuals increased in correspondence with rising eccentricity. Notably, these residuals proved to be independent of waveform length, catalog source, and spin but exhibited a correlation with the mass ratio. Specifically, we noted that smaller mass ratios correlated with larger fitting residuals, potentially indicating reduced accuracy in NR simulations involving small mass ratios.

Moreover, our analysis involved a comparison of the initial eccentricity obtained through PN fitting with that derived from the 3PN quasi-Keplerian parameterization and the initial eccentricity provided by the RIT and SXS catalogs. Notably, we observed that the initial eccentricity from RIT closely approximated e_{t_0} , followed by the quasi-Keplerian parameterization, while SXS exhibited the least alignment.

Further investigations delved into comparing the frequency, phase, and amplitude characteristics of the 22 modes. Noteworthy findings included a strong consistency between PN and NR in the inspiral segment, particularly evident in extended waveforms. Nevertheless, discrepancies became apparent as the nonspinning PN model started to diverge roughly at $200M$ before the merger, while the spin-aligned PN waveform exhibited failures before the $200M$. Furthermore, discrepancies be-

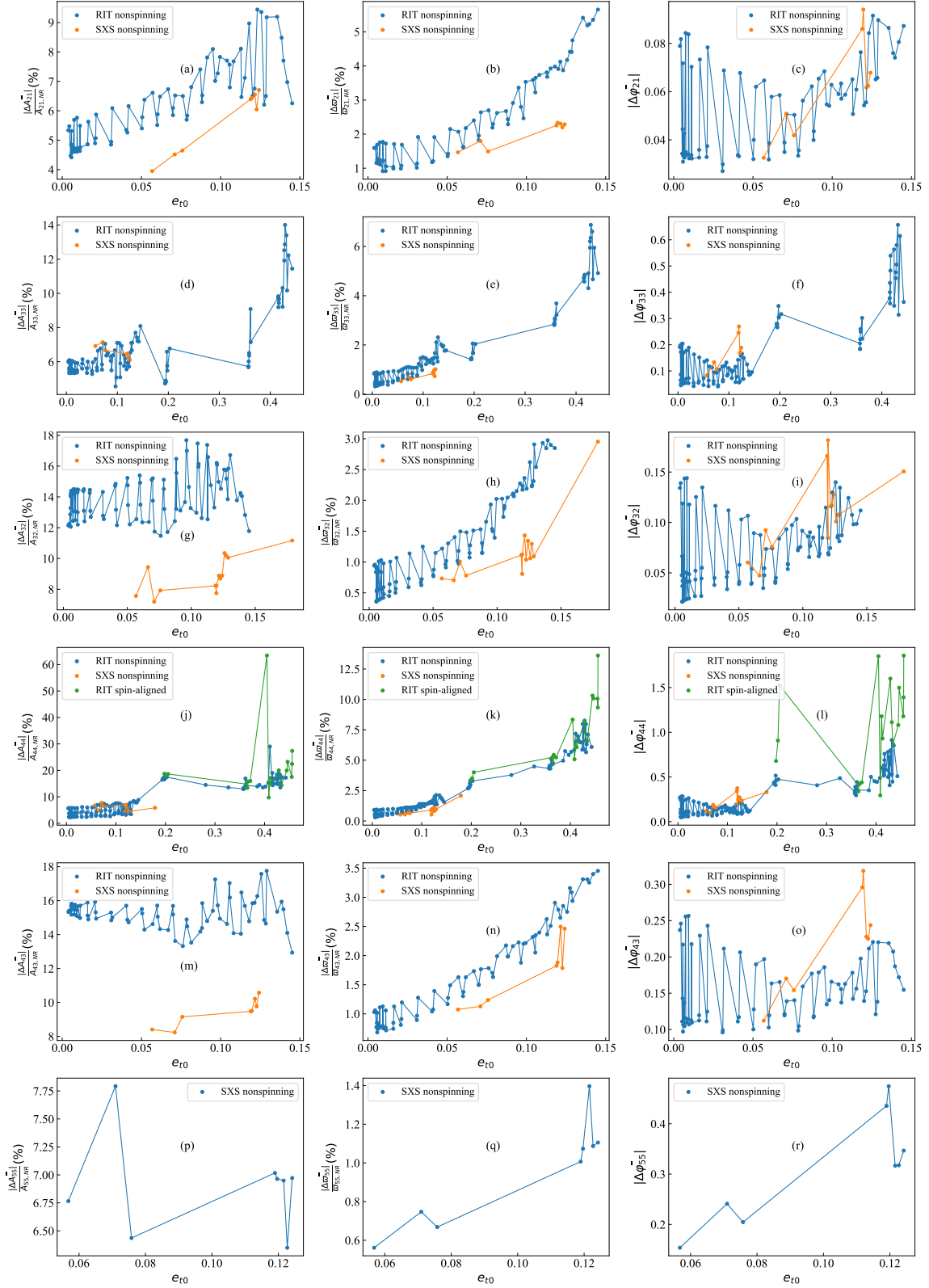


FIG. 17. Correlation between the average amplitude relative error $\frac{|\delta \bar{A}_{\ell m}|}{A_{\ell m, NR}}$ ((a), (d), (g), (j), (m), (p)), the average frequency relative error $\frac{|\delta \bar{\omega}_{\ell m}|}{\omega_{\ell m, NR}}$ ((b), (e), (h), (k), (n), (q)), and the average phase absolute error $|\delta \bar{\varphi}_{\ell m}|$ ((c), (f), (i), (l), (o), (r)) resulting from the PN fitting of the high-order mode and the initial eccentricity parameters e_{t0} .

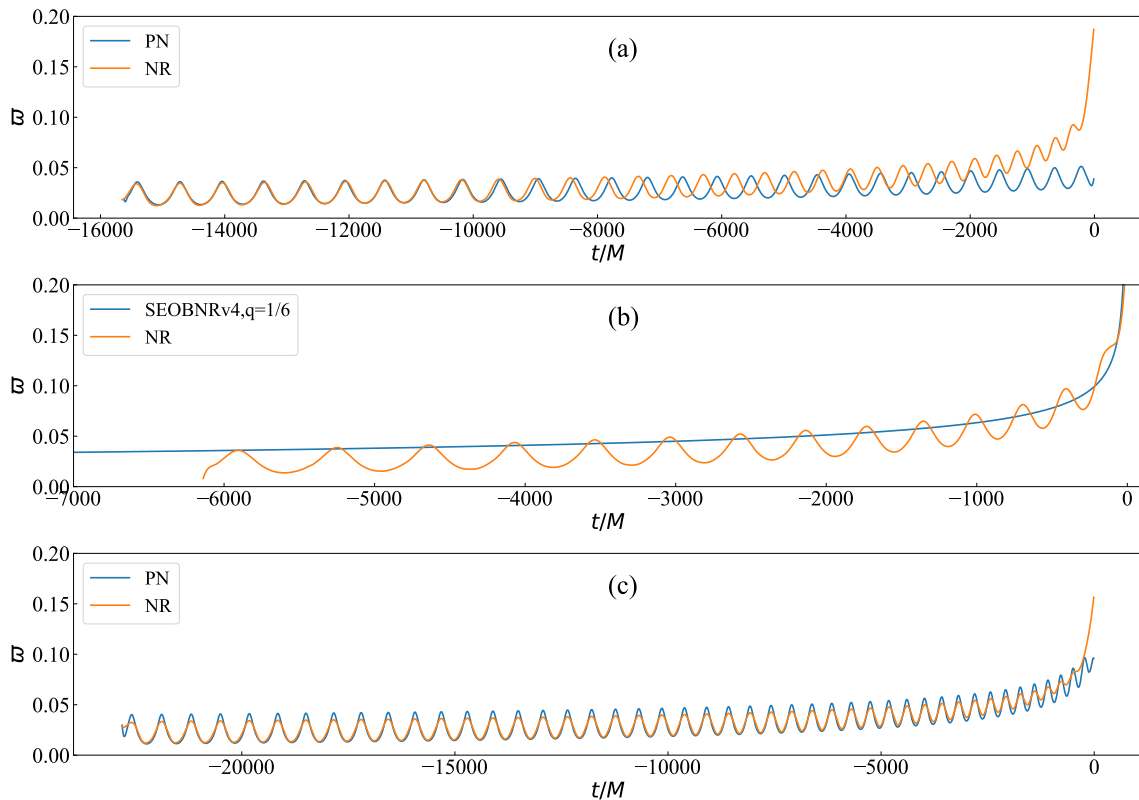


FIG. 18. Frequencies of the 22 modes for the longest waveforms RIT:eBBH:1514 (a) and RIT:eBBH:1560 (c) with mass ratios of $1/5$ and $1/7$ from the RIT catalog alongside their corresponding PN fitting outcomes. Panel (b) displays the frequencies of waveform RIT:eBBH:1537 and the circular orbit waveform with the equivalent mass ratio $q = 1/6$, sourced from SEOBNRv4 of Pycbc.

tween PN and NR waveforms magnified with increasing initial eccentricity, notably apparent at the periastron point and merger phase, where strong-field effects came into play.

Given the oscillatory nature of frequency, phase, and amplitude in eccentric waveforms, the discrepancies between PN and NR waveforms also oscillate, rendering it challenging to pinpoint a specific moment for error assessment. Consequently, in our study, we utilized the average errors $\frac{|\delta\omega|}{\omega_{NR}}$, $|\delta\varphi|$, and $\frac{|\delta A|}{A_{NR}}$ up to $200M$ pre-merger to encapsulate the overall waveform behavior. Our analysis revealed that the average errors in frequency, amplitude, and phase of the 22 modes amplified alongside increasing eccentricity levels. For eccentricities ranging from 0 to 0.2, we observed frequency errors below 3%, phase errors below 0.2, and amplitude errors under 6%. In cases where eccentricities spanned 0.2 to 0.4, nonspinning scenarios exhibited frequency errors between 2% and 6%, phase errors ranging from 0.1 to 0.3, and amplitude errors of 5% to 7.5%. Conversely, in spin-aligned cases within the same eccentricity range, frequency errors were between 2% and 8%, phase errors ranged from 0.3 to 0.5, and amplitude errors fell within 6% to 10%. As eccentricity surpassed 0.4, errors escalated. Furthermore, phase errors demonstrated an increase with elongating waveform

lengths.

Subsequently, we conducted a comparative analysis of the amplitudes, frequencies, and phases of the higher-order modes, including the 21, 33, 32, 44, 43, and 55 modes. Our observations indicated that the frequency and phase characteristics mirrored those of the 22 mode, whereas the amplitude behavior diverged. Notably, the leading-order moment's amplitude consistently provided the most precise results across these modes. Utilizing the average error metric, we quantified the disparities between the PN and NR waveforms for the higher-order modes. Our findings revealed that the frequency and amplitude errors exhibited similarities to those of the 22 mode, although the amplitude errors were comparatively larger. Each mode displayed distinct error patterns, highlighting the nuanced behaviors inherent to these higher-order modes.

In the last part, we performed fittings on three distinctive eccentric waveforms from RIT featuring lower mass ratios, uncovering varied challenges during the fitting procedures. We attribute these discrepancies to issues within NR simulations when dealing with low mass ratio scenarios, underscoring the imperative need for the advancement of a more precise NR simulation framework to address these specific challenges.

Through a comprehensive comparison of PN and NR

waveforms in eccentric orbits, we have delved deeply into the existing challenges within both methodologies. Our analysis underscores that there is still room for refinement in PN waveforms, particularly in enhancing accuracy across higher PN orders. Notably, for spin-aligned configurations, PN exhibits persistent shortcomings, experiencing failures preceding mergers and in proximity to periastron passages.

NR simulations, on the other hand, necessitate enhancements, particularly in handling small mass ratios and waveform extraction, with a specific focus on high-order mode extractions. To advance the construction of more precise gravitational wave templates for eccentric orbits, addressing these issues is paramount. By progressively resolving these challenges, we can systematically diminish systematic errors in parameter estimation, attain more precise gravitational wave parameters, and sig-

nificantly advance gravitational wave detection efforts.

ACKNOWLEDGMENTS

The authors are very grateful to RIT collaboration and SXS collaboration for the numerical simulation of eccentric BBH mergers, and thanks to Yan-Fang Huang, Zhou-Jian Cao, Duan-Yuan Gao, Lin Zhou, Yuan-Yuan Zuo, Jun-Yi Shen and Shi-Yan Tian for their helpful discussions. The computation is partially completed in the HPC Platform of Huazhong University of Science and Technology. The language was polished by ChatGPT during the revision of the draft. This work is supported by the National Key R&D Program of China (2021YFA0718504). Z. L. is supported by China Scholarship Council, No. 202306340128.

-
- [1] B. P. Abbott et al. (LIGO Scientific, Virgo), *Phys. Rev. Lett.* **116**, 061102 (2016), [arXiv:1602.03837 \[gr-qc\]](#).
 - [2] J. Aasi et al. (LIGO Scientific, VIRGO), *Class. Quant. Grav.* **32**, 115012 (2015), [arXiv:1410.7764 \[gr-qc\]](#).
 - [3] F. Acernese et al. (VIRGO), *Class. Quant. Grav.* **32**, 024001 (2015), [arXiv:1408.3978 \[gr-qc\]](#).
 - [4] T. Akutsu et al. (KAGRA), *Nature Astron.* **3**, 35 (2019), [arXiv:1811.08079 \[gr-qc\]](#).
 - [5] L. collaboration, Gravitational wave open science center, <https://www.gw-openscience.org/eventapi/html/GWTC/>.
 - [6] L. Blanchet, *Living Rev. Rel.* **17**, 2 (2014), [arXiv:1310.1528 \[gr-qc\]](#).
 - [7] A. Buonanno and T. Damour, *Phys. Rev. D* **59**, 084006 (1999), [arXiv:gr-qc/9811091](#).
 - [8] T. Damour, *Phys. Rev. D* **64**, 124013 (2001), [arXiv:gr-qc/0103018](#).
 - [9] S. A. Teukolsky, *Astrophys. J.* **185**, 635 (1973).
 - [10] F. Pretorius, *Phys. Rev. Lett.* **95**, 121101 (2005), [arXiv:gr-qc/0507014](#).
 - [11] M. Campanelli, C. O. Lousto, P. Marronetti, and Y. Zlochower, *Phys. Rev. Lett.* **96**, 111101 (2006), [arXiv:gr-qc/0511048](#).
 - [12] J. G. Baker, J. Centrella, D.-I. Choi, M. Koppitz, and J. van Meter, *Phys. Rev. Lett.* **96**, 111102 (2006), [arXiv:gr-qc/0511103](#).
 - [13] T. W. Baumgarte and S. L. Shapiro, *Phys. Rev. D* **59**, 024007 (1998), [arXiv:gr-qc/9810065](#).
 - [14] A. Gopakumar, M. Hannam, S. Husa, and B. Bruegmann, *Phys. Rev. D* **78**, 064026 (2008), [arXiv:0712.3737 \[gr-qc\]](#).
 - [15] S. Borhanian, K. G. Arun, H. P. Pfeiffer, and B. S. Sathyaprakash, *Class. Quant. Grav.* **37**, 065006 (2020), [arXiv:1901.08516 \[gr-qc\]](#).
 - [16] M. Boyle, D. A. Brown, L. E. Kidder, A. H. Mroue, H. P. Pfeiffer, M. A. Scheel, G. B. Cook, and S. A. Teukolsky, *Phys. Rev. D* **76**, 124038 (2007), [arXiv:0710.0158 \[gr-qc\]](#).
 - [17] M. Boyle, D. A. Brown, and L. Pekowsky, *Class. Quant. Grav.* **26**, 114006 (2009), [arXiv:0901.1628 \[gr-qc\]](#).
 - [18] Y. Pan, A. Buonanno, J. G. Baker, J. Centrella, B. J. Kelly, S. T. McWilliams, F. Pretorius, and J. R. van Meter, *Phys. Rev. D* **77**, 024014 (2008), [arXiv:0704.1964 \[gr-qc\]](#).
 - [19] M. Hannam, S. Husa, B. Bruegmann, and A. Gopakumar, *Phys. Rev. D* **78**, 104007 (2008), [arXiv:0712.3787 \[gr-qc\]](#).
 - [20] M. Hannam, S. Husa, F. Ohme, D. Muller, and B. Bruegmann, *Phys. Rev. D* **82**, 124008 (2010), [arXiv:1007.4789 \[gr-qc\]](#).
 - [21] M. Campanelli, C. O. Lousto, H. Nakano, and Y. Zlochower, *Phys. Rev. D* **79**, 084010 (2009), [arXiv:0808.0713 \[gr-qc\]](#).
 - [22] S. Habib and E. A. Huerta, *Phys. Rev. D* **100**, 044016 (2019), [arXiv:1904.09295 \[gr-qc\]](#).
 - [23] A. Chattaraj, T. RoyChowdhury, Divyajyoti, C. K. Mishra, and A. Gupta, *Phys. Rev. D* **106**, 124008 (2022), [arXiv:2204.02377 \[gr-qc\]](#).
 - [24] I. Hinder, F. Herrmann, P. Laguna, and D. Shoemaker, *Phys. Rev. D* **82**, 024033 (2010), [arXiv:0806.1037 \[gr-qc\]](#).
 - [25] P. C. Peters and J. Mathews, *Phys. Rev.* **131**, 435 (1963).
 - [26] P. C. Peters, *Phys. Rev.* **136**, B1224 (1964).
 - [27] I. Hinder, B. Vaishnav, F. Herrmann, D. Shoemaker, and P. Laguna, *Phys. Rev. D* **77**, 081502 (2008), [arXiv:0710.5167 \[gr-qc\]](#).
 - [28] R. O'Leary, R. W. O'Shaughnessy, and F. Rasio, *Phys. Rev. D* **76**, 061504 (2007), [arXiv:astro-ph/0701887](#).
 - [29] M. C. Miller and D. P. Hamilton, *Astrophys. J.* **576**, 894 (2002), [arXiv:astro-ph/0202298](#).
 - [30] K. Gultekin, M. Coleman Miller, and D. P. Hamilton, *Astrophys. J.* **640**, 156 (2006), [arXiv:astro-ph/0509885](#).
 - [31] R. M. O'Leary, F. A. Rasio, J. M. Fregeau, N. Ivanova, and R. W. O'Shaughnessy, *Astrophys. J.* **637**, 937 (2006), [arXiv:astro-ph/0508224](#).
 - [32] C. L. Rodriguez, M. Morscher, B. Pattabiraman, S. Chatterjee, C.-J. Haster, and F. A. Rasio, *Phys. Rev. Lett.* **115**, 051101 (2015), [Erratum: *Phys. Rev. Lett.* **116**, 029901 (2016)], [arXiv:1505.00792 \[astro-ph.HE\]](#).
 - [33] J. Samsing, *Phys. Rev. D* **97**, 103014 (2018), [arXiv:1711.07452 \[astro-ph.HE\]](#).

- [34] C. L. Rodriguez, P. Amaro-Seoane, S. Chatterjee, and F. A. Rasio, *Phys. Rev. Lett.* **120**, 151101 (2018), [arXiv:1712.04937 \[astro-ph.HE\]](#).
- [35] C. L. Rodriguez, P. Amaro-Seoane, S. Chatterjee, K. Kremer, F. A. Rasio, J. Samsing, C. S. Ye, and M. Zevin, *Phys. Rev. D* **98**, 123005 (2018), [arXiv:1811.04926 \[astro-ph.HE\]](#).
- [36] D. Park, C. Kim, H. M. Lee, Y.-B. Bae, and K. Belczynski, *Mon. Not. Roy. Astron. Soc.* **469**, 4665 (2017), [arXiv:1703.01568 \[astro-ph.HE\]](#).
- [37] L. Gondán and B. Kocsis, *Mon. Not. Roy. Astron. Soc.* **506**, 1665 (2021), [arXiv:2011.02507 \[astro-ph.HE\]](#).
- [38] F. Antonini and H. B. Perets, *Astrophys. J.* **757**, 27 (2012), [arXiv:1203.2938 \[astro-ph.GA\]](#).
- [39] B. Kocsis and J. Levin, *Phys. Rev. D* **85**, 123005 (2012), [arXiv:1109.4170 \[astro-ph.CO\]](#).
- [40] B.-M. Hoang, S. Naoz, B. Kocsis, F. A. Rasio, and F. Dosopoulou, *Astrophys. J.* **856**, 140 (2018), [arXiv:1706.09896 \[astro-ph.HE\]](#).
- [41] L. Gondán, B. Kocsis, P. Raffai, and Z. Frei, *Astrophys. J.* **860**, 5 (2018), [arXiv:1711.09989 \[astro-ph.HE\]](#).
- [42] J. Samsing, I. Bartos, D. J. D’Orazio, Z. Haiman, B. Kocsis, N. W. C. Leigh, B. Liu, M. E. Pessah, and H. Tagawa, *Nature* **603**, 237 (2022), [arXiv:2010.09765 \[astro-ph.HE\]](#).
- [43] H. Tagawa, B. Kocsis, Z. Haiman, I. Bartos, K. Omukai, and J. Samsing, *Astrophys. J. Lett.* **907**, L20 (2021), [arXiv:2010.10526 \[astro-ph.HE\]](#).
- [44] J. Samsing, M. MacLeod, and E. Ramirez-Ruiz, *Astrophys. J.* **784**, 71 (2014), [arXiv:1308.2964 \[astro-ph.HE\]](#).
- [45] J. Samsing, A. Askar, and M. Giersz, *Astrophys. J.* **855**, 124 (2018), [arXiv:1712.06186 \[astro-ph.HE\]](#).
- [46] M. Zevin, J. Samsing, C. Rodriguez, C.-J. Haster, and E. Ramirez-Ruiz, *Astrophys. J.* **871**, 91 (2019), [arXiv:1810.00901 \[astro-ph.HE\]](#).
- [47] M. Arca-Sedda, G. Li, and B. Kocsis, *Astron. Astrophys.* **650**, A189 (2021), [arXiv:1805.06458 \[astro-ph.HE\]](#).
- [48] W. E. East, S. T. McWilliams, J. Levin, and F. Pretorius, *Phys. Rev. D* **87**, 043004 (2013), [arXiv:1212.0837 \[gr-qc\]](#).
- [49] S. Naoz, B. Kocsis, A. Loeb, and N. Yunes, *Astrophys. J.* **773**, 187 (2013), [arXiv:1206.4316 \[astro-ph.SR\]](#).
- [50] J. H. VanLandingham, M. C. Miller, D. P. Hamilton, and D. C. Richardson, *Astrophys. J.* **828**, 77 (2016), [arXiv:1604.04948 \[astro-ph.HE\]](#).
- [51] K. Silsbee and S. Tremaine, *Astrophys. J.* **836**, 39 (2017), [arXiv:1608.07642 \[astro-ph.HE\]](#).
- [52] O. Blaes, M. H. Lee, and A. Socrates, *Astrophys. J.* **578**, 775 (2002), [arXiv:astro-ph/0203370](#).
- [53] J. M. Antognini, B. J. Shappee, T. A. Thompson, and P. Amaro-Seoane, *Mon. Not. Roy. Astron. Soc.* **439**, 1079 (2014), [arXiv:1308.5682 \[astro-ph.HE\]](#).
- [54] A. P. Stephan, S. Naoz, A. M. Ghez, G. Witzel, B. N. Sitariski, T. Do, and B. Kocsis, *Mon. Not. Roy. Astron. Soc.* **460**, 3494 (2016), [arXiv:1603.02709 \[astro-ph.SR\]](#).
- [55] B. Katz, S. Dong, and R. Malhotra, *Phys. Rev. Lett.* **107**, 181101 (2011), [arXiv:1106.3340 \[astro-ph.EP\]](#).
- [56] N. Seto, *Phys. Rev. Lett.* **111**, 061106 (2013), [arXiv:1304.5151 \[astro-ph.CO\]](#).
- [57] R. Abbott *et al.* (LIGO Scientific, Virgo), *Phys. Rev. Lett.* **125**, 101102 (2020), [arXiv:2009.01075 \[gr-qc\]](#).
- [58] V. Gayathri, J. Healy, J. Lange, B. O’Brien, M. Szczepanczyk, I. Bartos, M. Campanelli, S. Klimentko, C. O. Lousto, and R. O’Shaughnessy, *Nature Astron.* **6**, 344 (2022), [arXiv:2009.05461 \[astro-ph.HE\]](#).
- [59] I. M. Romero-Shaw, P. D. Lasky, E. Thrane, and J. C. Bustillo, *Astrophys. J. Lett.* **903**, L5 (2020), [arXiv:2009.04771 \[astro-ph.HE\]](#).
- [60] M. Punturo *et al.*, *Class. Quant. Grav.* **27**, 194002 (2010).
- [61] D. Reitze *et al.*, *Bull. Am. Astron. Soc.* **51**, 035 (2019), [arXiv:1907.04833 \[astro-ph.IM\]](#).
- [62] A. H. Mroue *et al.*, *Phys. Rev. Lett.* **111**, 241104 (2013), [arXiv:1304.6077 \[gr-qc\]](#).
- [63] M. Boyle *et al.*, *Class. Quant. Grav.* **36**, 195006 (2019), [arXiv:1904.04831 \[gr-qc\]](#).
- [64] J. Healy, C. O. Lousto, Y. Zlochower, and M. Campanelli, *Class. Quant. Grav.* **34**, 224001 (2017), [arXiv:1703.03423 \[gr-qc\]](#).
- [65] J. Healy, C. O. Lousto, J. Lange, R. O’Shaughnessy, Y. Zlochower, and M. Campanelli, *Phys. Rev. D* **100**, 024021 (2019), [arXiv:1901.02553 \[gr-qc\]](#).
- [66] J. Healy and C. O. Lousto, *Phys. Rev. D* **102**, 104018 (2020), [arXiv:2007.07910 \[gr-qc\]](#).
- [67] J. Healy and C. O. Lousto, *Phys. Rev. D* **105**, 124010 (2022), [arXiv:2202.00018 \[gr-qc\]](#).
- [68] E. Hamilton *et al.*, *Phys. Rev. D* **109**, 044032 (2024), [arXiv:2303.05419 \[gr-qc\]](#).
- [69] B. Bruegmann, J. A. Gonzalez, M. Hannam, S. Husa, U. Sperhake, and W. Tichy, *Phys. Rev. D* **77**, 024027 (2008), [arXiv:gr-qc/0610128](#).
- [70] S. Husa, J. A. Gonzalez, M. Hannam, B. Bruegmann, and U. Sperhake, *Class. Quant. Grav.* **25**, 105006 (2008), [arXiv:0706.0740 \[gr-qc\]](#).
- [71] K. Jani, J. Healy, J. A. Clark, L. London, P. Laguna, and D. Shoemaker, *Class. Quant. Grav.* **33**, 204001 (2016), [arXiv:1605.03204 \[gr-qc\]](#).
- [72] D. Ferguson *et al.*, (2023), [arXiv:2309.00262 \[gr-qc\]](#).
- [73] Caltech-Cornell-CITA, binary black hole simulation results, <http://www.black-holes.org/waveforms> ().
- [74] Caltech-Cornell-CITA, Rit binary black hole simulation results, <https://ccrg.rit.edu/numerical-simulations> ().
- [75] R.-M. Memmesheimer, A. Gopakumar, and G. Schafer, *Phys. Rev. D* **70**, 104011 (2004), [arXiv:gr-qc/0407049](#).
- [76] G. Cho, S. Tanay, A. Gopakumar, and H. M. Lee, *Phys. Rev. D* **105**, 064010 (2022), [arXiv:2110.09608 \[gr-qc\]](#).
- [77] M. Tessmer, J. Hartung, and G. Schafer, *Class. Quant. Grav.* **27**, 165005 (2010), [arXiv:1003.2735 \[gr-qc\]](#).
- [78] M. Tessmer, J. Hartung, and G. Schafer, *Class. Quant. Grav.* **30**, 015007 (2013), [arXiv:1207.6961 \[gr-qc\]](#).
- [79] C. Konigsdorffer and A. Gopakumar, *Phys. Rev. D* **73**, 124012 (2006), [arXiv:gr-qc/0603056](#).
- [80] A. Gopakumar and B. R. Iyer, *Phys. Rev. D* **65**, 084011 (2002), [arXiv:gr-qc/0110100](#).
- [81] K. G. Arun, L. Blanchet, B. R. Iyer, and S. Sinha, *Phys. Rev. D* **80**, 124018 (2009), [arXiv:0908.3854 \[gr-qc\]](#).
- [82] K. G. Arun, L. Blanchet, B. R. Iyer, and M. S. S. Quisailah, *Phys. Rev. D* **77**, 064034 (2008), [arXiv:0711.0250 \[gr-qc\]](#).
- [83] K. G. Arun, L. Blanchet, B. R. Iyer, and M. S. S. Quisailah, *Phys. Rev. D* **77**, 064035 (2008), [arXiv:0711.0302 \[gr-qc\]](#).
- [84] B. Moore, M. Favata, K. G. Arun, and C. K. Mishra, *Phys. Rev. D* **93**, 124061 (2016), [arXiv:1605.00304 \[gr-qc\]](#).
- [85] C. K. Mishra, K. G. Arun, and B. R. Iyer, *Phys. Rev.*

- D **91**, 084040 (2015), arXiv:1501.07096 [gr-qc].
- [86] Y. Boetzel, C. K. Mishra, G. Faye, A. Gopakumar, and B. R. Iyer, *Phys. Rev. D* **100**, 044018 (2019), arXiv:1904.11814 [gr-qc].
- [87] M. Ebersold, Y. Boetzel, G. Faye, C. K. Mishra, B. R. Iyer, and P. Jetzer, *Phys. Rev. D* **100**, 084043 (2019), arXiv:1906.06263 [gr-qc].
- [88] A. Klein and P. Jetzer, *Phys. Rev. D* **81**, 124001 (2010), arXiv:1005.2046 [gr-qc].
- [89] Q. Henry and M. Khalil, *Phys. Rev. D* **108**, 104016 (2023), arXiv:2308.13606 [gr-qc].
- [90] E. A. Huerta et al., *Phys. Rev. D* **95**, 024038 (2017), arXiv:1609.05933 [gr-qc].
- [91] I. Hinder, L. E. Kidder, and H. P. Pfeiffer, *Phys. Rev. D* **98**, 044015 (2018), arXiv:1709.02007 [gr-qc].
- [92] E. A. Huerta et al., *Phys. Rev. D* **97**, 024031 (2018), arXiv:1711.06276 [gr-qc].
- [93] T. D. Newton and E. P. Wigner, *Rev. Mod. Phys.* **21**, 400 (1949).
- [94] Y. Zlochower, J. G. Baker, M. Campanelli, and C. O. Lousto, *Phys. Rev. D* **72**, 024021 (2005), arXiv:gr-qc/0505055.
- [95] T. Nakamura, K. Oohara, and Y. Kojima, *Prog. Theor. Phys. Suppl.* **90**, 1 (1987).
- [96] M. Shibata and T. Nakamura, *Phys. Rev. D* **52**, 5428 (1995).
- [97] E. Schnetter, S. H. Hawley, and I. Hawke, *Class. Quant. Grav.* **21**, 1465 (2004), arXiv:gr-qc/0310042.
- [98] Y. Zlochower, M. Ponce, and C. O. Lousto, *Phys. Rev. D* **86**, 104056 (2012), arXiv:1208.5494 [gr-qc].
- [99] F. Löffler et al., *Class. Quant. Grav.* **29**, 115001 (2012), arXiv:1111.3344 [gr-qc].
- [100] L. Lindblom, M. A. Scheel, L. E. Kidder, R. Owen, and O. Rinne, *Class. Quant. Grav.* **23**, S447 (2006), arXiv:gr-qc/0512093.
- [101] B. Szilágyi, L. Lindblom, and M. A. Scheel, *Phys. Rev. D* **80**, 124010 (2009), arXiv:0909.3557 [gr-qc].
- [102] L. E. Kidder and L. S. Finn, *Phys. Rev. D* **62**, 084026 (2000), arXiv:gr-qc/9911014.
- [103] M. A. Scheel, M. Boyle, T. Chu, L. E. Kidder, K. D. Matthews, and H. P. Pfeiffer, *Phys. Rev. D* **79**, 024003 (2009), arXiv:0810.1767 [gr-qc].
- [104] D. A. Hemberger, M. A. Scheel, L. E. Kidder, B. Szilágyi, G. Lovelace, N. W. Taylor, and S. A. Teukolsky, *Class. Quant. Grav.* **30**, 115001 (2013), arXiv:1211.6079 [gr-qc].
- [105] F. Pretorius, *Class. Quant. Grav.* **22**, 425 (2005), arXiv:gr-qc/0407110.
- [106] D. O. Samary and F. Vignes-Tourneret, *Commun. Math. Phys.* **329**, 545 (2014), arXiv:1211.2618 [hep-th].
- [107] D. Garfinkle, *Phys. Rev. D* **65**, 044029 (2002), arXiv:gr-qc/0110013.
- [108] C. M. Biwer, C. D. Capano, S. De, M. Cabero, D. A. Brown, A. H. Nitz, and V. Raymond, *Publ. Astron. Soc. Pac.* **131**, 024503 (2019), arXiv:1807.10312 [astro-ph.IM].
- [109] A. H. Mroue, H. P. Pfeiffer, L. E. Kidder, and S. A. Teukolsky, *Phys. Rev. D* **82**, 124016 (2010), arXiv:1004.4697 [gr-qc].
- [110] Y. Setyawati and F. Ohme, *Phys. Rev. D* **103**, 124011 (2021), arXiv:2101.11033 [gr-qc].
- [111] H. Wang, Y.-C. Zou, and Y. Liu, *Phys. Rev. D* **107**, 124061 (2023), arXiv:2302.11227 [gr-qc].
- [112] J. Healy, C. O. Lousto, H. Nakano, and Y. Zlochower, *Class. Quant. Grav.* **34**, 145011 (2017), [Erratum: *Class. Quant. Grav.* **40**, 249502 (2023)], arXiv:1702.00872 [gr-qc].
- [113] B. Ireland, O. Birnholtz, H. Nakano, E. West, and M. Campanelli, *Phys. Rev. D* **100**, 024015 (2019), arXiv:1904.03443 [gr-qc].
- [114] A. Ramos-Buades, S. Husa, and G. Pratten, *Phys. Rev. D* **99**, 023003 (2019), arXiv:1810.00036 [gr-qc].
- [115] H. Wang, Y.-C. Zou, Q.-W. Wu, Y. Liu, and X. Liu, *Phys. Rev. D* **109**, 084063 (2024), arXiv:2310.04777 [gr-qc].
- [116] M. Radia, U. Sperhake, E. Berti, and R. Croft, *Phys. Rev. D* **103**, 104006 (2021), arXiv:2101.11015 [gr-qc].

Appendix A: eccentric PN expression

1. Nonspinning waveforms

In this section, we present the comprehensive formulation of the nonspinning BBH 3PN conservative dynamics. This description encompasses the computation of variables such as r , \dot{r} , ϕ , $\dot{\phi}$, l , and n . To streamline the presentation, we provide expressions for r and $\dot{\phi}$ herein, with \dot{r} and ϕ derivable through differentiation and integration. Regarding the nonspinning component, we direct the reader to Ref. [24], where these quantities are articulated in terms of the expansion parameter x and temporal eccentricity e_t .

The orbital radius r^{NS} of the nonspinning eccentric BBH can be expressed as

$$r^{\text{NS}} = r_{\text{Newt}}^{\text{NS}} x^{-1} + r_{1\text{PN}}^{\text{NS}} + r_{2\text{PN}}^{\text{NS}} x + r_{3\text{PN}}^{\text{NS}} x^2 + \mathcal{O}(x^3), \quad (\text{A1})$$

where the coefficients can be expressed as

$$r_{\text{Newt}}^{\text{NS}} = 1 - e_t \cos(u), \quad (\text{A2})$$

$$r_{1\text{PN}}^{\text{NS}} = \frac{2(e_t \cos(u) - 1)}{e_t^2 - 1} + \frac{1}{6}(2(\eta - 9) + e_t(7\eta - 6) \cos(u)), \quad (\text{A3})$$

$$\begin{aligned}
r_{2\text{PN}}^{\text{NS}} = & \frac{1}{(1-e_t^2)^2} \left[\frac{1}{72} (8\eta^2 + 30\eta + 72) e_t^4 + \frac{1}{72} (-16\eta^2 - 876\eta + 756) e_t^2 + \frac{1}{72} (8\eta^2 + 198\eta + 360) \right. \\
& + \left(\frac{1}{72} (-35\eta^2 + 231\eta - 72) e_t^5 + \frac{1}{72} (70\eta^2 - 150\eta - 468) e_t^3 + \frac{1}{72} (-35\eta^2 + 567\eta - 648) e_t \right) \cos(u) \\
& \left. + \sqrt{1-e_t^2} \left(\frac{1}{72} (360 - 144\eta) e_t^2 + \frac{1}{72} (144\eta - 360) + \left(\frac{1}{72} (180 - 72\eta) e_t^3 + \frac{1}{72} (72\eta - 180) e_t \right) \cos(u) \right) \right], \tag{A4}
\end{aligned}$$

$$\begin{aligned}
r_{3\text{PN}}^{\text{NS}} = & \frac{1}{181440 (1-e_t^2)^{7/2}} \left[(-665280\eta^2 + 1753920\eta - 1814400) e_t^6 \right. \\
& + (725760\eta^2 - 77490\pi^2\eta + 5523840\eta - 3628800) e_t^4 + (544320\eta^2 + 154980\pi^2\eta - 14132160\eta + 7257600) e_t^2 \\
& - 604800\eta^2 + 6854400\eta + ((302400\eta^2 - 1254960\eta + 453600) e_t^7 + (-1542240\eta^2 - 38745\pi^2\eta \\
& + 6980400\eta - 453600) e_t^5 + (2177280\eta^2 + 77490\pi^2\eta - 12373200\eta + 4989600) e_t^3 \\
& + (-937440\eta^2 - 38745\pi^2\eta + 6647760\eta - 4989600) e_t) \cos(u) \\
& + \sqrt{1-e_t^2} \left((-4480\eta^3 - 25200\eta^2 + 22680\eta - 120960) e_t^6 + (13440\eta^3 + 4404960\eta^2 + 116235\pi^2\eta \right. \\
& - 12718296\eta + 5261760) e_t^4 + (-13440\eta^3 + 2242800\eta^2 + 348705\pi^2\eta - 19225080\eta + 16148160) e_t^2 \\
& + 4480\eta^3 + 45360\eta^2 - 8600904\eta + ((-6860\eta^3 + 550620\eta^2 - 986580\eta + 120960) e_t^7 \\
& + (20580\eta^3 - 2458260\eta^2 + 3458700\eta - 2358720) e_t^5 + (-20580\eta^3 - 3539340\eta^2 - 116235\pi^2\eta \\
& + 20173860\eta - 16148160) e_t^3 + (6860\eta^3 - 1220940\eta^2 - 464940\pi^2\eta + 17875620\eta - 4717440) e_t) \cos(u) \\
& \left. + 116235\eta\pi^2 + 1814400 - 77490\eta\pi^2 - 1814400 \right]. \tag{A5}
\end{aligned}$$

The relative angular velocity $\dot{\phi}^{\text{NS}}$ of the nonspinning eccentric BBH can be expressed as

$$\dot{\phi}^{\text{NS}} = \dot{\phi}_{\text{Newt}}^{\text{NS}} x^{3/2} + \dot{\phi}_{1\text{PN}}^{\text{NS}} x^{5/2} + \dot{\phi}_{2\text{PN}}^{\text{NS}} x^{7/2} + \dot{\phi}_{3\text{PN}}^{\text{NS}} x^{9/2} + \mathcal{O}(x^{11/2}), \tag{A6}$$

where the coefficients can be expressed as

$$\dot{\phi}_{\text{Newt}}^{\text{NS}} = \frac{\sqrt{1-e_t^2}}{(e_t \cos(u) - 1)^2}, \tag{A7}$$

$$\dot{\phi}_{1\text{PN}}^{\text{NS}} = -\frac{e_t(\eta - 4)(e_t - \cos(u))}{\sqrt{1-e_t^2}(e_t \cos(u) - 1)^3}, \tag{A8}$$

$$\begin{aligned}
\dot{\phi}_{2\text{PN}}^{\text{NS}} = & \frac{1}{12(1-e_t^2)^{3/2}(e_t \cos(u) - 1)^5} \left[(-12\eta^2 - 18\eta) e_t^6 + (20\eta^2 - 26\eta - 60) e_t^4 + (-2\eta^2 + 50\eta + 75) e_t^2 \right. \\
& + [(-14\eta^2 + 8\eta - 147) e_t^5 + (8\eta^2 + 22\eta + 42) e_t^3] \cos^3(u) + [(17\eta^2 - 17\eta + 48) e_t^6 + (-4\eta^2 - 38\eta \\
& + 153) e_t^4 + (5\eta^2 - 35\eta + 114) e_t^2] \cos^2(u) - 36\eta + [(-\eta^2 + 97\eta + 12) e_t^5 + (-16\eta^2 - 74\eta - 81) e_t^3 \\
& + (-\eta^2 + 67\eta - 246) e_t] \cos(u) + \sqrt{1-e_t^2} [e_t^3(36\eta - 90) \cos^3(u) + ((180 - 72\eta) e_t^4 \\
& + (90 - 36\eta) e_t^2) \cos^2(u) + ((144\eta - 360) e_t^3 + (90 - 36\eta) e_t) \cos(u) + e_t^2(180 - 72\eta) + 36\eta - 90] + 90 \Big], \tag{A9}
\end{aligned}$$

$$\begin{aligned}
\dot{\phi}_{\text{3PN}}^{\text{NS}} = & \frac{1}{13440(1-e_t^2)^{5/2}(e_t \cos(u)-1)^7} \left[(10080\eta^3 + 40320\eta^2 - 15120\eta) e_t^{10} + (-52640\eta^3 - 13440\eta^2 + 483280\eta) e_t^8 \right. \\
& + (84000\eta^3 - 190400\eta^2 - 17220\pi^2\eta - 50048\eta - 241920) e_t^6 + (-52640\eta^3 + 516880\eta^2 + 68880\pi^2\eta \\
& - 1916048\eta + 262080) e_t^4 + (4480\eta^3 - 412160\eta^2 - 30135\pi^2\eta + 553008\eta + 342720) e_t^2 \\
& + ((13440\eta^3 + 94640\eta^2 - 113680\eta - 221760) e_t^9 + (-11200\eta^3 - 112000\eta^2 + 12915\pi^2\eta + 692928\eta \\
& - 194880) e_t^7 + (4480\eta^3 + 8960\eta^2 - 43050\pi^2\eta + 1127280\eta - 147840) e_t^5) \cos^5(u) + ((-16240\eta^3 + 12880\eta^2 \\
& + 18480\eta) e_t^{10} + (16240\eta^3 - 91840\eta^2 + 17220\pi^2\eta - 652192\eta + 100800) e_t^8 + (-55440\eta^3 + 34160\eta^2 \\
& - 30135\pi^2\eta - 2185040\eta + 2493120) e_t^6 + (21840\eta^3 + 86800\eta^2 + 163590\pi^2\eta - 5713888\eta + 228480) e_t^4) \\
& \times \cos^4(u) + ((560\eta^3 - 137200\eta^2 + 388640\eta + 241920) e_t^9 + (30800\eta^3 - 264880\eta^2 - 68880\pi^2\eta + 624128\eta \\
& + 766080) e_t^7 + (66640\eta^3 + 612080\eta^2 - 8610\pi^2\eta + 6666080\eta - 6652800) e_t^5 + (-30800\eta^3 - 294000\eta^2 \\
& - 223860\pi^2\eta + 9386432\eta) e_t^3) \cos^3(u) + 67200\eta^2 + ((4480\eta^3 - 20160\eta^2 + 16800\eta) e_t^{10} \\
& + (3920\eta^3 + 475440\eta^2 - 17220\pi^2\eta + 831952\eta - 725760) e_t^8 + (-75600\eta^3 + 96880\eta^2 + 154980\pi^2\eta \\
& - 3249488\eta - 685440) e_t^6 + (5040\eta^3 - 659120\eta^2 + 25830\pi^2\eta - 7356624\eta + 6948480) e_t^4 \\
& + (-5040\eta^3 + 190960\eta^2 + 137760\pi^2\eta - 7307920\eta + 107520) e_t^2) \cos^2(u) - 761600\eta \\
& + ((-2240\eta^3 - 168000\eta^2 - 424480\eta) e_t^9 + (28560\eta^3 + 242480\eta^2 + 34440\pi^2\eta - 1340224\eta + 725760) e_t^7 \\
& + (-33040\eta^3 - 754880\eta^2 - 172200\pi^2\eta + 5458480\eta - 221760) e_t^5 + (40880\eta^3 + 738640\eta^2 + 30135\pi^2\eta \\
& + 1554048\eta - 2936640) e_t^3 + (-560\eta^3 - 100240\eta^2 - 43050\pi^2\eta + 3284816\eta - 389760) e_t) \cos(u) \\
& + \sqrt{1-e_t^2} \left(((-127680\eta^2 + 544320\eta - 739200) e_t^7 + (-53760\eta^2 - 8610\pi^2\eta + 674240\eta - 67200) e_t^5) \cos^5(u) \right. \\
& + ((161280\eta^2 - 477120\eta + 537600) e_t^8 + (477120\eta^2 + 17220\pi^2\eta - 2894080\eta + 2217600) e_t^6 \\
& + (268800\eta^2 + 25830\pi^2\eta - 2721600\eta + 1276800) e_t^4) \cos^4(u) + ((-524160\eta^2 + 1122240\eta - 940800) e_t^7 \\
& + (-873600\eta^2 - 68880\pi^2\eta + 7705600\eta - 3897600) e_t^5 + (-416640\eta^2 - 17220\pi^2\eta \\
& + 3357760\eta - 3225600) e_t^3) \cos^3(u) + ((604800\eta^2 - 504000\eta - 403200) e_t^6 + (1034880\eta^2 + 103320\pi^2\eta \\
& - 11195520\eta + 5779200) e_t^4 + (174720\eta^2 - 17220\pi^2\eta - 486080\eta + 2688000) e_t^2) \cos^2(u) \\
& + ((-282240\eta^2 - 450240\eta + 1478400) e_t^5 + (-719040\eta^2 - 68880\pi^2\eta + 8128960\eta - 5040000) e_t^3 \\
& + (94080\eta^2 + 25830\pi^2\eta - 1585920\eta - 470400) e_t) \cos(u) - 67200\eta^2 + 761600\eta \\
& \left. + e_t^4 (40320\eta^2 + 309120\eta - 672000) + e_t^2 (208320\eta^2 + 17220\pi^2\eta - 2289280\eta + 1680000) \right. \\
& \left. - 8610\eta\pi^2 - 201600) + 8610\eta\pi^2 + 201600 \right].
\end{aligned} \tag{A10}$$

The mean anomaly l^{NS} of the nonspinning eccentric BBH can be expressed as

$$l^{\text{NS}} = u - e_t \sin u + l_{2\text{PN}}^{\text{NS}} x^2 + l_{3\text{PN}}^{\text{NS}} x^3 + \mathcal{O}(x^4), \tag{A11}$$

where the coefficients can be expressed as

$$l_{2\text{PN}}^{\text{NS}} = \frac{1}{8\sqrt{1-e_t^2}(1-e_t \cos(u))} \left[24(2\eta - 5) \tan^{-1} \left(\frac{\sin(u)\beta_\phi}{1 - \cos(u)\beta_\phi} \right) (e_t \cos(u) - 1) - e_t \sqrt{1-e_t^2} (\eta - 15) \eta \sin(u) \right] \tag{A12}$$

$$\begin{aligned}
l_{3\text{PN}}^{\text{NS}} = & \frac{1}{6720(1-e_t^2)^{3/2}(1-e_t \cos(u))^3} \left[35(96(11\eta^2 - 29\eta + 30)e_t^2 + 960\eta^2 \right. \\
& - 2\eta(-13184 + 123\pi^2) + 8640) \tan^{-1} \left(\frac{\sin(u)\beta_\phi}{1 - \cos(u)\beta_\phi} \right) (e_t \cos(u) - 1)^3 + 3360(24(2\eta - 5) \tan^{-1} \left(\frac{\sin(u)\beta_\phi}{1 - \cos(u)\beta_\phi} \right) \\
& + 12e_t(2\eta - 5) \cos(u)(-2 \tan^{-1} \left(\frac{\sin(u)\beta_\phi}{1 - \cos(u)\beta_\phi} \right) + e_t \sqrt{1 - e_t^2}(\eta - 15)\eta \sin(u)) (e_t \cos(u) - 1)^2 \\
& + e_t \sqrt{1 - e_t^2} (140(13e_t^4 - 11e_t^2 - 2)\eta^3 - 140(73e_t^4 - 325e_t^2 + 444)\eta^2 + (3220e_t^4 - 148960e_t^2 - 4305\pi^2 \\
& + 143868)\eta + e_t^2(1820(e_t^2 - 1)\eta^3 - 140(83e_t^2 + 109)\eta^2 - (1120e_t^2 + 4305\pi^2 + 752)\eta + 67200) \cos^2(u) \\
& \left. - 2e_t(1960(e_t^2 - 1)\eta^3 + 6720(e_t^2 - 5)\eta^2 + (-71820e_t^2 - 4305\pi^2 + 69948)\eta + 67200) \cos(u) + 67200) \sin(u) \right], \tag{A13}
\end{aligned}$$

where β_ϕ is given by

$$\beta_\phi = \frac{1 - \sqrt{1 - e_\phi^2}}{e_\phi}, \tag{A14}$$

where phase eccentricity e_ϕ is given by

$$e_\phi = e_t + e_{\phi 1\text{PN}}x + e_{\phi 2\text{PN}}x^2 + e_{\phi 3\text{PN}}x^3 + \mathcal{O}(x^4), \tag{A15}$$

where the coefficients can be expressed as

$$e_{\phi 1\text{PN}} = -e_t(\eta - 4), \tag{A16}$$

$$e_{\phi 2\text{PN}} = \frac{e_t}{96(e_t^2 - 1)} \left[(41\eta^2 - 659\eta + 1152)e_t^2 + 4\eta^2 + 68\eta + \sqrt{1 - e_t^2}(288\eta - 720) - 1248 \right], \tag{A17}$$

$$\begin{aligned}
e_{\phi 3\text{PN}} = & -\frac{e_t}{26880(1 - e_t^2)^{5/2}} \left[(13440\eta^2 + 483840\eta - 940800)e_t^4 + (255360\eta^2 + 17220\pi^2\eta - 2880640\eta \right. \\
& + 2688000)e_t^2 - 268800\eta^2 + 2396800\eta + \sqrt{1 - e_t^2}((1050\eta^3 - 134050\eta^2 + 786310\eta - 860160)e_t^4 \\
& + (-18900\eta^3 + 553980\eta^2 + 4305\pi^2\eta - 1246368\eta + 2042880)e_t^2 + 276640\eta^2 + 2674480\eta - 17220\eta\pi^2 \\
& \left. - 1451520) - 17220\eta\pi^2 - 1747200 \right]. \tag{A18}
\end{aligned}$$

The mean motion n^{NS} of the nonspinning eccentric BBH can be expressed as

$$j^{\text{NS}} = n^{\text{NS}} = x^{3/2} + n_{1\text{PN}}^{\text{NS}}x^{5/2} + n_{2\text{PN}}^{\text{NS}}x^{7/2} + n_{3\text{PN}}^{\text{NS}}x^{9/2} + \mathcal{O}(x^{11/2}), \tag{A19}$$

where the coefficients can be expressed as

$$n_{1\text{PN}}^{\text{NS}} = \frac{3}{e_t^2 - 1}, \tag{A20}$$

$$n_{2\text{PN}}^{\text{NS}} = \frac{(26\eta - 51)e_t^2 + 28\eta - 18}{4(e_t^2 - 1)^2}, \tag{A21}$$

$$\begin{aligned}
n_{3\text{PN}}^{\text{NS}} = & \frac{-1}{128(1 - e_t^2)^{7/2}} \left[(1536\eta - 3840)e_t^4 + (1920 - 768\eta)e_t^2 - 768\eta + \sqrt{1 - e_t^2}((1040\eta^2 - 1760\eta + 2496)e_t^4 \right. \\
& \left. + (5120\eta^2 + 123\pi^2\eta - 17856\eta + 8544)e_t^2 + 896\eta^2 - 14624\eta + 492\eta\pi^2 - 192) + 1920 \right] \tag{A22}
\end{aligned}$$

The radiative dynamics at the 3PN level that we employ is sourced from Ref. [81–83], encompassing both instantaneous and hereditary components expressed in terms of PN expansion parameters x and temporal eccentricity e_t .

The PN expansion parameters \dot{x}^{NS} for the nonspinning eccentric BBH system under the ADM coordinate system can be decomposed into instantaneous and hereditary components as

$$\dot{x}^{\text{NS}} = \dot{x}_{\text{inst}}^{\text{NS}} + \dot{x}_{\text{hered}}^{\text{NS}}, \quad (\text{A23})$$

where instantaneous component is given by

$$\dot{x}_{\text{inst}}^{\text{NS}} = \frac{2c^3\eta}{3GM} x^5 (\dot{x}_{\text{Newt}}^{\text{NS}} + \dot{x}_{1\text{PN}}^{\text{NS}} x + \dot{x}_{2\text{PN}}^{\text{NS}} x^2 + \dot{x}_{3\text{PN}}^{\text{NS}} x^3), \quad (\text{A24})$$

where the coefficients can be expressed as

$$\dot{x}_{\text{Newt}}^{\text{NS}} = \frac{1}{(1-e_t^2)^{7/2}} \left\{ \frac{96}{5} + \frac{292}{5} e_t^2 + \frac{37}{5} e_t^4 \right\}, \quad (\text{A25})$$

$$\dot{x}_{1\text{PN}}^{\text{NS}} = \frac{1}{(1-e_t^2)^{9/2}} \left\{ -\frac{1486}{35} - \frac{264}{5} \eta + e_t^2 \left(\frac{2193}{7} - 570\eta \right) + e_t^4 \left(\frac{12217}{20} - \frac{5061}{10} \eta \right) + e_t^6 \left(\frac{11717}{280} - \frac{148}{5} \eta \right) \right\}, \quad (\text{A26})$$

$$\begin{aligned} \dot{x}_{2\text{PN}}^{\text{NS}} = & \frac{1}{(1-e_t^2)^{11/2}} \left\{ -\frac{11257}{945} + \frac{15677}{105} \eta + \frac{944}{15} \eta^2 + e_t^2 \left(-\frac{2960801}{945} - \frac{2781}{5} \eta + \frac{182387}{90} \eta^2 \right) + e_t^4 \left(-\frac{68647}{1260} \right. \right. \\ & \left. \left. - \frac{1150631}{140} \eta + \frac{396443}{72} \eta^2 \right) + e_t^6 \left(\frac{925073}{336} - \frac{199939}{48} \eta + \frac{192943}{90} \eta^2 \right) + e_t^8 \left(\frac{391457}{3360} - \frac{6037}{56} \eta + \frac{2923}{45} \eta^2 \right) \right. \\ & \left. + \sqrt{1-e_t^2} \left[\left(48 - \frac{96}{5} \eta \right) + e_t^2 \left(2134 - \frac{4268}{5} \eta \right) + e_t^4 \left(2193 - \frac{4386}{5} \eta \right) + e_t^6 \left(\frac{175}{2} - 35\eta \right) \right] \right\}, \quad (\text{A27}) \end{aligned}$$

$$\begin{aligned} \dot{x}_{3\text{PN}}^{\text{NS}} = & \frac{1}{(1-e_t^2)^{13/2}} \left\{ \frac{614389219}{148500} + \left[-\frac{57265081}{11340} + \frac{369}{2} \pi^2 \right] \eta - \frac{16073}{140} \eta^2 - \frac{1121}{27} \eta^3 + e_t^2 \left(\frac{19769277811}{693000} \right. \right. \\ & \left. \left. + \left[\frac{66358561}{3240} + \frac{42571}{80} \pi^2 \right] \eta - \frac{3161701}{840} \eta^2 - \frac{1287385}{324} \eta^3 \right) + e_t^4 \left(-\frac{3983966927}{8316000} + \left[\frac{6451690597}{90720} \right. \right. \right. \\ & \left. \left. - \frac{12403}{64} \pi^2 \right] \eta + \frac{34877019}{1120} \eta^2 - \frac{33769597}{1296} \eta^3 \right) + e_t^6 \left(-\frac{4548320963}{5544000} + \left[-\frac{59823689}{4032} - \frac{242563}{640} \pi^2 \right] \eta \right. \\ & \left. + \frac{411401857}{6720} \eta^2 - \frac{3200965}{108} \eta^3 \right) + e_t^8 \left(\frac{19593451667}{2464000} + \left[-\frac{6614711}{480} - \frac{12177}{640} \pi^2 \right] \eta + \frac{92762}{7} \eta^2 - \frac{982645}{162} \eta^3 \right) \\ & \left. + e_t^{10} \left(\frac{33332681}{197120} - \frac{1874543}{10080} \eta + \frac{109733}{840} \eta^2 - \frac{8288}{81} \eta^3 \right) + \sqrt{1-e_t^2} \left[-\frac{1425319}{1125} + \left[\frac{9874}{105} - \frac{41}{10} \pi^2 \right] \eta + \frac{632}{5} \eta^2 \right. \right. \\ & \left. \left. + e_t^2 \left(\frac{933454}{375} + \left[-\frac{2257181}{63} + \frac{45961}{240} \pi^2 \right] \eta + \frac{125278}{15} \eta^2 \right) + e_t^4 \left(\frac{840635951}{21000} + \left[-\frac{4927789}{60} + \frac{6191}{32} \pi^2 \right] \eta \right. \right. \\ & \left. \left. + \frac{317273}{15} \eta^2 \right) + e_t^6 \left(\frac{702667207}{31500} + \left[-\frac{6830419}{252} + \frac{287}{960} \pi^2 \right] \eta + \frac{232177}{30} \eta^2 \right) + e_t^8 \left(\frac{56403}{112} - \frac{427733}{840} \eta + \frac{4739}{30} \eta^2 \right) \right] \\ & \left. + \left(\frac{54784}{175} + \frac{465664}{105} e_t^2 + \frac{4426376}{525} e_t^4 + \frac{1498856}{525} e_t^6 + \frac{31779}{350} e_t^8 \right) \ln \left[\frac{x}{x_0} \frac{1 + \sqrt{1-e_t^2}}{2(1-e_t^2)} \right] \right\}, \quad (\text{A28}) \end{aligned}$$

where the constant x_0 serves the purpose of removing the logarithmic term related to gauge dependence. This constant is present in the hereditary term as well, and their contributions can offset each other. Consequently, in Eq. (A28), the choice of x_0 does not impact the ultimate computational outcome.

And hereditary component is given by

$$\dot{x}_{\text{hered}}^{\text{NS}} = \frac{64c^3\eta}{5GM} x^4 (\dot{x}_{1.5\text{PN}}^{\text{NS}} x^{3/2} + \dot{x}_{2.5\text{PN}}^{\text{NS}} x^{5/2} + \dot{x}_{3\text{PN}}^{\text{NS}} x^3), \quad (\text{A29})$$

where the coefficients can be expressed as

$$\dot{x}_{1.5\text{PN}}^{\text{NS}} = 4\pi\varphi(e_t) \quad (\text{A30})$$

$$\dot{x}_{2.5\text{PN}}^{\text{NS}} = \pi \left[-\frac{4159}{672} \psi_x(e_t) - \frac{189}{8} \eta \zeta_x(e_t) \right], \quad (\text{A31})$$

$$\dot{x}_{3\text{PN}}^{\text{NS}} = -\frac{116761}{3675} \kappa(e_t) + \left[\frac{16}{3} \pi^2 - \frac{1712}{105} C - \frac{1712}{105} \ln\left(\frac{6x}{x_0}\right) \right] F(e_t), \quad (\text{A32})$$

where C represents Euler's constant, with a value of 0.577. And $\varphi(e_t)$, $\psi_x(e_t)$, $\zeta_x(e_t)$, $\kappa(e_t)$ and $F(e_t)$ represent some special functions, among which only $F(e_t)$ has an analytical form, which can be expressed as

$$F(e_t) = \frac{1 + \frac{85}{6} e_t^2 + \frac{5171}{192} e_t^4 + \frac{1751}{192} e_t^6 + \frac{297}{1024} e_t^8}{(1 - e_t^2)^{13/2}}. \quad (\text{A33})$$

While other special functions can be represented in series form, the analytical formulas are not provided in Ref. [81–83]; only expansions for small eccentricities are offered. Nonetheless, these expansions are unsuitable for the waveform under consideration as they are designed for eccentricities below 0.1 and may provide inaccurate outcomes when applied beyond this threshold. Nevertheless, by interpolating the data from the table in Appendix B of Ref. [81], accurate results can still be obtained.

In principle, the calculation results should be converted into the harmonic coordinate system. However, as x is a gauge invariant quantity, such a transformation is deemed unnecessary.

The temporal eccentricity \dot{e}_t^{NS} for the nonspinning eccentric BBH system under the ADM coordinate system can be decomposed into instantaneous and hereditary components as

$$\dot{e}_t^{\text{NS}} = \dot{e}_{t\text{inst}}^{\text{NS}} + \dot{e}_{t\text{hered}}^{\text{NS}}, \quad (\text{A34})$$

where instantaneous component is given by

$$\dot{e}_{t\text{inst}}^{\text{NS}} = -\frac{c^3 \eta}{GM} e_t x^4 \left(\dot{e}_{t\text{Newt}}^{\text{NS}} + \dot{e}_{t1\text{PN}}^{\text{NS}} x + \dot{e}_{t2\text{PN}}^{\text{NS}} x^2 + \dot{e}_{t3\text{PN}}^{\text{NS}} x^3 \right), \quad (\text{A35})$$

where the coefficients can be expressed as

$$\dot{e}_{t\text{Newt}}^{\text{NS}} = \frac{1}{(1 - e_t^2)^{5/2}} \left\{ \frac{304}{15} + \frac{121 e_t^2}{15} \right\} \quad (\text{A36})$$

$$\dot{e}_{t1\text{PN}}^{\text{NS}} = \frac{1}{(1 - e_t^2)^{7/2}} \left\{ -\frac{939}{35} - \frac{4084}{45} \eta + e_t^2 \left(\frac{29917}{105} - \frac{7753}{30} \eta \right) + e_t^4 \left(\frac{13929}{280} - \frac{1664}{45} \eta \right) \right\}, \quad (\text{A37})$$

$$\begin{aligned} \dot{e}_{t2\text{PN}}^{\text{NS}} = & \frac{1}{(1 - e_t^2)^{9/2}} \left\{ -\frac{961973}{1890} + \frac{70967}{210} \eta + \frac{752}{5} \eta^2 + e_t^2 \left(-\frac{3180307}{2520} - \frac{1541059}{840} \eta + \frac{64433}{40} \eta^2 \right) \right. \\ & + e_t^4 \left(\frac{23222071}{15120} - \frac{13402843}{5040} \eta + \frac{127411}{90} \eta^2 \right) + e_t^6 \left(\frac{420727}{3360} - \frac{362071}{2520} \eta + \frac{821}{9} \eta^2 \right) \\ & \left. + \sqrt{1 - e_t^2} \left[\frac{1336}{3} - \frac{2672}{15} \eta + e_t^2 \left(\frac{2321}{2} - \frac{2321}{5} \eta \right) + e_t^4 \left(\frac{565}{6} - \frac{113}{3} \eta \right) \right] \right\}, \quad (\text{A38}) \end{aligned}$$

$$\begin{aligned}
\dot{e}_{t3\text{PN}}^{\text{NS}} = & \frac{1}{(1-e_t^2)^{11/2}} \left\{ \frac{54177075619}{6237000} + \left[\frac{7198067}{22680} + \frac{1283}{10}\pi^2 \right] \eta - \frac{3000281}{2520}\eta^2 - \frac{61001}{486}\eta^3 + e_t^2 \left(\frac{6346360709}{891000} \right. \right. \\
& + \left[\frac{9569213}{360} + \frac{54001}{960}\pi^2 \right] \eta + \frac{12478601}{15120}\eta^2 - \frac{86910509}{19440}\eta^3 \left. \right) + e_t^4 \left(-\frac{126288160777}{16632000} + \left[\frac{418129451}{181440} \right. \right. \\
& - \left. \frac{254903}{1920}\pi^2 \right] \eta + \frac{478808759}{20160}\eta^2 - \frac{2223241}{180}\eta^3 \left. \right) + e_t^6 \left(\frac{5845342193}{1232000} + \left[-\frac{98425673}{10080} - \frac{6519}{640}\pi^2 \right] \eta \right. \\
& + \left. \frac{6538757}{630}\eta^2 - \frac{11792069}{2430}\eta^3 \right) + e_t^8 \left(\frac{302322169}{1774080} - \frac{1921387}{10080}\eta + \frac{41179}{216}\eta^2 - \frac{193396}{1215}\eta^3 \right) \\
& + \sqrt{1-e_t^2} \left[-\frac{22713049}{15750} + \left[-\frac{5526991}{945} + \frac{8323}{180}\pi^2 \right] \eta + \frac{54332}{45}\eta^2 + e_t^2 \left(\frac{89395687}{7875} + \left[-\frac{38295557}{1260} \right. \right. \right. \\
& + \left. \left. \frac{94177}{960}\pi^2 \right] \eta + \frac{681989}{90}\eta^2 \right) + e_t^4 \left(\frac{5321445613}{378000} + \left[-\frac{26478311}{1512} + \frac{2501}{2880}\pi^2 \right] \eta + \frac{225106}{45}\eta^2 \right) \\
& + e_t^6 \left(\frac{186961}{336} - \frac{289691}{504}\eta + \frac{3197}{18}\eta^2 \right) \left. \right] + \frac{730168}{23625} \frac{1}{1+\sqrt{1-e_t^2}} \\
& + \frac{304}{15} \left(\frac{82283}{1995} + \frac{297674}{1995}e_t^2 + \frac{1147147}{15960}e_t^4 + \frac{61311}{21280}e_t^6 \right) \ln \left[\frac{x}{x_0} \frac{1+\sqrt{1-e_t^2}}{2(1-e_t^2)} \right] \left. \right\}. \tag{A39}
\end{aligned}$$

And hereditary component is given by

$$\dot{e}_{t\text{hered}}^{\text{NS}} = \frac{32c^3\eta}{5GM} e_t x^4 \left(\dot{e}_{t1.5\text{PN}}^{\text{NS}} x^{3/2} + \dot{e}_{t2.5\text{PN}}^{\text{NS}} x^{5/2} + \dot{e}_{t3\text{PN}}^{\text{NS}} x^3 \right), \tag{A40}$$

where the coefficients can be expressed as

$$\dot{e}_{t1.5\text{PN}}^{\text{NS}} = -\frac{985}{48} \pi \varphi_e(e_t), \tag{A41}$$

$$\dot{e}_{t2.5\text{PN}}^{\text{NS}} = \pi \left[\frac{55691}{1344} \psi_e(e_t) + \frac{19067}{126} \eta \zeta_e(e_t) \right], \tag{A42}$$

$$\dot{e}_{t3\text{PN}}^{\text{NS}} = \left(\frac{89789209}{352800} - \frac{87419}{630} \ln 2 + \frac{78003}{560} \ln 3 \right) \times \kappa_e(e_t) - \frac{769}{96} \left[\frac{16}{3} \pi^2 - \frac{1712}{105} C - \frac{1712}{105} \ln \left(\frac{6x}{x_0} \right) \right] F_e(e_t), \tag{A43}$$

where $\varphi_e(e_t)$, $\psi_e(e_t)$, $\zeta_e(e_t)$, $\kappa_e(e_t)$ and $F_e(e_t)$ represent some special functions, among which only $F_e(e_t)$ has an analytical form, which can be expressed as

$$F_e(e_t) = \frac{1 + \frac{2782}{769}e_t^2 + \frac{10721}{6152}e_t^4 + \frac{1719}{24608}e_t^6}{(1-e_t^2)^{11/2}}. \tag{A44}$$

Similarly, accurate results for the other four special functions can be obtained by interpolating the data presented in the table in Appendix B of Ref. [81]. Moreover, as previously mentioned, it is imperative to convert e_t from ADM coordinates to harmonic coordinates. The transformation formula is as follows [81]:

$$\frac{e_t^{\text{MH}}}{e_t^{\text{ADM}}} = 1 + \frac{x^2}{1-e_t^2} \left(-\frac{1}{4} - \frac{17}{4}\eta \right) + \frac{x^3}{(1-e_t^2)^2} \left(-\frac{1}{2} + \left[-\frac{16739}{1680} + \frac{21}{16}\pi^2 \right] \eta + \frac{83}{24}\eta^2 + e_t^2 \left(-\frac{1}{2} - \frac{249}{16}\eta + \frac{241}{24}\eta^2 \right) \right), \tag{A45}$$

where the superscript MH denotes modified harmonic coordinates, with the right-hand side of the equation represented in ADM coordinates.

The 22 mode of the gravitational waveform $h^{22,\text{NS}}$ for the nonspinning eccentric BBH system, as provided in Ref. [85–87], can be expressed as

$$h^{22,\text{NS}} = \frac{4GM\eta}{c^2 R} \sqrt{\frac{\pi}{5}} e^{-2i\phi} H^{22,\text{NS}}, \tag{A46}$$

where amplitude $H^{22,\text{NS}}$ can be expressed as the sum of different PN orders,

$$H^{22,\text{NS}} = H_{\text{Newt}}^{22,\text{NS}} + H_{1\text{PN}}^{22,\text{NS}} + H_{2\text{PN}}^{22,\text{NS}} + H_{2.5\text{PN}}^{22,\text{NS}} + H_{3\text{PN}}^{22,\text{NS}}, \quad (\text{A47})$$

where the individual PN terms read as

$$H_{\text{Newt}}^{22,\text{NS}} = \frac{GM}{r} + r^2 \dot{\phi}^2 + 2ir\dot{\phi} - \dot{r}^2, \quad (\text{A48})$$

$$H_{1\text{PN}}^{22,\text{NS}} = \frac{1}{c^2} \left[\frac{G^2 M^2}{r^2} \left(-5 + \frac{\eta}{2} \right) + \frac{GM\dot{r}^2}{r} \left(-\frac{15}{14} - \frac{16\eta}{7} \right) + \left(-\frac{9}{14} + \frac{27\eta}{14} \right) \dot{r}^4 + r \left(\frac{9i}{7} - \frac{27i\eta}{7} \right) \dot{r}^3 \dot{\phi} \right. \\ \left. + GMr \left(\frac{11}{42} + \frac{26\eta}{7} \right) \dot{\phi}^2 + r^4 \left(\frac{9}{14} - \frac{27\eta}{14} \right) \dot{\phi}^4 + \dot{r} \left(GM \left(\frac{25i}{21} + \frac{45i\eta}{7} \right) \dot{\phi} + r^3 \left(\frac{9i}{7} - \frac{27i\eta}{7} \right) \dot{\phi}^3 \right) \right] \quad (\text{A49})$$

$$H_{2\text{PN}}^{22,\text{NS}} = \frac{1}{c^4} \left[\frac{G^3 M^3}{r^3} \left(\frac{757}{63} + \frac{181\eta}{36} + \frac{79\eta^2}{126} \right) + \left(-\frac{83}{168} + \frac{589\eta}{168} - \frac{1111\eta^2}{168} \right) \dot{r}^6 + r \left(\frac{83i}{84} - \frac{589i\eta}{84} + \frac{1111i\eta^2}{84} \right) \dot{r}^5 \dot{\phi} \right. \\ \left. + G^2 M^2 \left(-\frac{11891}{1512} - \frac{5225\eta}{216} + \frac{13133\eta^2}{1512} \right) \dot{\phi}^2 + GMr^3 \left(\frac{835}{252} + \frac{19\eta}{252} - \frac{2995\eta^2}{252} \right) \dot{\phi}^4 \right. \\ \left. + r^6 \left(\frac{83}{168} - \frac{589\eta}{168} + \frac{1111\eta^2}{168} \right) \dot{\phi}^6 + \dot{r}^4 \left(\frac{GM}{r} \left(-\frac{557}{168} + \frac{83\eta}{21} + \frac{214\eta^2}{21} \right) + r^2 \left(-\frac{83}{168} + \frac{589\eta}{168} - \frac{1111\eta^2}{168} \right) \dot{\phi}^2 \right) \right. \\ \left. + \dot{r}^3 \left(GM \left(\frac{863i}{126} - \frac{731i\eta}{63} - \frac{211i\eta^2}{9} \right) \dot{\phi} + r^3 \left(\frac{83i}{42} - \frac{589i\eta}{42} + \frac{1111i\eta^2}{42} \right) \dot{\phi}^3 \right) \right. \\ \left. + \dot{r}^2 \left(\frac{G^2 M^2}{r^2} \left(\frac{619}{252} - \frac{2789\eta}{252} - \frac{467\eta^2}{126} \right) + GMr \left(\frac{11}{28} - \frac{169\eta}{14} - \frac{58\eta^2}{21} \right) \dot{\phi}^2 + r^4 \left(\frac{83}{168} - \frac{589\eta}{168} + \frac{1111\eta^2}{168} \right) \dot{\phi}^4 \right) \right. \\ \left. + \dot{r} \left(\frac{G^2 M^2}{r} \left(-\frac{773i}{189} - \frac{3767i\eta}{189} + \frac{2852i\eta^2}{189} \right) \dot{\phi} + GMr^2 \left(\frac{433i}{84} + \frac{103i\eta}{12} - \frac{1703i\eta^2}{84} \right) \dot{\phi}^3 \right. \right. \\ \left. \left. + r^5 \left(\frac{83i}{84} - \frac{589i\eta}{84} + \frac{1111i\eta^2}{84} \right) \dot{\phi}^5 \right) \right], \quad (\text{A50})$$

$$H_{2.5\text{PN}}^{22,\text{NS}} = \frac{1}{c^5} \left[-\frac{122G^2 M^2 \eta \dot{r}^3}{35r^2} - \frac{468iG^3 M^3 \eta \dot{\phi}}{35r^2} + \frac{184iG^2 M^2 \eta \dot{r}^2 \dot{\phi}}{35r} - \frac{316}{35} iG^2 M^2 r \eta \dot{\phi}^3 + \dot{r} \left(\frac{2G^3 M^3 \eta}{105r^3} - \frac{121}{5} G^2 M^2 \eta \dot{\phi}^2 \right) \right], \quad (\text{A51})$$

$$\begin{aligned}
H_{3\text{PN}}^{22,\text{NS}} = & \frac{1}{c^6} \left[\frac{G^4 M^4}{r^4} \left(-\frac{512714}{51975} + \left(-\frac{1375951}{13860} + \frac{41\pi^2}{16} \right) \eta + \frac{1615\eta^2}{616} + \frac{2963\eta^3}{4158} \right) \right. \\
& + \left(-\frac{507}{1232} + \frac{6101\eta}{1232} - \frac{12525\eta^2}{616} + \frac{34525\eta^3}{1232} \right) \dot{r}^8 + r \left(\frac{507i}{616} - \frac{6101i\eta}{616} + \frac{12525i\eta^2}{308} - \frac{34525i\eta^3}{616} \right) \dot{r}^7 \dot{\phi} \\
& + \frac{G^3 m^3}{r} \left(\frac{42188851}{415800} + \left(\frac{190703}{3465} - \frac{123\pi^2}{64} \right) \eta - \frac{18415\eta^2}{308} + \frac{281473\eta^3}{16632} \right) \dot{\phi}^2 \\
& + G^2 M^2 r^2 \left(\frac{328813}{55440} - \frac{374651\eta}{33264} + \frac{249035\eta^2}{4158} - \frac{1340869\eta^3}{33264} \right) \dot{\phi}^4 \\
& + GM r^5 \left(\frac{12203}{2772} - \frac{36427\eta}{2772} - \frac{13667\eta^2}{1386} + \frac{49729\eta^3}{924} \right) \dot{\phi}^6 + r^8 \left(\frac{507}{1232} - \frac{6101\eta}{1232} + \frac{12525\eta^2}{616} - \frac{34525\eta^3}{1232} \right) \dot{\phi}^8 \\
& + r^4 \left(\frac{G^2 M^2}{r^2} \left(-\frac{92567}{13860} + \frac{7751\eta}{396} + \frac{400943\eta^2}{11088} + \frac{120695\eta^3}{3696} \right) \right. \\
& + GM r \left(-\frac{42811}{11088} + \frac{6749\eta}{1386} + \frac{19321\eta^2}{693} - \frac{58855\eta^3}{1386} \right) \dot{\phi}^2 \left. + r^6 \left(\frac{GM}{r} \left(-\frac{5581}{1232} + \frac{4694\eta}{231} - \frac{3365\eta^2}{462} - \frac{1850\eta^3}{33} \right) \right. \right. \\
& + r^2 \left(-\frac{507}{616} + \frac{6101\eta}{616} - \frac{12525\eta^2}{308} + \frac{34525\eta^3}{616} \right) \dot{\phi}^2 \left. + r^5 \left(GM \left(\frac{17233i}{1848} - \frac{31532i\eta}{693} + \frac{65575i\eta^2}{2772} + \frac{85145i\eta^3}{693} \right) \right. \right. \\
& + r^3 \left(\frac{1521i}{616} - \frac{18303i\eta}{616} + \frac{37575i\eta^2}{308} - \frac{103575i\eta^3}{616} \right) \dot{\phi}^3 \left. \right) \\
& + r^3 \left(\frac{G^2 M^2}{r} \left(\frac{39052i}{3465} - \frac{154114i\eta}{2079} - \frac{246065i\eta^2}{4158} - \frac{365725i\eta^3}{4158} \right) \right) \dot{\phi}^5 \\
& + GM r^2 \left(\frac{13867i}{792} - \frac{191995i\eta}{2772} - \frac{8741i\eta^2}{5544} + \frac{52700i\eta^3}{231} \right) \dot{\phi}^3 + r^5 \left(\frac{1521i}{616} - \frac{18303i\eta}{616} + \frac{37575i\eta^2}{308} - \frac{103575i\eta^3}{616} \right) \dot{\phi}^5 \\
& + r^2 \left(\frac{G^3 M^3}{r^3} \left(\frac{913799}{29700} + \left(\frac{174679}{2310} + \frac{123\pi^2}{32} \right) \eta - \frac{158215\eta^2}{2772} - \frac{12731\eta^3}{4158} \right) \right. \\
& + G^2 M^2 \left(\frac{20191}{18480} - \frac{3879065\eta}{33264} - \frac{411899\eta^2}{8316} - \frac{522547\eta^3}{33264} \right) \dot{\phi}^2 \\
& + GM r^3 \left(\frac{381}{77} - \frac{101237\eta}{2772} + \frac{247505\eta^2}{5544} + \frac{394771\eta^3}{5544} \right) \dot{\phi}^4 + r^6 \left(\frac{507}{616} - \frac{6101\eta}{616} + \frac{12525\eta^2}{308} - \frac{34525\eta^3}{616} \right) \dot{\phi}^6 \\
& + r \left(\frac{G^3 M^3}{r^2} \left(-\frac{68735i}{378} + \left(-\frac{57788i}{315} + \frac{123i\pi^2}{32} \right) \eta - \frac{701i\eta^2}{27} + \frac{11365i\eta^3}{378} \right) \right) \dot{\phi}^7 \\
& + G^2 M^2 r \left(\frac{91229i}{13860} + \frac{97861i\eta}{4158} + \frac{919811i\eta^2}{8316} - \frac{556601i\eta^3}{8316} \right) \dot{\phi}^3 \\
& \left. + GM r^4 \left(\frac{6299i}{792} - \frac{68279i\eta}{5544} - \frac{147673i\eta^2}{2772} + \frac{541693i\eta^3}{5544} \right) \dot{\phi}^5 + r^7 \left(\frac{507i}{616} - \frac{6101i\eta}{616} + \frac{12525i\eta^2}{308} - \frac{34525i\eta^3}{616} \right) \dot{\phi}^7 \right]. \tag{A52}
\end{aligned}$$

The high-order harmonic mode for nonspinning BBH can be expressed as

$$h^{\ell m, \text{NS}} = \frac{4GM\eta}{c^4 R} \sqrt{\frac{\pi}{5}} e^{-im\phi} H^{\ell m, \text{NS}}. \tag{A53}$$

For the high-order modes 21, 33, 32, 44, 43, and 55, we simplify by presenting only the amplitude of leading PN order waveform. In regard to the phase, it is important to emphasize that distinct high-order modes require different values of m in Eq. (19) and Eq. (A53).

The amplitudes of the high-order modes 21, 33, 32, 44, 43, and 55 at the leading PN order for nonspinning BBH can be expressed as

$$H_{0.5\text{PN}}^{21,\text{NS}} = \frac{1}{c} \left(\frac{2}{3} i GM \dot{\phi} \sqrt{1-4\eta} \right), \tag{A54}$$

$$H_{0.5\text{PN}}^{33,\text{NS}} = \frac{1}{c} \sqrt{1-4\eta} \left(-\frac{i}{2} \sqrt{\frac{35}{6}} GM \dot{\phi} - i \sqrt{\frac{5}{42}} \dot{\phi}^3 r^3 + \frac{\sqrt{\frac{10}{21}} GM \dot{r}}{r} + \sqrt{\frac{15}{14}} \dot{\phi}^2 r^2 \dot{r} + i \sqrt{\frac{15}{14}} \dot{\phi} r \dot{r}^2 - \sqrt{\frac{5}{42}} \dot{r}^3 \right), \tag{A55}$$

$$H_{1\text{PN}}^{32,\text{NS}} = \frac{1}{c^2} \sqrt{\frac{5}{7}} \left(\frac{2}{3} GM \dot{\phi}^2 r + \frac{i}{6} GM \dot{\phi} \dot{r} - 2GM \dot{\phi}^2 r \eta - \frac{i}{2} GM \dot{\phi} \dot{r} \eta \right), \quad (\text{A56})$$

$$\begin{aligned} H_{1\text{PN}}^{44,\text{NS}} = & \frac{1}{c^2} \left(-\frac{\sqrt{35} G^2 M^2}{36 r^2} - \frac{17}{12} \sqrt{\frac{5}{7}} GM \dot{\phi}^2 r - \frac{1}{6} \sqrt{\frac{5}{7}} \dot{\phi}^4 r^4 - \frac{3i}{2} \sqrt{\frac{5}{7}} GM \dot{\phi} \dot{r} - \frac{2i}{3} \sqrt{\frac{5}{7}} \dot{\phi}^3 r^3 \dot{r} + \frac{\sqrt{\frac{5}{7}} GM \dot{r}^2}{2r} \right. \\ & + \sqrt{\frac{5}{7}} \dot{\phi}^2 r^2 \dot{r}^2 + \frac{2i}{3} \sqrt{\frac{5}{7}} \dot{\phi} r \dot{r}^3 - \frac{1}{6} \sqrt{\frac{5}{7}} \dot{r}^4 + \frac{\sqrt{35} G^2 M^2 \eta}{12 r^2} + \frac{17}{4} \sqrt{\frac{5}{7}} GM \dot{\phi}^2 r \eta + \frac{1}{2} \sqrt{\frac{5}{7}} \dot{\phi}^4 r^4 \eta \\ & \left. + \frac{9i}{2} \sqrt{\frac{5}{7}} GM \dot{\phi} \dot{r} \eta + 2i \sqrt{\frac{5}{7}} \dot{\phi}^3 r^3 \dot{r} \eta - \frac{3\sqrt{\frac{5}{7}} GM \dot{r}^2 \eta}{2r} - 3\sqrt{\frac{5}{7}} \dot{\phi}^2 r^2 \dot{r}^2 \eta - 2i \sqrt{\frac{5}{7}} \dot{\phi} r \dot{r}^3 \eta + \frac{1}{2} \sqrt{\frac{5}{7}} \dot{r}^4 \eta \right), \end{aligned} \quad (\text{A57})$$

$$\begin{aligned} H_{1.5\text{PN}}^{43,\text{NS}} = & \frac{1}{c^3} \sqrt{1-4\eta} \left(-\frac{i\sqrt{\frac{2}{35}} G^2 M^2 \dot{\phi}}{3r} - \frac{23i GM \dot{\phi}^3 r^2}{6\sqrt{70}} + \frac{\sqrt{\frac{5}{14}} GM \dot{\phi}^2 r \dot{r}}{3} + \frac{i GM \dot{\phi} \dot{r}^2}{3\sqrt{70}} \right. \\ & \left. + \frac{2i\sqrt{\frac{2}{35}} G^2 M^2 \dot{\phi} \eta}{3r} + \frac{23i GM \dot{\phi}^3 r^2 \eta}{3\sqrt{70}} - \frac{\sqrt{\frac{10}{7}} GM \dot{\phi}^2 r \dot{r} \eta}{3} - \frac{i\sqrt{\frac{2}{35}} GM \dot{\phi} \dot{r}^2 \eta}{3} \right), \end{aligned} \quad (\text{A58})$$

$$\begin{aligned} H_{1.5\text{PN}}^{55,\text{NS}} = & \frac{1}{c^3} \sqrt{1-4\eta} \left(\frac{43i G^2 M^2 \dot{\phi}}{12\sqrt{66} r} + \frac{13i\sqrt{\frac{11}{6}} GM \dot{\phi}^3 r^2}{16} + \frac{i\dot{\phi}^5 r^5}{2\sqrt{66}} - \frac{41 G^2 M^2 \dot{r}}{24\sqrt{66} r^2} - \frac{13 GM \dot{\phi}^2 r \dot{r}}{\sqrt{66}} - \frac{5\dot{\phi}^4 r^4 \dot{r}}{2\sqrt{66}} \right. \\ & - \frac{i\sqrt{\frac{33}{2}} GM \dot{\phi} \dot{r}^2}{4} - \frac{5i\dot{\phi}^3 r^3 \dot{r}^2}{\sqrt{66}} + \frac{\sqrt{\frac{2}{33}} GM \dot{r}^3}{r} + \frac{5\dot{\phi}^2 r^2 \dot{r}^3}{\sqrt{66}} + \frac{5i\dot{\phi} r \dot{r}^4}{2\sqrt{66}} - \frac{\dot{r}^5}{2\sqrt{66}} - \frac{43i G^2 M^2 \dot{\phi} \eta}{6\sqrt{66} r} \\ & - \frac{13i\sqrt{\frac{11}{6}} GM \dot{\phi}^3 r^2 \eta}{8} - \frac{i\dot{\phi}^5 r^5 \eta}{\sqrt{66}} + \frac{41 G^2 M^2 \dot{r} \eta}{12\sqrt{66} r^2} + \frac{13\sqrt{\frac{2}{33}} GM \dot{\phi}^2 r \dot{r} \eta}{\eta} + \frac{5\dot{\phi}^4 r^4 \dot{r} \eta}{\sqrt{66}} \\ & \left. + \frac{i\sqrt{\frac{33}{2}} GM \dot{\phi} \dot{r}^2 \eta}{2} + \frac{5i\sqrt{\frac{2}{33}} \dot{\phi}^3 r^3 \dot{r}^2 \eta}{\eta} - \frac{2\sqrt{\frac{2}{33}} GM \dot{r}^3 \eta}{r} - \frac{5\sqrt{\frac{2}{33}} \dot{\phi}^2 r^2 \dot{r}^3 \eta}{\eta} - \frac{5i\dot{\phi} r \dot{r}^4 \eta}{\sqrt{66}} + \frac{\dot{r}^5 \eta}{\sqrt{66}} \right). \end{aligned} \quad (\text{A59})$$

2. Spin-aligned waveforms

Building upon the preceding nonspinning setup, this section delves into the 3PN dynamics of spin-aligned BBH in eccentric orbits. We commence by introducing the conservative dynamics at the 3PN level, as detailed in Ref. [89]. The orbital radius r^{SP} of the spin-aligned eccentric BBH can be expressed as

$$r^{\text{SP}} = r^{\text{NS}} + r^{\text{SO}} + r^{\text{SS}}, \quad (\text{A60})$$

where the nonspinning component r^{NS} has been detailed in the preceding section, and the spin-orbit coupling component r^{SO} can be expressed as

$$r^{\text{SO}} = r_{1.5\text{PN}}^{\text{SO}} + r_{2.5\text{PN}}^{\text{SO}}, \quad (\text{A61})$$

$$r_{1.5\text{PN}}^{\text{SO}} = -\frac{2}{3x} \left(-\frac{x}{1-e_t^2} \right)^{3/2} [\delta\chi_A (1+3e_t^2) + \chi_S - 3e_t^2(1-\eta)\chi_S + \eta\chi_S - 4e_t\delta\chi_A \cos u + 2e_t(2-\eta)\chi_S \cos u], \quad (\text{A62})$$

$$\begin{aligned}
r_{2.5\text{PN}}^{\text{SO}} = & \frac{x^{3/2}e^5}{3(1-e_t^2)^3} \left[2(1-e_t^2)^2 \left(2\delta(-3+\eta)\chi_A - (6-8\eta+\eta^2)\chi_S \right) (2+e_t \cos u) \right. \\
& + \sqrt{1-e_t^2} \left(\delta \left(e_t^2(84-33\eta) + e_t^4(12-8\eta) - 4(-6+\eta) \right) \chi_A \right. \\
& + \left. \left(24-28\eta+4e_t^4(3-5\eta+2\eta^2) + e_t^2(84-87\eta+10\eta^2) \right) \chi_S \right. \\
& \left. \left. + e_t \left(\delta \left(-60+17\eta+4e_t^2(-15+7\eta) \right) \chi_A - \left(60-77\eta+4\eta^2+2e_t^2(30-29\eta+7\eta^2) \right) \chi_S \right) \cos u \right) \right].
\end{aligned} \tag{A63}$$

The spin-spin coupling component r^{SS} can be expressed as

$$r^{\text{SS}} = r_{2\text{PN}}^{\text{SS}} + r_{3\text{PN}}^{\text{SS}}, \tag{A64}$$

$$r_{2\text{PN}}^{\text{SS}} = \frac{x}{2(-1+e_t^2)^2} [\kappa_S - 2\kappa_S\eta + \chi_A^2 - 4\eta\chi_A^2 + \chi_S^2 + \delta(\kappa_A + 2\chi_A\chi_S)] (1 + e_t^2 - 2e_t \cos u) \tag{A65}$$

$$\begin{aligned}
r_{3\text{PN}}^{\text{SS}} = & \frac{x^2}{18(1-e_t^2)^3} \left[99\kappa_S + 306e_t^2\kappa_S + 45e_t^4\kappa_S - 252\kappa_S\eta - 750e_t^2\kappa_S\eta - 105e_t^4\kappa_S\eta + 18\kappa_S\eta^2 + 168e_t^2\kappa_S\eta^2 \right. \\
& + 48e_t^4\kappa_S\eta^2 - 3\delta\kappa_A(-33+5e_t^4(-3+\eta) + 18\eta + 2e_t^2(-51+23\eta)) + 139\chi_A^2 + 474e_t^2\chi_A^2 + 45e_t^4\chi_A^2 \\
& - 574\eta\chi_A^2 - 2007e_t^2\eta\chi_A^2 - 213e_t^4\eta\chi_A^2 + 36\eta^2\chi_A^2 + 336e_t^2\eta^2\chi_A^2 + 96e_t^4\eta^2\chi_A^2 + 2\delta(139+e_t^2(474-309\eta) \\
& + e_t^4(45-33\eta) - 122\eta) \chi_A\chi_S + 139\chi_S^2 + 474e_t^2\chi_S^2 + 45e_t^4\chi_S^2 - 226\eta\chi_S^2 - 507e_t^2\eta\chi_S^2 - 33e_t^4\eta\chi_S^2 \\
& + 40\eta^2\chi_S^2 + 120e_t^2\eta^2\chi_S^2 + e_t[-3\kappa_S(72-178\eta+20\eta^2 + e_t^2(78-191\eta+58\eta^2)) \\
& + \delta(3\kappa_A(-72+34\eta+e_t^2(-78+35\eta)) + 4(-176+157\eta+3e_t^2(-51+25\eta)) \chi_A\chi_S] \\
& - 2[(176-737\eta+60\eta^2+3e_t^2(51-220\eta+58\eta^2))\chi_A^2 + (176-281\eta+80\eta^2-51e_t^2(-3+2\eta))\chi_S^2] \cos u \\
& + 3(1-e_t^2)^{3/2} [\delta\kappa_A(-14+5\eta) + \kappa_S(-14+33\eta-6\eta^2) + 4\delta(-11+9\eta)\chi_A\chi_S - 2[(11-46\eta+6\eta^2)\chi_A^2 \\
& \left. + (11-16\eta+4\eta^2)\chi_S^2] \right] (2+e_t \cos u) \Big],
\end{aligned} \tag{A66}$$

where we introduce some new quantities

$$\chi_S \equiv \frac{1}{2}(\chi_1 + \chi_2), \tag{A67}$$

$$\chi_A \equiv \frac{1}{2}(\chi_1 - \chi_2), \tag{A68}$$

$$\kappa_S \equiv \frac{1}{2}((\kappa_1 - 1)\chi_1^2 + (\kappa_2 - 1)\chi_2^2), \tag{A69}$$

$$\kappa_A \equiv \frac{1}{2}((\kappa_1 - 1)\chi_1^2 - (\kappa_2 - 1)\chi_2^2), \tag{A70}$$

where κ_1 and κ_2 are the spin quadrupole constants, which equal 1 for black holes.

The relative angular velocity $\dot{\phi}^{\text{NS}}$ of the spin-aligned eccentric BBH can be expressed as

$$\dot{\phi}^{\text{SP}} = \dot{\phi}^{\text{NS}} + \dot{\phi}^{\text{SO}} + \dot{\phi}^{\text{SS}}, \tag{A71}$$

where the spin-orbit coupling component $\dot{\phi}^{\text{SO}}$ can be expressed as

$$\dot{\phi}^{\text{SO}} = \dot{\phi}_{1.5\text{PN}}^{\text{SO}} + \dot{\phi}_{2.5\text{PN}}^{\text{SO}}, \tag{A72}$$

$$\dot{\phi}_{1.5\text{PN}}^{\text{SO}} = \frac{2e_t x^3 (\delta\chi_A + \chi_S) (e_t - \cos u)}{(1-e_t^2)(1-e_t \cos u)^3}, \tag{A73}$$

$$\begin{aligned}
\dot{\phi}_{2.5\text{PN}}^{\text{SO}} = & \frac{x^4}{6(1-e_t^2)^2(-1+e_t \cos u)^5} \left[-\delta(e_t^4(36-54\eta) - 24(-3+\eta) + 6e_t^6(-2+\eta) + e_t^2(56+31\eta)) \chi_A \right. \\
& + (-12(6-8\eta+\eta^2) + 6e_t^6(2-3\eta+2\eta^2) - 6e_t^4(6-27\eta+8\eta^2) + e_t^2(-56-57\eta+50\eta^2)) \chi_S \\
& - e_t [\delta(-224+44\eta+6e_t^4(-6+11\eta) + e_t^2(-196+13\eta)) \chi_A + (-4(56-60\eta+\eta^2) \\
& - 6e_t^4(6-23\eta+4\eta^2) + e_t^2(-196+171\eta+34\eta^2)) \chi_S] \cos u + e_t^2 [\delta(8(-29+5\eta) + 6e_t^4(-6+5\eta) \\
& + e_t^2(-188+53\eta)) \chi_A + (-4(58-81\eta+2\eta^2) - 6e_t^4(6-5\eta+2\eta^2) + e_t^2(-188+195\eta+26\eta^2)) \chi_S] \cos^2 u \\
& - e_t^3 [\delta(-68+14\eta+3e_t^2(-28+9\eta)) \chi_A + (-68+162\eta-4\eta^2+3e_t^2(-28+7\eta+2\eta^2)) \chi_S] \cos^3 u \\
& \left. - 12\sqrt{1-e_t^2} [2\delta(-3+\eta)\chi_A - (6-8\eta+\eta^2)\chi_S] (1-e_t \cos u)^2 (1-2e_t^2+e_t \cos u) \right]. \tag{A74}
\end{aligned}$$

And the spin-spin coupling component $\dot{\phi}^{\text{SS}}$ can be expressed as

$$\dot{\phi}^{\text{SS}} = \dot{\phi}_{2\text{PN}}^{\text{SS}} + \dot{\phi}_{3\text{PN}}^{\text{SS}}, \tag{A75}$$

$$\dot{\phi}_{2\text{PN}}^{\text{SS}} = \frac{e_t x^{7/2} (\kappa_S - 2\kappa_S \eta + \chi_A^2 - 4\eta \chi_A^2 + \chi_S^2 + \delta(\kappa_A + 2\chi_A \chi_S)) (e_t - \cos u)}{(1-e_t^2)^{3/2} (-1+e_t \cos u)^3}, \tag{A76}$$

$$\begin{aligned}
\dot{\phi}_{3\text{PN}}^{\text{SS}} = & \frac{x^4}{12(1-e_t^2)^3(1-e_t \cos u)^5} \left(6\sqrt{x}(-1+e_t^2) [\delta\kappa_A(-14+5\eta) + \kappa_S(-14+33\eta-6\eta^2) + 4\delta(-11+9\eta)\chi_A \chi_S \right. \\
& \left. - 2((11-46\eta+6\eta^2)\chi_A^2 + (11-16\eta+4\eta^2)\chi_S^2)] (1-e_t \cos u)^2 (1-2e_t^2+e_t \cos u) \right. \\
& \left. - 24\sqrt{x-e_t^2 x} (1-e_t \cos u)^2 \left[-(1+4e_t^2+3e_t^4)(-1+4\eta)\chi_A^2 + 2\delta(1+e_t^4(3-6\eta) - e_t^2(-4+\eta) + \eta)\chi_A \chi_S \right. \right. \\
& \left. \left. + ((1+\eta)^2 + 3e_t^4(1-4\eta+3\eta^2) - 2e_t^2(-2+\eta+3\eta^2)) \chi_S^2 \right. \right. \\
& \left. \left. + e_t(-1+3e_t^2) [(1+3e_t^2)(-1+4\eta)\chi_A^2 + 2\delta(-1+3e_t^2(-1+\eta))\chi_A \chi_S - (1+3e_t^2(-1+\eta) - \eta)(-1+\eta)\chi_S^2] \cos u \right] \right. \\
& \left. + \sqrt{x-e_t^2 x} \left[-84\kappa_S - 114e_t^2\kappa_S - 72e_t^4\kappa_S + 24e_t^6\kappa_S + 198\kappa_S \eta + 311e_t^2\kappa_S \eta + 160e_t^4\kappa_S \eta - 48e_t^6\kappa_S \eta - 36\kappa_S \eta^2 \right. \right. \\
& \left. \left. + 38e_t^2\kappa_S \eta^2 - 128e_t^4\kappa_S \eta^2 + 24e_t^6\kappa_S \eta^2 + \delta\kappa_A(-84+24e_t^6+30\eta+8e_t^4(-9+2\eta) + e_t^2(-114+83\eta)) - 108\chi_A^2 \right. \right. \\
& \left. \left. - 138e_t^2\chi_A^2 + 24e_t^6\chi_A^2 + 456\eta\chi_A^2 + 512e_t^2\eta\chi_A^2 + 112e_t^4\eta\chi_A^2 - 120e_t^6\eta\chi_A^2 - 72\eta^2\chi_A^2 + 76e_t^2\eta^2\chi_A^2 - 256e_t^4\eta^2\chi_A^2 \right. \right. \\
& \left. \left. + 48e_t^6\eta^2\chi_A^2 + 4\delta[-54+e_t^6(12-24\eta) + e_t^2(-69+\eta) + 66\eta+56e_t^4\eta] \chi_A \chi_S - 108\chi_S^2 - 138e_t^2\chi_S^2 + 24e_t^6\chi_S^2 \right. \right. \\
& \left. \left. + 240\eta\chi_S^2 + 44e_t^2\eta\chi_S^2 + 112e_t^4\eta\chi_S^2 - 72e_t^6\eta\chi_S^2 - 24\eta^2\chi_S^2 - 96e_t^2\eta^2\chi_S^2 + 72e_t^4\eta^2\chi_S^2 \right. \right. \\
& \left. \left. - e_t \left[-\kappa_S(300-740\eta+64\eta^2+2e_t^4(36-97\eta+74\eta^2) + e_t^2(366-929\eta+94\eta^2)) + \delta[\kappa_A(20(-15+7\eta) \right. \right. \right. \\
& \left. \left. + e_t^4(-72+50\eta) + e_t^2(-366+197\eta)) + 4(-258+e_t^4(144-167\eta) + 211\eta+e_t^2(-219+253\eta))\chi_A \chi_S \right] \right. \\
& \left. - 2[(258-1057\eta+64\eta^2+e_t^2(219-910\eta+94\eta^2) + e_t^4(-144+527\eta+148\eta^2))\chi_A^2 \right. \\
& \left. \left. + (258-397\eta+36\eta^2+e_t^4(-144+383\eta-252\eta^2) + e_t^2(219-472\eta+288\eta^2))\chi_S^2] \cos u \right. \right. \\
& \left. \left. + e_t^2 \left[-\kappa_S(348-868\eta+56\eta^2+2e_t^4(36-89\eta+46\eta^2) + e_t^2(318-817\eta+158\eta^2)) \right. \right. \right. \\
& \left. \left. \left. + \delta[\kappa_A(e_t^4(-72+34\eta) + 4(-87+43\eta) + e_t^2(-318+181\eta)) + 4(-354+e_t^4(216-259\eta) + 323\eta \right. \right. \right.
\end{aligned}$$

$$\begin{aligned}
& + e_t^2(-195 + 233\eta)\chi_A\chi_S \Big] - 2 \Big[(354 - 1457\eta + 56\eta^2 + e_t^4(-216 + 835\eta + 92\eta^2) + e_t^2(195 - 818\eta + 158\eta^2))\chi_A^2 \\
& + (354 - 605\eta + 108\eta^2 + e_t^4(-216 + 547\eta - 324\eta^2) + e_t^2(195 - 428\eta + 288\eta^2))\chi_S^2 \Big] \cos u^2 \\
& + e_t^3 \Big[\kappa_S(108 - 278\eta + 4\eta^2 + e_t^2(138 - 343\eta + 98\eta^2)) + \delta \Big[\kappa_A(108 + e_t^2(138 - 67\eta) - 62\eta) + 4(138 + e_t^2(81 - 53\eta) \\
& + 108e_t^4(-1 + \eta) - 154\eta)\chi_A\chi_S \Big] + 2 \Big[(138 - 568\eta + 4\eta^2 + 108e_t^4(-1 + 4\eta) + e_t^2(81 - 344\eta + 98\eta^2))\chi_A^2 \\
& + (138 - 108e_t^4(-1 + \eta)^2 - 292\eta + 84\eta^2 + e_t^2(81 - 86\eta + 48\eta^2))\chi_S^2 \Big] \cos u^3 \Big] \Big). \tag{A77}
\end{aligned}$$

The mean anomaly l^{SP} of the spin-aligned eccentric BBH can be expressed as

$$l^{\text{SP}} = l^{\text{NS}} + l^{\text{SO}} + l^{\text{SS}}, \tag{A78}$$

where the spin-orbit coupling component l^{SO} can be expressed as

$$\begin{aligned}
l^{\text{SO}} & = l_{2.5\text{PN}}^{\text{SO}} \\
& = \frac{x^{5/2}}{2(1 - e_t^2)} \Big[8u\delta(-3 + \eta)\chi_A - 4u(6 - 8\eta + \eta^2)\chi_S \\
& \quad - 8 \left(2\delta(-3 + \eta)\chi_A - (6 - 8\eta + \eta^2)\chi_S \right) \left(-\tan^{-1} \left(\frac{\sin(u)\beta_\phi}{1 - \cos(u)\beta_\phi} \right) + u \right) \\
& \quad + e_t \left(\delta(4 + \eta)\chi_A + (4 - 3\eta - 2\eta^2)\chi_S \right) \sin \left(2 \left(-\tan^{-1} \left(\frac{\sin(u)\beta_\phi}{1 - \cos(u)\beta_\phi} \right) + u \right) \right) \Big], \tag{A79}
\end{aligned}$$

and the spin-spin coupling component l^{SS} can be expressed as

$$\begin{aligned}
l^{\text{SS}} & = l_{3\text{PN}}^{\text{SS}} \\
& = \frac{x^3}{4(1 - e_t^2)^{3/2}} \Big[2u \left(-14\kappa_S + 33\kappa_S\eta - 6\kappa_S\eta^2 + \delta\kappa_A(-14 + 5\eta) - 22\chi_A^2 + 92\eta\chi_A^2 - 12\eta^2\chi_A^2 \right. \\
& \quad + 4\delta(-11 + 9\eta)\chi_A\chi_S - 22\chi_S^2 + 32\eta\chi_S^2 - 8\eta^2\chi_S^2 \Big) + 4 \left(\delta\kappa_A(14 - 5\eta) + \kappa_S(14 - 33\eta + 6\eta^2) \right. \\
& \quad + 22\chi_A^2 - 92\eta\chi_A^2 + 12\eta^2\chi_A^2 + 4\delta(11 - 9\eta)\chi_A\chi_S + 22\chi_S^2 - 32\eta\chi_S^2 + 8\eta^2\chi_S^2 \Big) \left(-\tan^{-1} \left(\frac{\sin(u)\beta_\phi}{1 - \cos(u)\beta_\phi} \right) + u \right) \\
& \quad + e_t \left(\delta\kappa_A(8 - 3\eta) + \kappa_S(8 - 19\eta + 2\eta^2) + 8\chi_A^2 - 31\eta\chi_A^2 + 4\eta^2\chi_A^2 + 2\delta(8 - 7\eta)\chi_A\chi_S + 8\chi_S^2 \right. \\
& \quad \left. - 15\eta\chi_S^2 \right) \sin \left(2 \left(-\tan^{-1} \left(\frac{\sin(u)\beta_\phi}{1 - \cos(u)\beta_\phi} \right) + u \right) \right) \Big], \tag{A80}
\end{aligned}$$

where the expression for β_ϕ is provided in Eq. (A14). Furthermore, in Eqs. (A79) and (A80), we have refined the equations based on the guidelines outlined in Ref. [24], effectively mitigating the issue of local divergence during waveform computation.

The mean motion n^{SP} of the spin-aligned eccentric BBH can be expressed as

$$n^{\text{SP}} = n^{\text{NS}} + n^{\text{SO}} + n^{\text{SS}}, \tag{A81}$$

where the spin-orbit coupling component n^{SO} can be expressed as

$$n^{\text{SO}} = n_{1.5\text{PN}}^{\text{SO}} + n_{2.5\text{PN}}^{\text{SO}}, \tag{A82}$$

$$n_{1.5\text{PN}}^{\text{SO}} = \frac{2x^3(2\delta\chi_A - (-2 + \eta)\chi_S)}{(1 - e_t^2)^{3/2}}, \tag{A83}$$

$$n_{2.5\text{PN}}^{\text{SO}} = -\frac{x^4(\delta(-20 + 17\eta + 4e_t^2(-15 + 7\eta))\chi_A - (20 - 57\eta + 4\eta^2 + 2e_t^2(30 - 29\eta + 7\eta^2))\chi_S)}{2(1 - e_t^2)^{5/2}}. \tag{A84}$$

And the spin-spin coupling component n^{SS} can be expressed as

$$n^{\text{SS}} = n_{2\text{PN}}^{\text{SS}} + n_{3\text{PN}}^{\text{SS}}, \quad (\text{A85})$$

$$n_{2\text{PN}}^{\text{SS}} = -\frac{3x^{7/2} (\kappa_S - 2\kappa_S\eta + \chi_A^2 - 4\eta\chi_A^2 + \chi_S^2 + \delta(\kappa_A + 2\chi_A\chi_S))}{2(1 - e_t^2)^2}, \quad (\text{A86})$$

$$\begin{aligned} n_{3\text{PN}}^{\text{SS}} = & \frac{x^{9/2}}{4(1 - e_t^2)^3} (\kappa_S (42 - 118\eta + 20\eta^2 + e_t^2(78 - 191\eta + 58\eta^2)) + \delta(\kappa_A (42 + e_t^2(78 - 35\eta) - 34\eta) \\ & + 4(17 + e_t^2(51 - 25\eta) - 39\eta)\chi_A\chi_S) + 2((17 - 79\eta + 20\eta^2 + e_t^2(51 - 220\eta + 58\eta^2))\chi_A^2 \\ & + (17 + e_t^2(51 - 34\eta) - 67\eta + 20\eta^2)\chi_S^2)). \end{aligned} \quad (\text{A87})$$

The radiative dynamics up to the 3PN order under the harmonic coordinate system for spin-aligned BBH utilized in this study are derived from Ref. [89], covering instantaneous and hereditary contributions described in relation to PN expansion parameters x and temporal eccentricity e_t . These components can be represented as the combination of the nonspinning portion, spin-orbit coupling, and spin-spin coupling, given by

$$\dot{x}^{\text{SP}} = \dot{x}^{\text{NS}} + \dot{x}^{\text{SO}} + \dot{x}^{\text{SS}}, \quad (\text{A88})$$

and

$$\dot{e}_t^{\text{SP}} = \dot{e}_t^{\text{NS}} + \dot{e}_t^{\text{SO}} + \dot{e}_t^{\text{SS}}. \quad (\text{A89})$$

They can be further partitioned into instantaneous and hereditary constituents as follows:

$$\dot{x}^{\text{SO}} = \dot{x}_{\text{inst}}^{\text{SO}} + \dot{x}_{\text{hered}}^{\text{SO}}, \quad (\text{A90})$$

$$\dot{x}^{\text{SS}} = \dot{x}_{\text{inst}}^{\text{SS}}, \quad (\text{A91})$$

$$\dot{e}_t^{\text{SO}} = \dot{e}_{t\text{inst}}^{\text{SO}} + \dot{e}_{t\text{hered}}^{\text{SO}}, \quad (\text{A92})$$

$$\dot{e}_t^{\text{SS}} = \dot{e}_{t\text{inst}}^{\text{SS}}. \quad (\text{A93})$$

It is worth mentioning that the hereditary term of spin-spin coupling comes from beyond the 3PN order, so it is absent here. The specific expressions of the PN order of the above equations are

$$\dot{x}_{\text{inst}}^{\text{SO}} = \dot{x}_{1.5\text{PN}}^{\text{SO}} + \dot{x}_{2.5\text{PN}}^{\text{SO}}, \quad (\text{A94})$$

$$\begin{aligned} \dot{x}_{1.5\text{PN}}^{\text{SO}} = & \frac{x^{13/2}\eta}{45(-1 + e_t^2)^5 M} ((5424 + 27608e_t^2 + 16694e_t^4 + 585e^6)\delta\chi_A + (5424 + e_t^4(16694 - 4072\eta) \\ & - 3648\eta + 9e_t^6(65 + 8\eta) - 8e_t^2(-3451 + 1670\eta))\chi_S), \end{aligned} \quad (\text{A95})$$

$$\begin{aligned} \dot{x}_{2.5\text{PN}}^{\text{SO}} = & \frac{x^{15/2}\eta}{10080(1 - e_t^2)^6 M} (\delta(45e_t^8(-17967 + 14560\eta) + 128(-31319 + 48678\eta) + 224e_t^4(-505492 + 493737\eta) \\ & + 128e_t^2(-334209 + 496090\eta) + 16e_t^6(-2581907 + 2083557\eta))\chi_A + (45e_t^8(-17967 + 12924\eta + 1792\eta^2) \\ & - 128(31319 - 91900\eta + 26544\eta^2) - 448e_t^4(252746 - 403471\eta + 98766\eta^2) \\ & - 128e_t^2(334209 - 828514\eta + 266042\eta^2) - 16e_t^6(2581907 - 2894533\eta \\ & + 469140\eta^2))\chi_S + 896e_t^2\sqrt{1 - e_t^2}(4376 + 4458e_t^2 + 91e_t^4)(2\delta(-3 + \eta)\chi_A - (6 - 8\eta + \eta^2)\chi_S)), \end{aligned} \quad (\text{A96})$$

$$\dot{x}_{\text{hered}}^{\text{SO}} = \dot{x}_{3\text{PN}}^{\text{SO}}, \quad (\text{A97})$$

$$\begin{aligned} \dot{x}_{3\text{PN}}^{\text{SO}} = & -\frac{\pi x^8 \eta}{103680(1-e_t^2)^{13/2} M} \left((49766400 + 528887808e_t^2 + 814424832e_t^4 + 213166272e_t^6 + 3911917e_t^8) \delta\chi_A \right. \\ & + (-221184(-225 + 148\eta) - 18432e_t^2(-28694 + 13789\eta) - 2304e_t^4(-353483 + 101614\eta) \\ & \left. - 96e_t^6(-2220482 + 214925\eta) + e_t^8(3911917 + 1055680\eta) \right) \chi_S, \end{aligned} \quad (\text{A98})$$

$$\dot{x}_{\text{inst}}^{\text{SS}} = \dot{x}_{2\text{PN}}^{\text{SS}} + \dot{x}_{3\text{PN}}^{\text{SS}}, \quad (\text{A99})$$

$$\begin{aligned} \dot{x}_{2\text{PN}}^{\text{SS}} = & \frac{x^7 \eta}{60(1-e_t^2)^{11/2} M} \left(4(960 + 5384e_t^2 + 3736e_t^4 + 177e_t^6) \delta\kappa_A - 4(960 + 5384e_t^2 + 3736e_t^4 + 177e_t^6) \kappa_S (-1 + 2\eta) \right. \\ & + 3888\chi_A^2 + 21992e_t^2\chi_A^2 + 15358e_t^4\chi_A^2 + 735e_t^6\chi_A^2 - 15360\eta\chi_A^2 - 86144e_t^2\eta\chi_A^2 - 59776e_t^4\eta\chi_A^2 - 2832e_t^6\eta\chi_A^2 \\ & + 2(3888 + 21992e_t^2 + 15358e_t^4 + 735e_t^6) \delta\chi_A\chi_S + 3888\chi_S^2 + 21992e_t^2\chi_S^2 + 15358e_t^4\chi_S^2 + 735e_t^6\chi_S^2 - 192\eta\chi_S^2 \\ & \left. - 1824e_t^2\eta\chi_S^2 - 1656e_t^4\eta\chi_S^2 - 108e_t^6\eta\chi_S^2 \right), \end{aligned} \quad (\text{A100})$$

$$\begin{aligned} \dot{x}_{3\text{PN}}^{\text{SS}} = & \frac{x^8 \eta}{30240M} \left(\frac{1}{(1-e_t^2)^{13/2}} \left(6\kappa_S (192(8963 - 31632\eta + 14784\eta^2) + 224e_t^2(70203 - 254204\eta + 160324\eta^2) \right. \right. \\ & + 3e_t^8(164778 - 456935\eta + 251104\eta^2) + 28e_t^6(624771 - 1759522\eta + 937088\eta^2) + 8e_t^4(5381787 \\ & - 16375838\eta + 9140320\eta^2) \left. \right) + 32150592\chi_A^2 + 236283488e_t^2\chi_A^2 + 439738616e_t^4\chi_A^2 + 141676164e_t^6\chi_A^2 \\ & + 3374811e_t^8\chi_A^2 - 139984704\eta\chi_A^2 - 1054958240e_t^2\eta\chi_A^2 - 1959961928e_t^4\eta\chi_A^2 - 633764796e_t^6\eta\chi_A^2 \\ & - 15271560e_t^8\eta\chi_A^2 + 34062336\eta^2\chi_A^2 + 430950912e_t^2\eta^2\chi_A^2 + 877470720e_t^4\eta^2\chi_A^2 + 314861568e_t^6\eta^2\chi_A^2 \\ & + 9039744e_t^8\eta^2\chi_A^2 + 32150592\chi_S^2 + 236283488e_t^2\chi_S^2 + 439738616e_t^4\chi_S^2 + 141676164e_t^6\chi_S^2 \\ & + 3374811e_t^8\chi_S^2 - 67507776\eta\chi_S^2 - 389245472e_t^2\eta\chi_S^2 - 507132584e_t^4\eta\chi_S^2 - 121365132e_t^6\eta\chi_S^2 \\ & - 2752848e_t^8\eta\chi_S^2 + 19272960\eta^2\chi_S^2 + 71582336e_t^2\eta^2\chi_S^2 + 57059744e_t^4\eta^2\chi_S^2 + 9706032e_t^6\eta^2\chi_S^2 \\ & + 344736e_t^8\eta^2\chi_S^2 - 2\delta(3\kappa_A(192(-8963 + 13706\eta) + 224e_t^2(-70203 + 113798\eta) + e_t^8(-494334 \\ & + 382137\eta) + 28e_t^6(-624771 + 509980\eta) + 8e_t^4(-5381787 + 5612264\eta)) + (576(-55817 + 68481\eta) \\ & + 9e_t^8(-374979 + 251398\eta) + 224e_t^2(-1054837 + 1113995\eta) + 84e_t^6(-1686621 + 1121579\eta) \\ & + 8e_t^4(-54967327 + 44258753\eta)) \chi_A\chi_S) - \frac{672(-96 + 4484e_t^2 + 4530e_t^4 + 7e_t^6)}{(1-e_t^2)^6} (\delta\kappa_A(-14 + 5\eta) \\ & \left. + \kappa_S(-14 + 33\eta - 6\eta^2) + 4\delta(-11 + 9\eta)\chi_A\chi_S - 2((11 - 46\eta + 6\eta^2)\chi_A^2 + (11 - 16\eta + 4\eta^2)\chi_S^2) \right), \end{aligned} \quad (\text{A101})$$

$$\dot{e}_{\text{inst}}^{\text{SO}} = \dot{e}_{1.5\text{PN}}^{\text{SO}} + \dot{e}_{2.5\text{PN}}^{\text{SO}}, \quad (\text{A102})$$

$$\begin{aligned} \dot{e}_{1.5\text{PN}}^{\text{SO}} = & \frac{e_t x^{11/2} \eta}{90(1-e_t^2)^4 M} \left((19688 + 28256e_t^2 + 2367e_t^4) \delta\chi_A \right. \\ & \left. + (19688 + e_t^2(28256 - 7972\eta) - 13312\eta + 3e_t^4(789 + 92\eta)) \chi_S \right), \end{aligned} \quad (\text{A103})$$

$$\begin{aligned} \dot{e}_{2.5\text{PN}}^{\text{SO}} = & \frac{e_t x^{13/2} \eta}{60480M} \left(-\frac{2688(2960 + 6927e_t^2 + 313e_t^4) (2\delta(-3 + \eta)\chi_A - (6 - 8\eta + \eta^2)\chi_S)}{(1-e_t^2)^{9/2}} \right. \\ & + \frac{1}{(-1+e_t^2)^5} \left(\delta(9e_t^6(-1037433 + 955808\eta) + 64(-324747 + 1197434\eta) + 56e_t^4(-4389075 \right. \\ & + 3676346\eta) + 48e_t^2(-6885449 + 7330106\eta)) \chi_A + (3e_t^6(-3112299 + 2662908\eta + 336896\eta^2) \\ & - 64(324747 - 1788860\eta + 740824\eta^2) - 48e_t^2(6885449 - 12914742\eta + 3551324\eta^2) \\ & \left. \left. - 8e_t^4(30723525 - 36750368\eta + 6313216\eta^2) \right) \chi_S \right), \end{aligned} \quad (\text{A104})$$

$$\dot{e}_{\text{thered}}^{\text{SO}} = \dot{e}_{\text{3PN}}^{\text{SO}}, \quad (\text{A105})$$

$$\begin{aligned} \dot{e}_{\text{3PN}}^{\text{SO}} = & \frac{e\pi x^7 \eta}{51840(1 - e_t^2)^{11/2} M} \left((64622592 + 238783104e_t^2 + 96887280e_t^4 + 2313613e_t^6) \delta\chi_A + (-9216(-7012 + 4937\eta) \right. \\ & \left. - 1152e_t^2(-207277 + 74954\eta) - 48e_t^4(-2018485 + 95561\eta) + e_t^6(2313613 + 1263046\eta)) \chi_S \right), \end{aligned} \quad (\text{A106})$$

$$\dot{e}_{\text{inst}}^{\text{SS}} = \dot{e}_{\text{2PN}}^{\text{SS}} + \dot{e}_{\text{3PN}}^{\text{SS}}, \quad (\text{A107})$$

$$\begin{aligned} \dot{e}_{\text{2PN}}^{\text{SS}} = & - \frac{e_t x^6 \eta}{120(1 - e_t^2)^{9/2} M} \left(4(3752 + 5950e_t^2 + 555e_t^4) \delta\kappa_A - 4(3752 + 5950e_t^2 + 555e_t^4) \kappa_S (-1 + 2\eta) \right. \\ & + 15368\chi_A^2 + 24340e_t^2\chi_A^2 + 2265e_t^4\chi_A^2 - 60032\eta\chi_A^2 - 95200e_t^2\eta\chi_A^2 - 8880e_t^4\eta\chi_A^2 + 2(15368 + 24340e_t^2 \\ & \left. + 2265e_t^4) \delta\chi_A\chi_S + 15368\chi_S^2 + 24340e_t^2\chi_S^2 + 2265e_t^4\chi_S^2 - 1440\eta\chi_S^2 - 2160e_t^2\eta\chi_S^2 - 180e_t^4\eta\chi_S^2 \right), \end{aligned} \quad (\text{A108})$$

$$\begin{aligned} \dot{e}_{\text{3PN}}^{\text{SS}} = & \frac{e_t x^7 \eta}{60480M} \left(- \frac{1}{(1 - e_t^2)^{11/2}} \left(6\kappa_S (9e_t^6(184470 - 516661\eta + 288288\eta^2) + 32(89793 - 527402\eta + 404908\eta^2) \right. \right. \\ & + 48e_t^2(847619 - 2691660\eta + 1530550\eta^2) + 4e_t^4(8317317 - 23483168\eta + 12461848\eta^2)) + 88499360\chi_A^2 \\ & + 477482624e_t^2\chi_A^2 + 275826708e_t^4\chi_A^2 + 11414979e_t^6\chi_A^2 - 399608096\eta\chi_A^2 - 2115049424e_t^2\eta\chi_A^2 \\ & - 1236732852e_t^4\eta\chi_A^2 - 52550856e_t^6\eta\chi_A^2 + 155484672\eta^2\chi_A^2 + 881596800e_t^2\eta^2\chi_A^2 + 598168704e_t^4\eta^2\chi_A^2 \\ & + 31135104e_t^6\eta^2\chi_A^2 + 88499360\chi_S^2 + 477482624e_t^2\chi_S^2 + 275826708e_t^4\chi_S^2 + 11414979e_t^6\chi_S^2 \\ & - 219613856\eta\chi_S^2 - 624223376e_t^2\eta\chi_S^2 - 235260900e_t^4\eta\chi_S^2 - 8905680e_t^6\eta\chi_S^2 + 58808960\eta^2\chi_S^2 \\ & + 83203904e_t^2\eta^2\chi_S^2 + 15245328e_t^4\eta^2\chi_S^2 + 707616e_t^6\eta^2\chi_S^2 - 2\delta(3\kappa_A(9e_t^6(-184470 + 147721\eta) \\ & + 32(-89793 + 347816\eta) + 48e_t^2(-847619 + 996422\eta) + 4e_t^4(-8317317 + 6848534\eta)) \\ & + (27e_t^6(-422777 + 292530\eta) + 32(-2765605 + 4144133\eta) + 12e_t^4(-22985559 + 15361955\eta) \\ & + 16e_t^2(-29842664 + 25916947\eta)) \chi_A\chi_S) - \frac{672(3248 + 6891e_t^2 + 61e_t^4)}{(1 - e_t^2)^5} (\delta\kappa_A(-14 + 5\eta) \\ & \left. \left. + \kappa_S(-14 + 33\eta - 6\eta^2) + 4\delta(-11 + 9\eta)\chi_A\chi_S - 2((11 - 46\eta + 6\eta^2)\chi_A^2 + (11 - 16\eta + 4\eta^2)\chi_S^2) \right) \right). \end{aligned} \quad (\text{A109})$$

The 22 mode of the gravitational waveform $h^{22,\text{SP}}$ for the spin-aligned eccentric BBH system, as provided in Ref. [89], can be expressed as

$$h^{22,\text{SP}} = \frac{4GM\eta}{c^4 R} \sqrt{\frac{\pi}{5}} e^{-2i\phi} H^{22,\text{SP}}, \quad (\text{A110})$$

where the amplitude $H^{22,\text{SP}}$ can be expressed as

$$H^{22,\text{SP}} = H^{22,\text{NS}} + H^{22,\text{SO}} + H^{22,\text{SS}}, \quad (\text{A111})$$

where $H^{22,\text{NS}}$ is the nonspinning portion of the aforementioned waveform. And the specific expressions of $H^{22,\text{SO}}$ and $H^{22,\text{SS}}$ are

$$H^{22,\text{SO}} = H_{1.5\text{PN}}^{22,\text{SO}} + H_{2.5\text{PN}}^{22,\text{SO}} + H_{3\text{PN}}^{22,\text{SO}}, \quad (\text{A112})$$

$$H_{1.5\text{PN}}^{22,\text{SO}} = \frac{1}{c^3} \frac{2M^2}{3r^2} \left(-i\dot{r} (3\delta\chi_A + (3 - 8\eta)\chi_S) + r\dot{\phi} (-3\delta\chi_A + (-3 + 5\eta)\chi_S) \right), \quad (\text{A113})$$

$$\begin{aligned} H_{2.5\text{PN}}^{22,\text{SO}} = & \frac{1}{c^5} \frac{M^2}{42r^3} \left(-8iM\dot{r} (\delta(-55 + 19\eta)\chi_A + (-55 + 100\eta - 86\eta^2)\chi_S) + 2ir\dot{r}^3 (3\delta(-9 + 14\eta)\chi_A \right. \\ & + (-27 + 30\eta - 4\eta^2)\chi_S) - r^4\dot{\phi}^3 (\delta(120 + 83\eta)\chi_A + 3(40 - 161\eta + 78\eta^2)\chi_S) \\ & + r^2\dot{r}^2\dot{\phi} (\delta(18 + 275\eta)\chi_A + (18 - 315\eta + 188\eta^2)\chi_S) - 2ir^3\dot{r}\dot{\phi}^2 (\delta(51 + 62\eta)\chi_A \\ & \left. + (51 - 264\eta + 440\eta^2)\chi_S) + Mr\dot{\phi} (\delta(238 - 141\eta)\chi_A + (238 - 181\eta + 474\eta^2)\chi_S) \right), \end{aligned} \quad (\text{A114})$$

$$H_{3\text{PN}}^{22,\text{SO}} = -\frac{1}{c^6} \frac{iM^3(M + r(2\dot{r}^2 - 10ir\dot{r}\dot{\phi} + 7r^2\dot{\phi}^2))(\delta\chi_A + \chi_S - 2\eta\chi_S)}{3r^4}, \quad (\text{A115})$$

$$H^{22,\text{SS}} = H_{2\text{PN}}^{22,\text{SS}} + H_{3\text{PN}}^{22,\text{SS}}, \quad (\text{A116})$$

$$H_{2\text{PN}}^{22,\text{SS}} = \frac{1}{c^4} \frac{3M^3(\kappa_S - 2\kappa_S\eta + \chi_A^2 - 4\eta\chi_A^2 + \chi_S^2 + \delta(\kappa_A + 2\chi_A\chi_S))}{2r^3} \quad (\text{A117})$$

$$\begin{aligned} H_{3\text{PN}}^{22,\text{SS}} = & -\frac{1}{c^6} \frac{M^3}{84r^4} (2M(\delta\kappa_A(438 + 103\eta) + \kappa_S(438 - 773\eta + 108\eta^2) + 2(219 - 863\eta + 108\eta^2)\chi_A^2 \\ & + 2\delta(438 + 145\eta)\chi_A\chi_S + 6(73 + 44\eta - 28\eta^2)\chi_S^2) + r(-r^2\dot{\phi}^2(\delta\kappa_A(153 + 430\eta) + \kappa_S(153 \\ & + 124\eta - 804\eta^2) + 153\chi_A^2 - 28\eta\chi_A^2 - 1608\eta^2\chi_A^2 + 2\delta(153 + 38\eta)\chi_A\chi_S + 153\chi_S^2 - 508\eta\chi_S^2 \\ & - 112\eta^2\chi_S^2) - 2ir\dot{r}\dot{\phi}(\delta\kappa_A(117 + 211\eta) + \kappa_S(117 - 23\eta - 390\eta^2) + 117\chi_A^2 - 439\eta\chi_A^2 \\ & - 780\eta^2\chi_A^2 + 2\delta(117 - 223\eta)\chi_A\chi_S + 117\chi_S^2 - 475\eta\chi_S^2 + 56\eta^2\chi_S^2) + \dot{r}^2(\delta\kappa_A(291 - 308\eta) \\ & + \kappa_S(291 - 890\eta + 24\eta^2) + 291\chi_A^2 - 940\eta\chi_A^2 + 48\eta^2\chi_A^2 + 2\delta(291 - 364\eta)\chi_A\chi_S + 291\chi_S^2 \\ & - 952\eta\chi_S^2 + 224\eta^2\chi_S^2)). \end{aligned} \quad (\text{A118})$$

The high-order harmonic mode for spin-aligned BBH can be expressed as

$$h^{\ell m, \text{SP}} = \frac{4GM\eta}{c^4 R} \sqrt{\frac{\pi}{5}} e^{-im\phi} H^{\ell m, \text{SP}}. \quad (\text{A119})$$

At the leading PN order PN order, the magnitudes of the high-order modes 21, 33, 32, 44, 43, and 55 in spin-aligned BBH closely resemble those in the nonspinning scenario. For a more detailed representation at higher PN orders in the context of complete spin alignment, readers can consult Ref. [89].

3. Initial eccentricity estimate

The technique employed to quantify the nonspinning eccentricity originates from the third PN precise generalized quasi-Keplerian parametrization for compact binaries moving in eccentric orbits under harmonic coordinates [75], characterized by the expression:

$$\begin{aligned} e_{t0\text{KP}}^2 = & 1 + 2E_0h_0^2 + \frac{(-2E_0)}{4c^2} \left\{ -8 + 8\eta - (-2E_0h_0^2)(-17 + 7\eta) \right\} + \frac{(-2E_0)^2}{8c^4} \left\{ 12 + 72\eta + 20\eta^2 \right. \\ & \left. - 24\sqrt{(-2E_0h_0^2)}(-5 + 2\eta) - (-2E_0h_0^2)(112 - 47\eta + 16\eta^2) - \frac{16}{(-2E_0h_0^2)}(-4 + 7\eta) + \frac{24}{\sqrt{(-2E_0h_0^2)}}(-5 + 2\eta) \right\} \\ & + \frac{(-2E_0)^3}{6720c^6} \left\{ 23520 - 464800\eta + 179760\eta^2 + 16800\eta^3 - 2520\sqrt{(-2E_0h_0^2)}(265 - 193\eta + 46\eta^2) \right. \\ & \left. - 525(-2E_0h_0^2)(-528 + 200\eta - 77\eta^2 + 24\eta^3) - \frac{6}{(-2E_0h_0^2)}(73920 - 260272\eta + 4305\pi^2\eta + 61040\eta^2) \right. \\ & \left. + \frac{70}{\sqrt{(-2E_0h_0^2)}}(16380 - 19964\eta + 123\pi^2\eta + 3240\eta^2) + \frac{8}{(-2E_0h_0^2)^2}(53760 - 176024\eta + 4305\pi^2\eta \right. \\ & \left. + 15120\eta^2) - \frac{70}{(-2E_0h_0^2)^{3/2}}(10080 - 13952\eta + 123\pi^2\eta + 1440\eta^2) \right\} \end{aligned} \quad (\text{A120})$$

where we introduce E_0 and h_0 , defined as $E_0 = E_b/\eta$ and $h_0 = L/\eta$, where E_b represents the orbital binding energy, as defined by Eq. (65), and L denotes the orbital angular momentum. All relevant data for numerical relativity simulations can be accessed from the RIT and SXS catalogs.

In the context of spin-aligned configurations, we employ the quasi-Keplerian parameterization method at the 2PN order to determine eccentricity in ADM coordinates referring to Ref. [77], represented as:

$$\begin{aligned}
e_t^2 = & 1 - 2h_0^2|E_0| + |E_0| (h_0^2|E_0|(17 - 7\eta) + 4(\eta - 1)) \\
& + \frac{\delta}{h_0}|E_0| \left[2(\eta - 2) (\chi_1 + \chi_2) - 4\sqrt{1 - 4\eta} (\chi_1 - \chi_2) \right] \\
& + \frac{\delta^2|E_0|}{h_0^2} \left[(\chi_1 - \chi_2)^2 \left(\left(\left(\eta - \frac{1}{2} \right) (\lambda_1 + \lambda_2) - \frac{1}{2}\sqrt{1 - 4\eta} (\lambda_1 - \lambda_2) \right) - \eta \right) \right. \\
& + (\chi_1 + \chi_2)^2 \left(\eta + \left(\left(\eta - \frac{1}{2} \right) (\lambda_1 + \lambda_2) - \frac{1}{2}\sqrt{1 - 4\eta} (\lambda_1 - \lambda_2) \right) \right) \\
& + (\chi_1 + \chi_2) (\chi_1 - \chi_2) \left. \left((2\eta - 1) (\lambda_1 - \lambda_2) - \sqrt{1 - 4\eta} (\lambda_1 + \lambda_2) \right) \right] \\
& + \frac{|E_0|}{h_0^2} \left(-11\eta + 17 + h_0^4|E_0|^2 (-16\eta^2 + 47\eta - 112) + 12\sqrt{2}h_0^3|E_0|^{3/2}(5 - 2\eta) \right) \\
& + 2h_0^2|E_0| (5\eta^2 + \eta + 2) + 6\sqrt{2}h_0\sqrt{|E_0|}(2\eta - 5) \\
& + \frac{\delta}{h_0} \frac{|E_0|}{2h_0^2} \left[(\chi_1 + \chi_2) \left(-16\sqrt{2}h_0^3|E_0|^{3/2} (\eta^2 - 8\eta + 6) + h_0^2|E_0| (32\eta^2 - 159\eta + 124) \right. \right. \\
& + 8\sqrt{2}\sqrt{|E_0|}h_0 (\eta^2 - 8\eta + 6) - 8\eta^2 + 78\eta - 64 \left. \left. \right) \right. \\
& + \sqrt{1 - 4\eta} (\chi_1 - \chi_2) \left(32\sqrt{2}h_0^3|E_0|^{3/2}(\eta - 3) + h_0^2|E_0|(124 - 59\eta) \right. \\
& \left. \left. - 16\sqrt{2}h_0\sqrt{|E_0|}(\eta - 3) + 18\eta - 64 \right) \right]
\end{aligned} \tag{A121}$$

where E_0 and h_0 have the same meaning as in the nonspinning case, and $\lambda_1 = \lambda_2 = -0.5$.

Appendix B: Fitting waveform and parameters

This section showcases the NR waveforms utilized, along with the outcomes of parameter fitting achieved through PN least squares fitting applied to the NR waveforms, encompassing data from the RIT and SXS catalogs for both nonspinning and spin-aligned setups. Additionally, it includes the eccentricity results derived from methodology quasi-Keplerian parameterization $e_{t0\text{KP}}$. In Table II, we present the details of the NR simulations utilized, including the spin configuration, mass ratio, spins χ_1 and χ_2 in the z direction, the fitting time interval, the PN least squares fitting results for parameters x_0 , l_0 , e_{t0} , and ϕ_0 , the fitting residuals Q , and the eccentricity values $e_{t0\text{KP}}$ determined through the quasi-Keplerian parameterization.

TABLE II: Details of the NR simulations utilized, including the spin configuration, mass ratio, spins χ_1 and χ_2 in the z direction, the fitting time interval, the PN least squares fitting results for parameters x_0 , l_0 , e_{t0} , and ϕ_0 , the fitting residuals Q , and the eccentricity values $e_{t0\text{KP}}$ determined through the quasi-Keplerian parameterization.

Simulations	Type	q	χ_1	χ_2	Fitting interval	x_0	l_0	e_{t0}	ϕ_0	Q	$e_{t0\text{KP}}$
RIT:eBBH:1090	Nonspinning	1	0	0	[-1194,-300]	0.082991	3.481579	0.005624	2.590685	1.12×10^{-8}	0.07821
RIT:eBBH:1091	Nonspinning	1	0	0	[-1176,-300]	0.083244	3.847368	0.005751	2.617879	1.13×10^{-8}	0.07798
RIT:eBBH:1092	Nonspinning	1	0	0	[-1157,-300]	0.083499	4.158421	0.006537	2.645123	1.15×10^{-8}	0.07785
RIT:eBBH:1093	Nonspinning	1	0	0	[-1139,-300]	0.083750	4.387895	0.007789	2.676829	1.20×10^{-8}	0.07776
RIT:eBBH:1094	Nonspinning	1	0	0	[-1171,-300]	0.084006	4.547135	0.009305	2.705703	1.26×10^{-8}	0.07774
RIT:eBBH:1095	Nonspinning	1	0	0	[-1153,-300]	0.084260	4.662105	0.011032	2.736338	1.35×10^{-8}	0.07776
RIT:eBBH:1096	Nonspinning	1	0	0	[-1109,-300]	0.084900	4.835789	0.015653	2.814509	1.85×10^{-8}	0.07811
RIT:eBBH:1097	Nonspinning	1	0	0	[-1066,-300]	0.085562	4.938947	0.020546	2.886214	2.37×10^{-8}	0.07882
RIT:eBBH:1098	Nonspinning	1	0	0	[-904,-300]	0.088251	5.154737	0.040786	3.236675	3.05×10^{-8}	0.08499
RIT:eBBH:1099	Nonspinning	1	0	0	[-976,-300]	0.089646	5.221053	0.050058	3.436083	2.46×10^{-8}	0.08979
RIT:eBBH:1100	Nonspinning	1	0	0	[-803,-300]	0.091115	5.265263	0.059644	3.619988	4.93×10^{-8}	0.09551
RIT:eBBH:1101	Nonspinning	1	0	0	[-785,-300]	0.092666	5.302105	0.069016	-2.490113	9.10×10^{-8}	0.10197

(Table continued)

TABLE II (Continued)

Simulations	Type	q	χ_1	χ_2	Fitting interval	x_0	l_0	e_{t0}	ϕ_0	Q	e_{t0KP}
RIT:eBBH:1102	Nonspinning	1	0	0	[-721,-300]	0.094231	5.334737	0.078479	-2.301955	1.61×10^{-7}	0.10903
RIT:eBBH:1103	Nonspinning	1	0	0	[-666,-300]	0.095789	5.384211	0.088226	-2.075571	1.44×10^{-7}	0.11658
RIT:eBBH:1104	Nonspinning	1	0	0	[-602,-300]	0.097444	5.431579	0.096159	-1.849961	3.85×10^{-8}	0.12450
RIT:eBBH:1105	Nonspinning	1	0	0	[-545,-300]	0.099288	5.463158	0.104953	-1.665337	4.08×10^{-8}	0.13273
RIT:eBBH:1106	Nonspinning	1	0	0	[-515,-200]	0.101167	5.484211	0.112440	-1.473961	7.47×10^{-8}	0.14120
RIT:eBBH:1107	Nonspinning	1	0	0	[-468,-200]	0.103230	5.508421	0.119887	-1.292614	8.39×10^{-8}	0.14986
RIT:eBBH:1108	Nonspinning	1	0	0	[-419,-200]	0.105457	5.531579	0.127149	-1.103378	7.13×10^{-8}	0.15868
RIT:eBBH:1109	Nonspinning	1	0	0	[-393,-200]	0.106579	5.537895	0.130435	-0.999022	7.09×10^{-8}	0.16313
RIT:eBBH:1133	Nonspinning	1/4	0	0	[-1844,-800]	0.082499	3.649474	0.003881	2.656878	7.75×10^{-9}	0.08120
RIT:eBBH:1134	Nonspinning	1/4	0	0	[-1816,-800]	0.082742	4.152632	0.004500	2.684012	7.82×10^{-9}	0.08091
RIT:eBBH:1135	Nonspinning	1/4	0	0	[-1788,-800]	0.083013	4.469474	0.005784	2.691516	7.41×10^{-9}	0.08070
RIT:eBBH:1136	Nonspinning	1/4	0	0	[-1760,-800]	0.083233	4.669474	0.007497	2.736034	7.65×10^{-9}	0.08053
RIT:eBBH:1137	Nonspinning	1/4	0	0	[-1733,-800]	0.083483	4.785263	0.009318	2.759675	7.80×10^{-9}	0.08043
RIT:eBBH:1138	Nonspinning	1/4	0	0	[-1706,-800]	0.083767	4.853684	0.011230	2.761049	8.48×10^{-9}	0.08038
RIT:eBBH:1139	Nonspinning	1/4	0	0	[-1640,-700]	0.084392	4.978947	0.016471	2.830922	1.19×10^{-8}	0.08052
RIT:eBBH:1140	Nonspinning	1/4	0	0	[-1576,-700]	0.085026	5.048421	0.021390	2.899352	1.48×10^{-8}	0.08101
RIT:eBBH:1141	Nonspinning	1/4	0	0	[-1447,-600]	0.086355	5.127368	0.031613	3.018197	2.67×10^{-8}	0.08300
RIT:eBBH:1142	Nonspinning	1/4	0	0	[-1427,-600]	0.087708	5.180000	0.041883	3.150058	5.37×10^{-8}	0.08630
RIT:eBBH:1143	Nonspinning	1/4	0	0	[-1366,-500]	0.089116	5.220000	0.051877	3.282279	9.74×10^{-8}	0.09071
RIT:eBBH:1144	Nonspinning	1/4	0	0	[-1308,-500]	0.089815	5.238421	0.057072	3.360127	1.27×10^{-7}	0.09328
RIT:eBBH:1145	Nonspinning	1/4	0	0	[-1250,-400]	0.090576	5.252105	0.061713	3.420018	1.75×10^{-7}	0.09607
RIT:eBBH:1146	Nonspinning	1/4	0	0	[-1194,-400]	0.091315	5.265789	0.066837	-2.786966	2.39×10^{-7}	0.09905
RIT:eBBH:1147	Nonspinning	1/4	0	0	[-1145,-300]	0.092119	5.276316	0.071281	-2.731379	3.30×10^{-7}	0.10222
RIT:eBBH:1148	Nonspinning	1/4	0	0	[-1098,-300]	0.092899	5.285681	0.076129	-2.664751	4.69×10^{-7}	0.10554
RIT:eBBH:1149	Nonspinning	1/4	0	0	[-1051,-300]	0.093649	5.299474	0.081438	-2.570056	6.15×10^{-7}	0.10900
RIT:eBBH:1150	Nonspinning	1/4	0	0	[-1001,-300]	0.094385	5.326007	0.087130	-2.450216	6.05×10^{-7}	0.11261
RIT:eBBH:1151	Nonspinning	1/4	0	0	[-948,-300]	0.095165	5.362632	0.091453	-2.321655	2.92×10^{-7}	0.11632
RIT:eBBH:1152	Nonspinning	1/4	0	0	[-897,-300]	0.095977	5.383684	0.095080	-2.202471	2.39×10^{-7}	0.12014
RIT:eBBH:1153	Nonspinning	1/4	0	0	[-863,-300]	0.096886	5.391053	0.099510	-2.138225	3.41×10^{-7}	0.12405
RIT:eBBH:1154	Nonspinning	1/4	0	0	[-823,-300]	0.097786	5.401579	0.103992	-2.055945	4.80×10^{-7}	0.12804
RIT:eBBH:1155	Nonspinning	1/4	0	0	[-786,-300]	0.098720	5.407895	0.108161	-1.980047	6.85×10^{-7}	0.13211
RIT:eBBH:1156	Nonspinning	1/4	0	0	[-747,-300]	0.099635	5.414211	0.112781	-1.890690	9.69×10^{-7}	0.13624
RIT:eBBH:1157	Nonspinning	1/4	0	0	[-713,-300]	0.100522	5.427368	0.117976	-1.780219	1.24×10^{-6}	0.14044
RIT:eBBH:1158	Nonspinning	1/4	0	0	[-664,-300]	0.101405	5.459532	0.123142	-1.640302	8.99×10^{-7}	0.14468
RIT:eBBH:1159	Nonspinning	1/4	0	0	[-619,-300]	0.102351	5.496842	0.125690	-1.485783	1.34×10^{-7}	0.14896
RIT:eBBH:1160	Nonspinning	1/4	0	0	[-582,-300]	0.103418	5.506842	0.129047	-1.381539	1.28×10^{-7}	0.15331
RIT:eBBH:1161	Nonspinning	1/4	0	0	[-551,-200]	0.104704	5.472105	0.135665	-1.372285	2.44×10^{-6}	0.15769
RIT:eBBH:1162	Nonspinning	1/4	0	0	[-523,-200]	0.105795	5.505263	0.138477	-1.233183	1.07×10^{-6}	0.16209
RIT:eBBH:1163	Nonspinning	1/4	0	0	[-495,-200]	0.107011	5.524211	0.139619	-1.106726	2.00×10^{-7}	0.16653
RIT:eBBH:1164	Nonspinning	1/4	0	0	[-475,-200]	0.108341	5.528421	0.142046	-1.004547	1.82×10^{-7}	0.17100
RIT:eBBH:1165	Nonspinning	1/4	0	0	[-438,-200]	0.109782	5.533158	0.145150	-0.900833	2.09×10^{-7}	0.17549
RIT:eBBH:1200	Nonspinning	1/2	0	0	[-1338,-600]	0.082828	3.492105	0.005325	2.620816	6.44×10^{-9}	0.07926
RIT:eBBH:1201	Nonspinning	1/2	0	0	[-1318,-600]	0.083049	3.894211	0.005613	2.662174	6.83×10^{-9}	0.07903
RIT:eBBH:1202	Nonspinning	1/2	0	0	[-1297,-600]	0.083307	4.224737	0.006504	2.685870	6.80×10^{-9}	0.07886
RIT:eBBH:1203	Nonspinning	1/2	0	0	[-1277,-500]	0.083584	4.428947	0.007645	2.702922	1.00×10^{-8}	0.07875
RIT:eBBH:1204	Nonspinning	1/2	0	0	[-1257,-500]	0.083840	4.588947	0.009305	2.727978	1.06×10^{-8}	0.07870
RIT:eBBH:1205	Nonspinning	1/2	0	0	[-1237,-500]	0.084098	4.701579	0.011162	2.753254	1.15×10^{-8}	0.07871
RIT:eBBH:1206	Nonspinning	1/2	0	0	[-1238,-500]	0.084736	4.875263	0.016016	2.826787	1.36×10^{-8}	0.07899
RIT:eBBH:1207	Nonspinning	1/2	0	0	[-1189,-500]	0.085381	4.982632	0.021096	2.904696	1.39×10^{-8}	0.07962
RIT:eBBH:1208	Nonspinning	1/2	0	0	[-1096,-400]	0.086747	5.081579	0.030955	3.035802	3.46×10^{-8}	0.08193
RIT:eBBH:1209	Nonspinning	1/2	0	0	[-1008,-400]	0.088090	5.172105	0.041114	3.217989	2.45×10^{-8}	0.08550
RIT:eBBH:1210	Nonspinning	1/2	0	0	[-1024,-400]	0.089480	5.230000	0.050503	3.400687	2.46×10^{-8}	0.09018
RIT:eBBH:1211	Nonspinning	1/2	0	0	[-940,-400]	0.090958	5.271053	0.060235	3.567925	4.81×10^{-8}	0.09577
RIT:eBBH:1212	Nonspinning	1/2	0	0	[-861,-400]	0.092456	5.306842	0.069921	-2.533825	9.03×10^{-8}	0.10213
RIT:eBBH:1213	Nonspinning	1/2	0	0	[-811,-300]	0.094081	5.337368	0.078902	-2.366889	1.57×10^{-7}	0.10909
RIT:eBBH:1214	Nonspinning	1/2	0	0	[-743,-300]	0.095700	5.364737	0.088232	-2.183018	2.83×10^{-7}	0.11656
RIT:eBBH:1215	Nonspinning	1/2	0	0	[-673,-300]	0.097303	5.411053	0.098138	-1.955428	2.58×10^{-7}	0.12442

(Table continued)

TABLE II (Continued)

Simulations	Type	q	χ_1	χ_2	Fitting interval	x_0	l_0	e_{t0}	ϕ_0	Q	e_{t0KP}
RIT:eBBH:1216	Nonspinning	1/2	0	0	[-604,-300]	0.099024	5.460526	0.105617	-1.720755	5.21×10^{-8}	0.13259
RIT:eBBH:1217	Nonspinning	1/2	0	0	[-546,-200]	0.101028	5.459474	0.115241	-1.581007	6.42×10^{-7}	0.14101
RIT:eBBH:1218	Nonspinning	1/2	0	0	[-495,-200]	0.102984	5.505789	0.121395	-1.349127	9.04×10^{-8}	0.14963
RIT:eBBH:1219	Nonspinning	1/2	0	0	[-445,-200]	0.105203	5.526842	0.128510	-1.163278	9.81×10^{-8}	0.15841
RIT:eBBH:1241	Nonspinning	3/4	0	0	[-1221,-500]	0.082896	3.491053	0.005832	2.619953	4.84×10^{-9}	0.07841
RIT:eBBH:1242	Nonspinning	3/4	0	0	[-1202,-500]	0.083140	3.860526	0.005992	2.651699	5.51×10^{-9}	0.07820
RIT:eBBH:1243	Nonspinning	3/4	0	0	[-1183,-500]	0.083396	4.175263	0.006806	2.678351	5.66×10^{-9}	0.07805
RIT:eBBH:1244	Nonspinning	3/4	0	0	[-1164,-500]	0.083646	4.408947	0.008117	2.709243	6.25×10^{-9}	0.07797
RIT:eBBH:1245	Nonspinning	3/4	0	0	[-1146,-500]	0.083906	4.573158	0.009682	2.736100	6.08×10^{-9}	0.07794
RIT:eBBH:1246	Nonspinning	3/4	0	0	[-1127,-500]	0.084161	4.693158	0.011389	2.767391	6.17×10^{-9}	0.07797
RIT:eBBH:1247	Nonspinning	3/4	0	0	[-1132,-500]	0.084804	4.877368	0.015982	2.845872	6.04×10^{-9}	0.07830
RIT:eBBH:1248	Nonspinning	3/4	0	0	[-1088,-500]	0.085459	4.979474	0.020735	2.923306	6.27×10^{-9}	0.07899
RIT:eBBH:1249	Nonspinning	3/4	0	0	[-1004,-400]	0.086814	5.094211	0.030822	3.076327	9.91×10^{-9}	0.08141
RIT:eBBH:1250	Nonspinning	3/4	0	0	[-973,-400]	0.088168	5.170000	0.040442	3.257745	1.44×10^{-8}	0.08510
RIT:eBBH:1251	Nonspinning	3/4	0	0	[-944,-400]	0.089604	5.223684	0.050270	3.427651	2.62×10^{-8}	0.08988
RIT:eBBH:1252	Nonspinning	3/4	0	0	[-868,-400]	0.091069	5.267895	0.059978	3.610003	4.87×10^{-8}	0.09557
RIT:eBBH:1253	Nonspinning	3/4	0	0	[-809,-400]	0.092544	5.313158	0.069904	-2.472680	6.54×10^{-8}	0.10201
RIT:eBBH:1254	Nonspinning	3/4	0	0	[-744,-300]	0.094190	5.336316	0.078536	-2.311507	1.59×10^{-7}	0.10906
RIT:eBBH:1255	Nonspinning	3/4	0	0	[-678,-300]	0.095752	5.379474	0.088385	-2.093602	1.85×10^{-7}	0.11658
RIT:eBBH:1256	Nonspinning	3/4	0	0	[-613,-300]	0.097391	5.432105	0.096533	-1.860349	3.83×10^{-8}	0.12449
RIT:eBBH:1257	Nonspinning	3/4	0	0	[-564,-200]	0.099297	5.428947	0.105767	-1.720883	5.43×10^{-7}	0.13271
RIT:eBBH:1258	Nonspinning	3/4	0	0	[-513,-200]	0.101127	5.481579	0.113113	-1.490849	1.23×10^{-7}	0.14117
RIT:eBBH:1259	Nonspinning	3/4	0	0	[-465,-200]	0.103134	5.508947	0.120116	-1.291997	9.38×10^{-8}	0.14983
RIT:eBBH:1260	Nonspinning	3/4	0	0	[-416,-200]	0.105414	5.531579	0.127444	-1.114624	8.84×10^{-8}	0.15863
RIT:eBBH:1282	Nonspinning	1	0	0	[-11536,-1000]	0.048243	4.290850	0.197120	-2.014567	1.17×10^{-7}	0.19553
RIT:eBBH:1283	Nonspinning	1	0	0	[-5696,-1000]	0.053019	4.353711	0.281010	-2.315150	2.34×10^{-7}	0.27984
RIT:eBBH:1284	Nonspinning	1	0	0	[-3602,-1000]	0.056134	4.384316	0.327042	-2.443524	5.19×10^{-7}	0.32785
RIT:eBBH:1285	Nonspinning	1	0	0	[-2690,-500]	0.058312	4.420732	0.359652	-2.493538	9.86×10^{-7}	0.35872
RIT:eBBH:1287	Nonspinning	1	0	0	[-1829,-500]	0.060909	4.419580	0.385463	-2.536189	1.87×10^{-6}	0.38867
RIT:eBBH:1286	Nonspinning	1	0	0	[-2102,-500]	0.061645	4.420937	0.389594	-2.487635	2.00×10^{-6}	0.39602
RIT:eBBH:1289	Nonspinning	1	0	0	[-1913,-400]	0.062348	4.426132	0.396798	-2.484868	2.52×10^{-6}	0.40330
RIT:eBBH:1288	Nonspinning	1	0	0	[-1765,-400]	0.063176	4.414717	0.401683	-2.513374	3.36×10^{-6}	0.41053
RIT:eBBH:1291	Nonspinning	1	0	0	[-1595,-400]	0.063921	4.419815	0.407769	-2.491983	3.72×10^{-6}	0.41770
RIT:eBBH:1290	Nonspinning	1	0	0	[-1452,-400]	0.064839	4.409618	0.410775	-2.467450	4.15×10^{-6}	0.42481
RIT:eBBH:1293	Nonspinning	1	0	0	[-1330,-400]	0.065787	4.399422	0.415695	-2.494619	5.66×10^{-6}	0.43187
RIT:eBBH:1292	Nonspinning	1	0	0	[-1183,-400]	0.066686	4.399422	0.419951	-2.475669	6.06×10^{-6}	0.43887
RIT:eBBH:1295	Nonspinning	1	0	0	[-1065,-300]	0.067709	4.384127	0.427391	-2.513742	8.73×10^{-6}	0.44581
RIT:eBBH:1294	Nonspinning	1	0	0	[-971,-300]	0.068842	4.373021	0.425059	-2.365113	7.55×10^{-6}	0.45269
RIT:eBBH:1297	Nonspinning	1	0	0	[-859,-200]	0.070006	4.357820	0.431041	-2.342054	1.13×10^{-5}	0.45951
RIT:eBBH:1296	Nonspinning	1	0	0	[-743,-200]	0.071370	4.336834	0.431908	-2.344454	1.35×10^{-5}	0.46628
RIT:eBBH:1330	Nonspinning	9/10	0	0	[-11724,-1000]	0.048147	4.305433	0.194825	-1.861335	5.40×10^{-8}	0.19408
RIT:eBBH:1331	Nonspinning	9/10	0	0	[-2694,-500]	0.058225	4.415449	0.357173	-2.471125	9.11×10^{-7}	0.35759
RIT:eBBH:1332	Nonspinning	9/10	0	0	[-1354,-300]	0.065569	4.406231	0.416251	-2.443202	5.15×10^{-6}	0.43088
RIT:eBBH:1333	Nonspinning	9/10	0	0	[-879,-200]	0.069805	4.361599	0.433026	-2.397944	1.29×10^{-5}	0.45859
RIT:eBBH:1353	Nonspinning	4/5	0	0	[-11835,-1000]	0.048140	4.305299	0.195131	-1.854330	5.32×10^{-8}	0.19408
RIT:eBBH:1354	Nonspinning	4/5	0	0	[-3218,-500]	0.058213	4.420283	0.357490	-2.466165	9.09×10^{-7}	0.35756
RIT:eBBH:1355	Nonspinning	4/5	0	0	[-1363,-400]	0.065598	4.405299	0.415505	-2.475990	5.45×10^{-6}	0.43085
RIT:eBBH:1356	Nonspinning	4/5	0	0	[-886,-300]	0.069857	4.363058	0.427429	-2.353169	9.27×10^{-6}	0.45855
RIT:eBBH:1376	Nonspinning	7/10	0	0	[-12064,-1000]	0.048131	4.310106	0.194554	-1.830161	5.28×10^{-8}	0.19407
RIT:eBBH:1377	Nonspinning	7/10	0	0	[-3270,-500]	0.058223	4.420454	0.357109	-2.458103	8.97×10^{-7}	0.35750
RIT:eBBH:1378	Nonspinning	7/10	0	0	[-1381,-400]	0.065585	4.407776	0.415781	-2.466174	5.39×10^{-6}	0.43077
RIT:eBBH:1379	Nonspinning	7/10	0	0	[-899,-300]	0.069874	4.363024	0.427431	-2.343689	9.23×10^{-6}	0.45847
RIT:eBBH:1399	Nonspinning	3/5	0	0	[-12481,-1000]	0.048114	4.318550	0.193576	-1.781341	5.14×10^{-8}	0.19406
RIT:eBBH:1400	Nonspinning	3/5	0	0	[-3369,-500]	0.058197	4.426576	0.357626	-2.438717	9.05×10^{-7}	0.35740
RIT:eBBH:1401	Nonspinning	3/5	0	0	[-1410,-400]	0.065587	4.410445	0.415863	-2.455433	5.31×10^{-6}	0.43065
RIT:eBBH:1402	Nonspinning	3/5	0	0	[-920,-300]	0.069849	4.368388	0.428583	-2.337774	9.30×10^{-6}	0.45834
RIT:eBBH:1422	Nonspinning	1/2	0	0	[-12846,-1000]	0.048242	4.298953	0.198058	-1.882699	6.29×10^{-8}	0.19536

(Table continued)

TABLE II (Continued)

Simulations	Type	q	χ_1	χ_2	Fitting interval	x_0	l_0	e_{t0}	ϕ_0	Q	e_{t0KP}
RIT:eBBH:1423	Nonspinning	1/2	0	0	[-3487,-500]	0.058316	4.419950	0.358598	-2.447685	9.50×10^{-7}	0.35826
RIT:eBBH:1424	Nonspinning	1/2	0	0	[-1439,-400]	0.065719	4.411384	0.416867	-2.443388	5.49×10^{-6}	0.43134
RIT:eBBH:1425	Nonspinning	1/2	0	0	[-938,-300]	0.070032	4.368712	0.428990	-2.304345	9.90×10^{-6}	0.45898
RIT:eBBH:1445	Nonspinning	2/5	0	0	[-14012,-1000]	0.048164	4.307285	0.197959	-1.844830	5.75×10^{-8}	0.19403
RIT:eBBH:1446	Nonspinning	2/5	0	0	[-3772,-500]	0.058219	4.424085	0.358421	-2.435551	9.45×10^{-7}	0.35700
RIT:eBBH:1447	Nonspinning	2/5	0	0	[-1537,-400]	0.065575	4.417081	0.417076	-2.415085	5.33×10^{-6}	0.43017
RIT:eBBH:1448	Nonspinning	2/5	0	0	[-1002,-300]	0.069843	4.377519	0.431653	-2.298384	1.14×10^{-5}	0.45785
RIT:eBBH:1468	Nonspinning	1/3	0	0	[-14885,-1000]	0.048270	4.293214	0.202685	-1.947855	9.08×10^{-8}	0.19516
RIT:eBBH:1469	Nonspinning	1/3	0	0	[-4021,-500]	0.058240	4.434938	0.361682	-2.457581	1.08×10^{-6}	0.35768
RIT:eBBH:1470	Nonspinning	1/3	0	0	[-1627,-400]	0.065581	4.424968	0.424166	-2.521533	7.66×10^{-6}	0.43069
RIT:eBBH:1471	Nonspinning	1/3	0	0	[-1038,-300]	0.070000	4.379848	0.435683	-2.335837	1.47×10^{-5}	0.45831
RIT:eBBH:1491	Nonspinning	1/4	0	0	[-17606,-1000]	0.048185	4.327294	0.197261	-1.714333	4.89×10^{-8}	0.19398
RIT:eBBH:1492	Nonspinning	1/4	0	0	[-4650,-500]	0.058175	4.436953	0.361381	-2.425922	1.03×10^{-6}	0.35642
RIT:eBBH:1493	Nonspinning	1/4	0	0	[-1874,-400]	0.065422	4.433595	0.424074	-2.422223	7.31×10^{-6}	0.42948
RIT:eBBH:1494	Nonspinning	1/4	0	0	[-1141,-300]	0.069895	4.388408	0.443018	-2.502784	1.99×10^{-5}	0.45714
RIT:eBBH:1740	Spin-ligned	1	-0.5	-0.5	[-9966,-1000]	0.048861	4.243120	0.201827	-2.789773	1.95×10^{-7}	0.20702
RIT:eBBH:1741	Spin-ligned	1	-0.5	-0.5	[-2159,-500]	0.061191	4.356750	0.363587	-2.906665	1.64×10^{-6}	0.37058
RIT:eBBH:1763	Spin-ligned	1	-0.8	-0.8	[-8926,-1000]	0.049339	4.225607	0.205185	-3.202682	3.56×10^{-7}	0.22918
RIT:eBBH:1764	Spin-ligned	1	-0.8	-0.8	[-1493,-400]	0.064034	4.309648	0.365244	-2.991234	2.49×10^{-6}	0.38297
RIT:eBBH:1786	Spin-ligned	1	0.5	0.5	[-2320,-400]	0.061876	4.474999	0.411076	-1.991020	5.16×10^{-6}	0.42191
RIT:eBBH:1787	Spin-ligned	1	0.5	0.5	[-1739,-400]	0.064529	4.466832	0.431725	-2.085661	1.04×10^{-5}	0.44865
RIT:eBBH:1788	Spin-ligned	1	0.5	0.5	[-1091,-400]	0.069618	4.427534	0.446566	-2.095252	1.89×10^{-5}	0.48712
RIT:eBBH:1807	Spin-ligned	1	0.8	0.8	[-2854,-400]	0.060530	4.499562	0.404775	-1.604014	6.69×10^{-6}	0.41899
RIT:eBBH:1808	Spin-ligned	1	0.8	0.8	[-2221,-400]	0.062669	4.507297	0.428760	-1.757701	9.56×10^{-6}	0.44437
RIT:eBBH:1809	Spin-ligned	1	0.8	0.8	[-1487,-400]	0.066603	4.487266	0.455576	-1.942250	2.26×10^{-5}	0.48103
RIT:eBBH:1810	Spin-ligned	1	0.8	0.8	[-967,-300]	0.072278	4.415135	0.455850	-1.814238	4.39×10^{-5}	0.51587
RIT:eBBH:1811	Spin-ligned	1	0.8	0.8	[-710,-200]	0.077459	4.305993	0.454949	-1.786925	9.04×10^{-5}	0.53805
RIT:eBBH:1828	Spin-ligned	1	0	0.8	[-2146,-400]	0.062397	4.467975	0.412924	-2.125679	4.96×10^{-6}	0.42570
RIT:eBBH:1829	Spin-ligned	1	0	0.8	[-1592,-400]	0.065208	4.458413	0.434177	-2.202726	9.50×10^{-6}	0.45243
RIT:eBBH:1830	Spin-ligned	1	0	0.8	[-961,-300]	0.071002	4.391649	0.444828	-2.092890	2.10×10^{-5}	0.49102
RIT:eBBH:1862	Spin-ligned	1/3	0	-0.8	[-2081,-400]	0.062686	4.335796	0.371205	-3.068030	3.60×10^{-6}	0.37980
RIT:eBBH:1883	Spin-ligned	1/2	0	-0.8	[-2130,-400]	0.061833	4.344211	0.366412	-2.335113	2.29×10^{-6}	0.35251
RIT:eBBH:1899	Spin-ligned	1	0	-0.8	[-10460,-1000]	0.048638	4.281648	0.197918	-2.489198	1.05×10^{-7}	0.21209
RIT:eBBH:1900	Spin-ligned	1	0	-0.8	[-2356,-400]	0.060398	4.372612	0.364363	-2.894547	1.55×10^{-6}	0.37087
RIT:eBBH:1901	Spin-ligned	1	0	-0.8	[-813,-200]	0.071933	4.268929	0.408480	-2.712869	4.74×10^{-6}	0.44535
SXS:BBH:1355	Nonspinning	1	0	0	[-3071,-300]	0.068757	1.994624	0.066123	0.951318	6.80×10^{-8}	0.06123
SXS:BBH:1356	Nonspinning	1	0	0	[-6583,-300]	0.056819	5.976205	0.119648	-0.254013	5.36×10^{-8}	0.14171
SXS:BBH:1357	Nonspinning	1	0	0	[-3420,-300]	0.066068	6.556144	0.128740	1.853997	1.07×10^{-7}	0.12760
SXS:BBH:1358	Nonspinning	1	0	0	[-3181,-300]	0.067207	6.635232	0.127084	2.096370	9.19×10^{-8}	0.12789
SXS:BBH:1359	Nonspinning	1	0	0	[-3053,-300]	0.067894	0.387847	0.125970	2.205003	9.35×10^{-8}	0.15151
SXS:BBH:1360	Nonspinning	1	0	0	[-2896,-300]	0.067348	0.360219	0.178906	2.633178	1.80×10^{-7}	0.19791
SXS:BBH:1361	Nonspinning	1	0	0	[-2849,-300]	0.067572	0.358490	0.180128	2.660157	2.41×10^{-7}	0.17654
SXS:BBH:1362	Nonspinning	1	0	0	[-2673,-300]	0.066603	0.393420	0.238166	3.106062	4.35×10^{-7}	0.24186
SXS:BBH:1363	Nonspinning	1	0	0	[-2635,-300]	0.066767	0.396938	0.238877	3.163563	9.74×10^{-7}	0.24513
SXS:BBH:1364	Nonspinning	1/2	0	0	[-3727,-300]	0.067400	0.669219	0.056787	1.332571	5.92×10^{-8}	0.05986
SXS:BBH:1365	Nonspinning	1/2	0	0	[-3709,-300]	0.067254	0.418394	0.075791	1.519396	9.08×10^{-8}	0.06439
SXS:BBH:1366	Nonspinning	1/2	0	0	[-3602,-300]	0.066900	0.238871	0.124168	1.871625	1.16×10^{-7}	0.13724
SXS:BBH:1367	Nonspinning	1/2	0	0	[-3481,-300]	0.067475	0.264768	0.122686	1.948643	1.16×10^{-7}	0.11288
SXS:BBH:1368	Nonspinning	1/2	0	0	[-3374,-300]	0.067988	0.298730	0.121591	2.051288	1.43×10^{-7}	0.13330
SXS:BBH:1369	Nonspinning	1/2	0	0	[-3150,-300]	0.065673	0.231351	0.237012	2.555949	5.47×10^{-7}	0.24024
SXS:BBH:1370	Nonspinning	1/2	0	0	[-2903,-300]	0.067051	0.311412	0.230810	2.925016	6.08×10^{-7}	0.24001
SXS:BBH:1371	Nonspinning	1/3	0	0	[-4236,-300]	0.067573	0.295354	0.070978	1.375396	1.02×10^{-7}	0.10062
SXS:BBH:1372	Nonspinning	1/3	0	0	[-4094,-300]	0.067292	0.126380	0.119649	1.731706	2.12×10^{-7}	0.11868
SXS:BBH:1373	Nonspinning	1/3	0	0	[-3979,-300]	0.067743	0.155603	0.118981	1.809612	1.86×10^{-7}	0.13512
SXS:BBH:1374	Nonspinning	1/3	0	0	[-3547,-300]	0.066333	0.138994	0.230359	2.324821	7.63×10^{-7}	0.24115